Hydrodynamic and Water Quality Modeling of Lake and Estuary Systems Considering Inflow and Outflow Effects

by

Bushra Tasnim

A dissertation submitted to the Graduate Faculty of
Auburn University
in partial fulfillment of the
requirements for the Degree of
Doctor of Philosophy

Auburn, Alabama
December 09, 2023

Keywords: computational hydraulics, EFDC, eutrophication, estuary restoration, sea level rise

Approved by

Joel S. Hayworth, Co-Chair, Elton Z. and L.G.F. Associate Professor of Civil and Environmental Engineering
Xing Fang, Co-Chair, Arthur H. Feagin Chair Professor of Civil and Environmental Engineering
Mark O. Barnett, Professor of Civil and Environmental Engineering
Anna Linhoss, Associate Professor of Biosystems Engineering

Abstract

Algal bloom, fish kill, hypoxia, and toxicity are some of the water quality issues faced by many waterbodies, from lakes to estuaries. Internal or external nutrients cause excess growth of algae and then lead to low or no dissolved oxygen (DO) in the waterbody, which impairs the life of living organisms, fish, etc. This has a direct influence on public health, the biological integrity of natural resources, and the economy. This study focuses on understanding the nutrient dynamics and using appropriate water quality model to mimic the nutrient conditions on a range of waterbodies, small lakes to estuaries. An existing lake water quality model MINLAKE2012 was modified to include nitrogen, phosphorus and DO sub-models along with sediment flux calculation to simulate the water quality parameters for long term. Six lakes in Minnesota were simulated using this model and the average standard error for DO simulation of these lakes decreased by 24.2% from the original MINLAKE2012 model, which indicates better model performance. This model is suggested as a reliable tool to managers. A comparative study of 1-D MINLAKE and 3-D EFDC model has been conducted for three lakes in Minnesota. It was found that the EFDC model is suitable where the spatial variance is significant within the waterbody. However, one drawback of EFDC is the absence of a snow model which is important for cold regions. The 3-D EFDC model, being reliable for capturing spatial variance and being more detailed, was used to simulate water quality in Cotton Bayou-Terry Cove system in Mobile, Alabama, which has multiple inflows and very complex bathymetry. This estuary has been suffering from very poor water quality, and fish kill issues which have caused economic and cultural loss. Following the nested model approach of EFDC, the model was calibrated using the continuous observed data for water level, water temperature and DO collected at three locations

in Cotton Bayou-Terry Cove system. The standard error for DO simulation ranged from 1.09 mg/L to 1.50 mg/L at the three locations. Different restoration techniques were tested to select the most efficient one by using different boundary conditions in EFDC which includes aerator and dredging. A total of sixteen aerator sets were required to keep the DO above the target DO, 3 mg/L. When both aerator and dredging were used, a dredged channel in Cotton Bayou and nine aerator sets were able to keep the DO above the target DO at all time. Finally, the best restoration techniques were tested against future climate and sea level rise scenarios to predict how the estuary would behave with the restoration techniques implementation in the future. This study gives an overall idea of water quality modeling which will be useful for lake and estuary restoration and help the managers to make informed decisions.

Acknowledgements

I would like to express my heartfelt gratitude to Dr. Hayworth for providing me with the opportunity to pursue my doctoral studies and providing his valuable insights throughout my dissertation journey. The one person who has taught me everything since I first came to Auburn, helped me in academic research and always inspired me to dream big and believe in my potential is Dr. Fang- I am forever indebted to him. I am very lucky to have two amazing advisors who are not only great researchers, but also great human beings. I would like to express my gratitude to Dr. Barnett, Dr. Linhoss for their support as Committee members and to Dr. Panizzi for her support as the University Reader.

Special thanks to Dr. Vanisree Mulabagal and my amazing friends Suranjana, Meredith, Danyang, Sai Deepthi, Susan and Nikit for their support.

I am grateful to the Almighty and my family members, relatives, friends and well-wishers for their continuous support and prayers throughout my life. I would like to thank my grandmother Mrs. Masuda Faiz Chowdhury for planting the dream of becoming a Dr. very early in my career. My mother, Alif Layla, my biggest support and best friend, thanks for always inspiring me and listening to me without any complaints; my father, Md. Hedayet Ullah for supporting me, my brother, Fahim Ahmed, for always being there. I would like to thank my partner in all ups and downs, Dr. Mohammad Ashraful Haq for his constant support throughout this journey.

Table of Contents

List of Figures

List of Tables

List of Abbreviations

mg/L	miligrams/liter
m	meter
km	kilometer
m/s	meter/second
m2/hr	square meters per hour
J/m3	Joule per cubic meter
cm2/sec	square centimeters per second
µg/L	microgram per liter
cfs	cubic feet per second
cms	cubic meter per second
^{o}C/m	degree Celsius per meter
kg/m^3	kilograms per cubic meter
kJ/kg	kilojoules per kilogram
W/m^2	Watt per square meter
ppt	parts per million

Chapter 1 Introduction

1.1 Background

Eutrophication has been a threat to waterbodies since the beginning of the twentieth century in industrialized countries (Le Moal et al., 2018; Moss, 2011); Takolander et al. (2017). A large proportion of the anthropogenic increase in nitrogen and phosphorus flux due to industrialization is delivered to ground or surface waters through direct runoff, human and animal wastes, and atmospheric deposition. Over time, excess nutrients are transported to waterbodies (Liu et al., 2008; Turner, 2003). When a waterbody undergoes any human- or natural-influenced ecosystem changes such as nutrient loading, extreme weather events, or invasive organisms; algal species (cyanobacteria) can form dense overgrowths known as algal blooms. Since these blooms can produce toxins that are harmful to people and animals they are often referred to as harmful algal blooms (HAB). HABs cause undesirable changes in aquatic resources such as reduced water clarity, hypoxia, fish kills, loss of biodiversity, and an increase in nuisance species (Townsend et al., 2003; Wolfe & Patz, 2002). Oxygen is consumed by both living and dead algae which results in low oxygen concentration in lakes and estuaries known as hypoxia (below 2-4 mg/L of dissolved oxygen (DO)). Eutrophication also has a detrimental effect on human health through increased exposure to cyanobacteria toxins (Hudnell, 2010; Hudnell & Dortch, 2008), nitrites, and nitrates (Townsend et al., 2003; Wolfe & Patz, 2002) in drinking water. Since most cities use surface water as the drinking water source, HABs can cause serious problems of off-flavor odor and taste (sometimes described as earthy or musty). In some cases, drinking water no longer remains safe to drink and a complete cleanup is needed. For example, the state of Ohio committed to spending $172 million to clean up Lake Erie as HABs were causing severe drinking water problems (Seewer, 2020). Furthermore, the economic costs

of eutrophication, for restoring the ecosystem services (e.g., housing amenity value, recreation opportunities, freshwater provisioning, and food and fiber production) are high (Dodds et al., 2008; Moomaw & Birch; Pretty et al., 2003). Eutrophication can have serious effects on the social health of a community causing decreases in activity that are dependent on aquatic or seafood harvests or tourism, resulting in disruption of social, and cultural practices. It is estimated that in North America, more than 41% of lakes are eutrophic (Bartram & Chorus, 1999).

Estuaries are also affected by eutrophication (Livingston, 2001;Bricker et al. 2007). Estuaries are among the most productive systems in nature, due in large part to the balance of fresh water and saline water in estuaries (Bales et al., 2006). Phytoplankton growth and variations of nutrients in lakes or estuaries are directly related to input from inflowing rivers and tributaries (Shen and Haas 2004). Harmful algal blooms found in estuarine waters are caused by circulation, river flow, and anthropogenic nutrient loadings leading to eutrophication (Sellner et al.2003). The dynamic forcing in the system results in the spatial and temporal variability of salinity, temperature, and nutrients in estuaries. Several studies have reviewed the effects of excess nutrients on coastal systems that include hypoxia, increased algal biomass, and excessive concentrations of toxic algae (e.g., Howarth et al 2009; Bricker et al., 2007; Shen & Haas, 2004).

Identifying the key parameters affecting water quality is very important in eutrophication studies. To understand the occurrence of eutrophication, it is important to understand the interaction between hydrodynamics and water quality. Hypoxia created at the bottom of a lake or estuary often results from a lack of mixing within the waterbody(Herb & Stefan, 2005; Markfort et al., 2010). This can result from low wind speeds at the water surface, which fail to impart enough energy into the water to mix the whole waterbody. The bathymetry of a waterbody can

also hinder mixing. Variations in weather conditions on short and long timescales can also impact water quality (Fang & Stefan, 1997; Fang et al., 2004).

Management and restoration solutions to control eutrophication require predicting the nutrient concentration, understanding interactions between hydrodynamics and water quality variables, and quantifying algal growth and decay. Since the 1970s, numerical modeling has shown to be an effective tool to quantify nutrient concentrations (Imboden, 1974; Vollenweider & J., 1982). Several promising surface water numerical models have been developed over the past decades (MINLAKE, PCLake, LAKE2K, CE-QUAL-W2, EFDC, and ELCOM-CAEDYM). The key state variables of these models are nutrients, principally phosphorus (P), nitrogen (N), and sometimes silica (Si) since these nutrients link to primary production.

For eutrophic lakes, high phosphorus release from lake sediments is sometimes reported as a mechanism delaying lake recovery after the external loading of phosphorus has been reduced (Marsden, 1989; Philips et al., 2005; Sondergaard et al., 2007). Since internal loading adds uncertainty to lake restoration processes, a reliable lake water quality modeling tool that, a) focuses on the internal nutrient dynamics, b) considers all physical processes (e.g., ice cover, sediment heat transfer), c) is applicable to different types of lakes, and d) is capable of multiple year simulation, are ideal. For lake management and restoration purposes, models which can predict chlorophyll-a, phosphorus, and DO in various types of lakes (shallow to deep, small to large surface area, and oligotrophic to eutrophic) for short-term and long-term simulations is necessary.

Estuaries are very productive waterbodies which often suffer from fish kill, HABs and other water quality issues. Due to its economic and anthropogenic importance, impaired estuaries are most likely to be restored by the management. It has been reported that often the restoration

measures are not adequate to address the water quality issue (Harris et al., 2015, Conley et al., 2009). This happens for not understanding the hydrodynamics and water quality mechanisms. Each estuary acts differently based on its bathymetry, mixing capabilities etc. Therefore, a modeling approach might be very useful that a) considers all physical processes, b) considers the spatial variance of the hydrodynamic and water quality constituents, c) calibrates the model with continuous observed data, d) includes predictive modeling of some promising management options. A detailed modeling approach with all the above-mentioned capabilities is very necessary to make informed decisions for estuary restoration.

1.2 Objectives

The primary objectives of this study are to utilize advanced hydrodynamic and water quality simulation models to understand the interaction between hydrodynamics and water quality, identify the primary stressors of eutrophication in lakes and estuaries, and apply this knowledge to examine potential restoration strategies within an estuary with known water quality degradation (with and without the influence of climate change).

1.3 Models Used

1.3.1 MINLAKE

The Minnesota Lake Water Quality Management Model (MINLAKE) is a one-dimensional (along depth direction), deterministic water quality model with a time step of one day and was developed in 1988 for supporting lake eutrophication studies and was capable of simulating water temperature, chlorophyll a (Chl*a*), phosphorus, nitrogen, biochemical oxygen demand (BOD), dissolved oxygen (DO) for lakes during the open water season (Riley & Stefan, 1988). Ice cover period is defined as the period when the lake does not have ice cover; the rest of

the year is called the open water season. MINLAKE1988 was further developed to include ice-cover period simulation (Gu & Stefan, 1990), simplified regional DO model (X Fang & H. G. Stefan, 1994), modified year-round nutrient model (West & H. G. Stefan, 1998), and hourly water temperature and DO model (Jamily, 2018). MINLAKE nutrient model (MINLAKE98) was applied to three lakes but did not perform well for multiple year simulation (West & Stefan, 1998); hence, the model was not used further. The most recent version of MINLAKE with daily simulation, MINLAKE2012 was capable of simulating water temperature and DO in different types of lakes with good agreement with observations (Batick, 2011) but lacks a nutrient model.

MINLAKE models use the basic one-dimensional advection-diffusion equation to simulate the dynamic variations of state variables in horizontal layers of a lake.

$$A\frac{\partial \mathrm{C}}{\partial \mathrm{t}} + v\frac{\partial(\mathrm{A}*\mathrm{C})}{\partial \mathrm{z}} = \frac{\partial}{\partial \mathrm{z}}\left(K_z A\frac{\partial \mathrm{C}}{\partial \mathrm{z}}\right) \pm sources/sinks \tag{1.1}$$

where C is the concentration of a state variable, v is the vertical settling velocity of the particulate form of some of the state variables (v = 0 for dissolved); z is the vertical coordinate measured positively downward; K_z is the vertical turbulent diffusion coefficient; and $A(z)$ (m^2) is the horizontal area for each layer of water as a function of the depth. For all MINLAKE model variants, water temperature is simulated first by solving the following heat transport equation.

$$\frac{\partial T_w}{\partial t} = \frac{1}{A}\frac{\partial}{\partial z}\left(K_z A\frac{\partial T_w}{\partial z}\right) + \frac{H_w}{\rho C_P} \tag{1.2}$$

where $T_w\,(z, t)$ is the water temperature in (^{o}C), which is a function of depth (z) and time (t); Kz (m^2/day) is the vertical turbulent heat diffusion coefficient which is a function of depth and time; $\boldsymbol{\rho}C_p$ (J/m^3- ^{o}C) represents the heat capacity of water per unit volume; H_w (J/m^3-day) is the heat source and/or sink term per unit volume of water. Determination of the turbulent diffusion coefficient is discussed in detail by Fang (Xing Fang & Heinz G Stefan, 1994). In the regional

daily MINLAKE model, the vertical heat diffusion coefficient K_z for epilimnion and hypolimnion is calculated using the following equation:

$$K_z = 8.17 \times 10^{-4} \times \frac{As^{0.56}}{(N^2)^{0.43}} \quad (1.3)$$

where K_z is the vertical diffusion coefficient in cm^2/sec (1 cm^2/sec = 8.64 m^2/day = 0.36 m^2/hr), A_s is the surface area of the lake (km^2) and N^2 is the Brunt-Vaisala stability frequency of the stratification (sec^{-2}). In the epilimnion, N^2 was set at a minimum value of 0.000075 (Hondzo & Stefan, 1993). Equations (1) and (2) are solved numerically using an implicit finite difference scheme and a Gaussian elimination method with time steps of one day.

1.3.2 Environmental Fluid Dynamics Code (EFDC+)

EFDC+ is an advanced hydrodynamic and water quality simulation model that includes six internal correlative sub-models: wind wave model, hydrodynamic model, sediment transport model, eutrophication model, toxic model, and sediment bed model/sediment diagenesis model (Figure 1-1). The hydrodynamic model is the most fundamental part of the EFDC+ simulation model (Figure 1-1). It works as the energy source to operate the remaining models. Once receiving information from the hydrodynamic model such as water level, water velocity, water temperature, salinity and so on, the water quality (eutrophication) model can simulate water quality parameter distribution. Meanwhile, the concentrations of water quality parameters are also affected by the sediment transport model and sediment bed model.

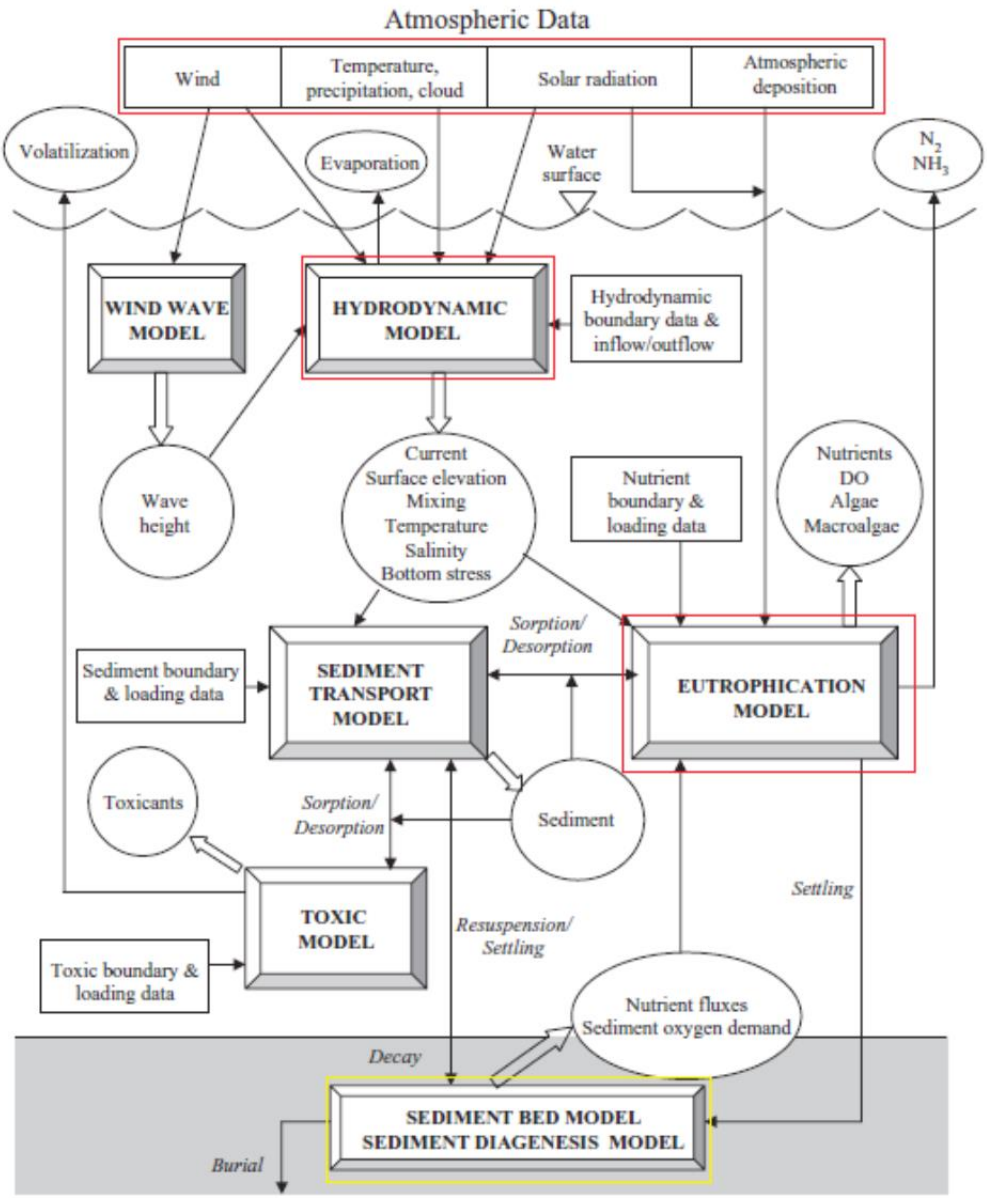

Figure 1-1 Six Interconnected Submodels of EFDC+ (adopted from Li, 2019)

Table 1-1 lists the 22 EFDC state variables and corresponding abbreviation symbols in the water quality (eutrophication) model. The 22 state variables are divided into 6 groups: algae group, organic carbon group, phosphorus group, nitrogen group, silica group, and other water quality variables.

Table 1-1 Water Quality Variables Simulated by EFDC (Li, 2019)

Water Quality Variable Group	Variable Number and Name
Algae	(1) Cyanobacteria (blue-green algae) (B_c)
	(2) Diatom algae (B_d)
	(3) Green algae (B_g)
	(22) Macroalgae (B_m)[b]
Organic carbon	(4) Refractory particulate organic carbon (RPOC)
	(5) labile particulate organic carbon (LPOC)
	(6) dissolved organic carbon (DOC)
Phosphorus	(7) refractory particulate organic phosphorus (RPOP)
	(8) labile particulate organic phosphorus (LPOP)
	(9) dissolved organic phosphorus (DOP)
	(10) total phosphate (PO4t)
Nitrogen	(11) refractory particulate organic nitrogen (RPON)
	(12) labile particulate organic nitrogen (LPON)
	(13) dissolved organic nitrogen (DON)
	(14) ammonia nitrogen (NH4)
	(15) nitrate nitrogen (NO3)
Silica	(16) particulate biogenic silica (SU)
	(17) available silica (SA)
Other	(18) chemical oxygen demand (COD)
	(19) dissolved oxygen (DO)
	(20) total active metal (TAM)[c]
	(21) fecal coliform bacteria (Feb)[d]

Figure 1-2 is a schematic diagram showing these relationships. The algae group is placed at the base because they are primary producers and are the originator and receiver of changes in water quality. The four types of nutrients (carbon, nitrogen, phosphorus, and silica) have direct relationship in their respective group(s). Although one group of nutrient is not much affected by another group of nutrient, all of them directly affect the DO concentration.

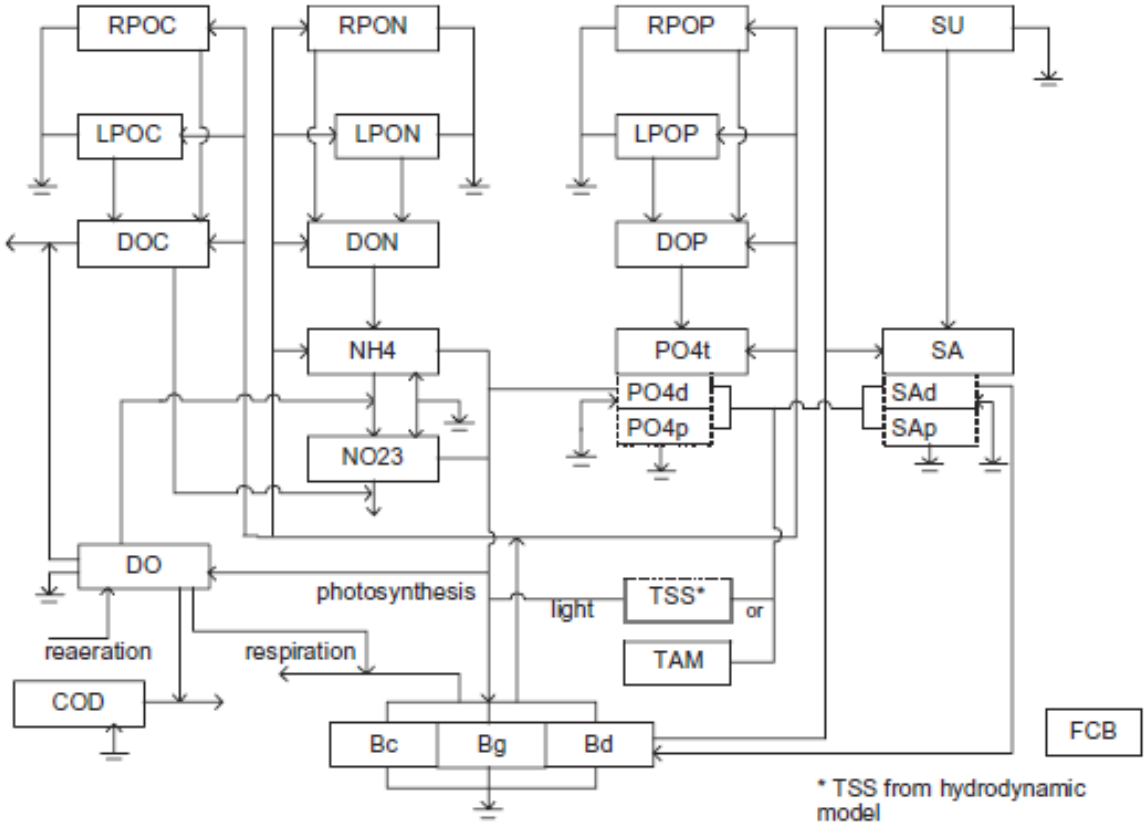

Figure 1-2 Schematic diagram of EFDC hydrodynamic and water quality modeling components (adopted from Li, 2019).

1.3.2.1 Hydrodynamic Model

Hydrodynamics is a study focusing on the motion of water featuring the transportation of sediments, toxins, and nutrients in the water body. The solution of the hydrodynamic model is a complex process which often involves atmospheric forcing, Coriolis force and geostrophic flow, upstream inflows and downstream outflows. Their effect can be expressed as the flow velocity, pressure, density, and temperature functions of space and time under the governing of conservation laws. The precipitation, relative humidity, cloud cover, and atmospheric pressure can affect the water capacity held by the study area by changing the water level. The wind speed and direction form the forces acting on the water column, together with the gravitational force,

the viscous force, and the force from water pressure gradients. For a relatively large study area, Coriolis force can also be significant to circulations in the water body, which is caused by the earth rotation. Under the influence of the Coriolis force, the objects in the water body tend to deflect a few degrees to the right in the Northern Hemisphere to some extent. In addition, the dispersion also plays an important role in the transportation of dissolved substances such as salinity, DO and so on, through the horizontal spreading and mixing of water mass caused by turbulent mixing and molecular diffusion. Besides, the turbulence model developed by Mellor and Yamada is used to represent the vertical mixing process in EFDC. The detail functions linking with the hydrodynamic model under the curvilinear horizontal and sigma vertical coordinate system are listed as the following:

$$\partial_t(m_x m_y Hu) + \partial_x(m_y Huu) + \partial_y(m_x Hvu) + \partial_z(m_x m_y wu) - m_x m_y f_c Hv = -m_y H\partial_x(p + gH + gz_b^*) - m_y(\partial_x h - z\partial_x H)\partial_z p + m_x m_y \partial_z(H^{-1}A_v\partial_z u) + Q_u$$

(1.4)

$$\partial_t(m_x m_y Hv) + \partial_x(m_y Huv) + \partial_y(m_x Hvv) + \partial_z(m_x m_y wv) - m_x m_y f_c Hu = -m_y H\partial_y(p + gH + gz_b^*) - m_x(\partial_y h - z\partial_y H)\partial_z p + m_x m_y \partial_z(H^{-1}A_v\partial_z v) + Q_v$$

(1.5)

$$\partial_z p = -gHb = -gH(\rho - \rho_0)\rho_0^{-1}$$

(1.6)

$$\partial_t(m_x m_y H) + \partial_x(m_y Hu) + \partial_y(m_x Hv) + \partial_z(m_x m_y w) = Q_H$$

(1.7)

$$m_x m_y f_c = m_x m_y f - u\partial_y m_x + v\partial_x m_y$$

(1.8)

where u and v are the horizontal velocities in the curvilinear-orthogonal horizontal coordinates (x, y); w is the vertical velocity in the stretched vertical coordinate z; p is the excess pressure above the reference density hydrostatic pressure divided by the reference density, z_s* is the free surface elevation, z_b* is the bottom or topography elevation, H $(= z_s$*$- z_b$*$)$ is the total water column depth in a grid; A_v is the horizontal eddy or turbulent viscosity; f_c is the Coriolis parameter; Q_u and Q_v represent additional forces or momentum sources and sinks, including horizontal turbulent momentum diffusion, vegetation resistance, and wave Reynolds stress due to high frequency gravity waves; Q_H is the source/sink term used to represent direct rainfall, evaporation, groundwater interaction, water wi8thdrawals, and point and nonpoint source discharges; m_x and m_y are dimensionless scale factors for curvilinear horizontal coordinates. The sigma coordinate z is dimensionless, $z= 0$ at the bottom topography, and $z=1$ at the free surface for all grids, but water depth H is a function of time and location and solved by the EFDC.

The generic transport equation in EFDC for a dissolved or suspended constituent C (Hamrick 1992b) is:

$$\partial_t(m_x m_y HC) + \partial_x(m_y HuC) + \partial_y(m_x HvC) + \partial_z(m_x m_y wC) = m_x m_y \partial_z(H^{-1}\partial_z A_b C + \sigma C) + m_x m_y H R_C + Q_C \quad (1.9)$$

where A_b is the vertical turbulent or eddy diffusivity; σ is the settling velocity, which is zero for a dissolved constituent or tracer modeled in this study; and R_c is the reactive sources and sinks. The horizontal turbulent diffusion and external sources and sinks associated with volumetric withdrawals and discharges are accounted for using Q_C. The transport of dynamically active constituents such as salinity, temperature, and suspended sediment is coupled with the momentum equations through an equation of state and the hydrostatic approximation (Equation

1.6). The second moment turbulence closure model developed by Mellor and Yamada (1982) and modified by Galperin et al. (1988b) and Kantha and Clayson (1994) is used in the EFDC model to relate vertical turbulent viscosity and diffusivity to the turbulent intensity, a turbulent length scale, and a Richardson number.

1.3.2.2 Water Temperature Model

Water temperature is an important parameter in water quality modeling. All other parameters in the hydrodynamic and water quality models are related or dependent on water temperature. In addition, water stratification is affected by the vertical temperature profile because water density changes with temperature. The combining results from surface heat exchange and the water temperature of inflow and outflow determine the temperature of a water body (Equation 1.10).

Surface heat exchange can be regarded as a combination of five processes: net solar shortwave radiation, net atmospheric longwave radiation, longwave back-radiation from the water, conduction, and evaporation (Figure 1-3) (Eq. 1.11). Among the five processes, solar radiation (W/m^2) is the most important in terms of magnitude. It primarily depends on the altitude of the sun and also reduces by cloud cover. It contributes to the surface heat exchange only during daylight hours. Solar radiation at most weather stations is not recorded but estimated/predicted by numerical models. The net atmospheric longwave radiation refers to downward radiation from the atmosphere, which represents the mechanism of how air temperature affects the heat flux penetrating into the water column. In contrast to solar radiation, atmospheric radiation is a significant component for heat balance during non-daylight hours

because the air temperature will never reach absolute zero on the Kelvin scale. Longwave back radiation from the water is the upward radiation emitted by the water surface. This value is connected with the surface water temperature. Conduction is a process where heat spontaneously transfers from a warmer to a cooler body. It occurs when substances having different temperatures come into contact. In the surface heat exchange model, conduction occurs only in the thin layer where air touches the surface water. Evaporation is a process where liquid surface water converts to the vapor state. In this process, latent heat flux is removed from the water body as the energy to break down the hydrogen bonds among the liquid water molecules to convert them to the vapor state. Equation 1.12 is the detailed temperature transport function in sigma coordinate.

$$Accumulation = inflow - outflow \pm surface\ heat\ exchange$$

(1.10)

$$H_{net} = H_S + H_L + H_E + H_C$$

(1.11)

Where H_{net} = net heat flux across the air/water interface, H_s = shortwave solar radiation flux, H_L= net longwave radiation flux from the atmosphere and the waterbody, H_E = latent heat flux due to evaporation, and H_C = sensible heat flux due to conduction.

$$\frac{\partial(HT)}{\partial t} + \frac{\partial(HuT)}{\partial x} + \frac{\partial(HvT)}{\partial y} + \frac{\partial(wT)}{\partial z} = \frac{\partial}{\partial z}\left(\frac{A_b}{H}\frac{\partial T}{\partial z}\right) + \frac{\partial I}{\partial z} + Q_T$$

(1.12)

Where I = solar radiation and Q_T = horizontal turbulent diffusion and external source/sinks.

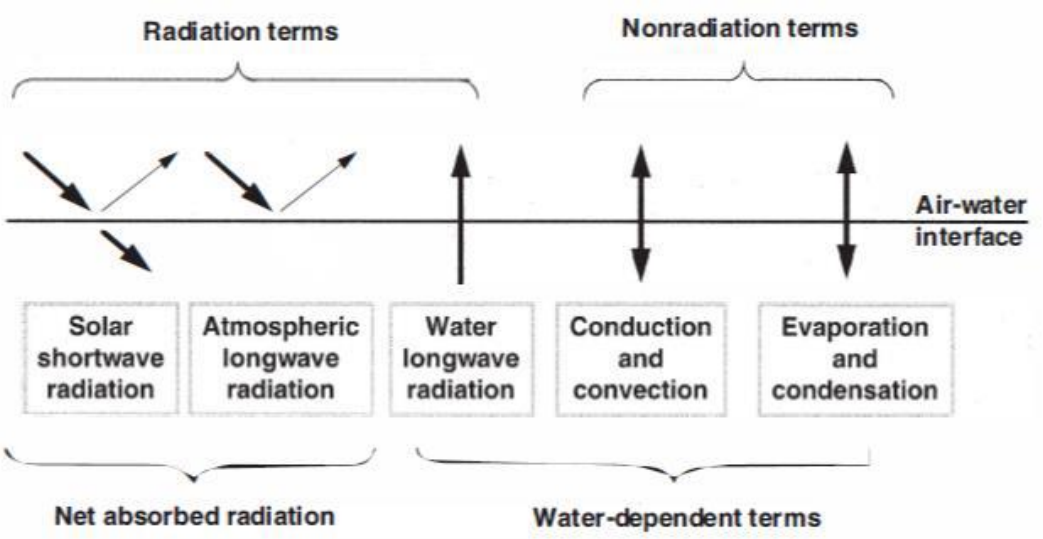

Figure 1-3 Radiation and non-radiation terms affecting water temperature

1.3.2.3 Water Quality Modeling

The water quality or eutrophication model focuses on spatial and temporal changes in DO linked with algae and nutrients. Nutrients such as nitrogen, carbon, and phosphorus provide the material for algae growth, producing oxygen through photosynthesis. In turn, the decomposition of dead phytoplankton contributes to the source of the nutrients.

Nitrogen has two forms, inorganic and organic (Equation 1.13). Organic nitrogen is derived from decomposition of organisms and plants. Organic nitrogen can be divided into three forms: refractory, labile, and dissolved, based on the time scale for decomposition. The labile form often has a rapid decomposition period (weeks to months) while the refractory form needs years to decompose. The labile and particulate form dissolute to dissolved organic nitrogen. Ammonia, nitrate, and nitrogen gas are the inorganic forms of nitrogen. Nitrogen gas in the atmosphere can only be absorbed and utilized by blue-green algae, which can be present in varying abundance depending on the waterbody. Ammonia and nitrate are the only forms of nitrogen suitable for algal growth. Although algae prefer to uptake nitrogen as ammonia, nitrate

can also be directly utilized by algae for growth. Organic nitrogen can convert to ammonia through mineralization or decomposition, while nitrate can be generated through the nitrification process, with ammonia oxidization in the presence of nitrifying bacteria and oxygen. When DO is limited, nitrogen gas will be produced from nitrate through the denitrification process. Algae then utilize inorganic nitrogen, and organic nitrogen is released when the algae die. The conceptual equations for the change of all forms of nitrogen are listed from Equation 1.13 to Equation 1.17 including total nitrogen (TN), particulate organic nitrogen (PON), dissolved organic nitrogen (DON), ammonia (NH4) and nitrate (NO3).

$$TN = NO_2 + \frac{NH_3}{NH_4} + ON \tag{1.13}$$

$$The\ change\ of\ PON = Algal\ basal\ metabolism + algal\ predation - PON\ analysis - settling + external\ source \tag{1.14}$$

$$The\ change\ of\ DON = Algal\ basal\ metabolism + algal\ predation - PON\ analysis - mineralization + external\ source \tag{1.15}$$

$$The\ change\ of\ NH_4 = Algal\ contributions + DON\ mineralization - nitrification + botton\ flux\ of\ NH_4 + external\ source \tag{1.16}$$

$$The\ change\ of\ NO_3 = -Algal\ uptake + nitrification - denitrification + botton\ flux\ of\ NO_3 + external\ source \tag{1.17}$$

Like nitrogen, phosphorus also has an organic and inorganic form. It is a key nutrient for algal growth because it can convert sunlight into usable energy forms. Compared with nitrogen, phosphorus is a common limiting nutrient for algal growth in a waterbody. EFDC+ simulates

two organic forms of phosphorus: Particulate Organic Phosphorus (POP) and Dissolved Organic Phosphorus (DOP). One reason is that the source of phosphorus is often limited, unlike organic nitrogen which can be obtained from nitrogen gas in the atmosphere through the fixation process. The second reason is that phosphorus is a very reactive compound. Rapid reactions with other cations reduce the amount of inorganic phosphorus which is the suitable form for algal growth. As in the nitrogen cycle, organic phosphorus originates primarily with decomposition of dead algae. Inorganic phosphorus can be converted from the organic form through the mineralization or decomposition process. Unlike the two forms of inorganic nitrogen (ammonia and nitrate), there is only one inorganic phosphorus form, orthophosphate, that is suitable for algal growth. Additionally, phosphorus does not exist in the gas phase. The conceptual equation for the change of Total Water Phase Phosphate (TP), POP and DOP are listed from Equation 1.18 to Equation 1.20.

$$\begin{aligned} The\ change\ of\ TP = {} & Algal\ metabolism + algal\ predation + mineralization - \\ & settling\ of\ sorbed\ Phosphate \pm \\ & exchange\ of\ dissolved\ Phosphate\ at\ the\ sediment\ interface + \\ & external\ source \end{aligned} \tag{1.18}$$

$$\begin{aligned} The\ change\ of\ POP = {} & Algal\ basal\ metabolism + algal\ predation - POP\ hydrolysis - \\ & settling\ + external\ source \end{aligned} \tag{1.19}$$

$$\begin{aligned} The\ change\ of\ DOP = {} & Algal\ basal\ metabolism + algal\ predation + POP\ hydrolysis - \\ & mineralization + external\ source \end{aligned} \tag{1.20}$$

Algae is the primary producer in surface water through photosynthesis of sunlight to convert carbon dioxide and nutrients to new organic material, releasing oxygen. There are three types of algae commonly found in surface water bodies: blue-green algae, diatom algae, and green algae, respectively. Blue-green algae is unique in that it can fix the nitrogen gas in the atmosphere. This characteristic makes it extremely tolerant of environmental stress. With this attribute, nitrogen is not a limiting nutrient for blue-green algae growth. Diatom algae is unique due to its silica cell wall structure. This algae requires silica in their metabolic activity and is dependent on the presence of dissolved silica for survival. Green algae are the most common algae. Their growth is limited to all the nutrients. The conceptual representation of the change of algae is shown in Eq. 1.21.

$$Net\ algal\ production = algal\ growth - metabolism - predation - settling + external\ source \quad (1.21)$$

DO is the critical parameter in water quality analysis. DO calculations involve several physical and chemical factors such as solubility, transport, production, and consumption of DO. The factors affecting changes in DO can generally be divided into two groups: sinks and sources, as shown in Equation 1.22. Detailed equation of DO calculation is given in Equation 1.23.

$$Net\ change\ of\ DO = photosynthesis - respiration - nitrification - DOC\ decomposition - COD + Reaeration - SOD + external\ loads \quad (1.22)$$

$$\frac{\partial DO}{\partial t} = \sum_{x=c,d,g}((1.3 - 0.3\ PN_x)P_x - (1 - FCD_x)\frac{DO}{DO+KHR_x}BM_x)AOCR.B_x - AONT.Nit.NH_4 - AOCR.K_{HR}.DOC - \frac{DO}{KH_{COD}+DO}K_{COD}.COD + K_r(DO_S - DO) + \frac{SOD}{\Delta z} + \frac{WDO}{V} \quad (1.23)$$

where PNx = preference for ammonium uptake by algal group x ($0 \leq PNx \leq 1$); $AONT$ = mass of DO consume per unit mass of ammonium nitrogen nitrified; $AOCR$ = dissolved oxygen/carbon ratio in respiration; K_r = reaeration coefficient(day^{-1}); DO_S = saturation concentration of dissolved oxygen (g O_2/m^3); SOD = sediment oxygen demand (g $O_2/m^2/day$); WDO = external loads of dissolved oxygen (g O_2/day).

1.4 Dissertation Organization

Chapter 1 is the introduction that describes the background of the whole study, the study area, and the description of MINLAKE and EFDC models.

Chapter 2 describes the development of lake eutrophication model MINLAKE2020. Nitrogen, Phosphorus, DO and inflow-outflow submodels are included into MINLAKE2012 to develop the updated version 2020. The model was tested using six lakes with varying characteristics. This work has already been published as a peer-reviewed journal *Water* (2021) titled "Simulating Nutrients and Phytoplankton Dynamics in Lakes: Model Development and Applications."

Chapter 3 includes the comparison of 1-D MINLAKE2020 and 3-D EFDC+ models for three lakes in Minnesota. The models were compared based on water temperature, DO simulation and inflow distributions. This work will be submitted to Water journal (2023) for review titled " Comparing 1-D and 3-D Water Temperature, Ice Cover, and Dissolved Oxygen Modeling in Three Minnesota Lakes."

Chapter 4 presents the model development and calibration of EFDC+ model for Cotton Bayou. It includes the description of the input data, source of calibration data, model calibration parameters and calibration results for the simulation periods (11/07/2023- 2/20/2023 and 05/01/2023-07/10/2023) for water level, water temperature and DO.

Chapter 5 focuses on the predictive modeling of the potential restoration techniques using the model calibrated in Chapter 4. The best restoration technique to resolve the issue of low DO (which causes fish kill) is selected and discussed here.

Chapter 6 presents the effect of future climate and sea level rise on the existing condition model (Chapter 4) and the selected predictive model (Chapter 5) for the Cotton Bayou-Terry Cove area.

Chapter 7 presents a summary of all the findings from Chapter 2 through Chapter 6.

Chapter 2 Lake Eutrophication Modeling Without/With Inflows-Outflows

2.1 Lake Eutrophication Modeling

Various lake/reservoir water quality models have been developed and applied to understand the environmental health of fresh waterbodies. LAKE2K is a one-dimensional lake water quality model which simulates carbon, nitrogen, oxygen, phosphorus, silica concentrations, and phytoplankton and zooplankton biomass using water balance, heat balance, and mass balance for the epilimnion, metalimnion, and hypolimnion (three layers) of a lake (Chapra & Martin, 2004). A two-dimensional hydrodynamic and water quality model, CE-QUAL-W2 (originally developed in 1990s) can be used in rivers, lakes, reservoirs, estuaries, and even a combination of river segments and multiple reservoirs but is more suitable for relatively long and narrow water bodies (Cole & Wells, 1995). PCLake (1990) is a process-based model to simulate water quality in shallow, non-stratifying lakes in temperate climate zones with a uniform daily time-step for processes. The recent version of PCLake, PCLake+ simulates basic stratification in temperature using mixing depth and two layers: epilimnion and hypolimnion only (Janssen et al., 2019). EFDC is a state-of-the-art, versatile model that can simulate one-, two- or three- dimensional flow, transport, and biogeochemical processes in surface water systems such as rivers, lakes, estuaries, and reservoirs. In Lake Pusiano, Carraro et al. (2012) validated the 3D model ELCOM coupled to the biological model CAEDYM with high frequency measurements to identify the factors (including hydrodynamic factors) which drive the spatial distribution of cyanobacteria in the lake. Though EFDC and ELCOM-CAEDYM are very flexible and support a variety of conditions, the complexity of these models makes them difficult to apply when data are scarce. Each of these models have limitations such as modeling for a certain type of waterbody (PCLake) or certain parameters (MINLAKE2012) or ignoring some physical

processes (CE-QUAL-W2 and Lake2K), complexity of the model (EFDC and ELCOM-CAEDYM). In order to improve operational control of algal blooms and management applications, models are often integrated into warning systems to predict short-term phytoplankton blooms to improve operational control of cyanobacterial blooms (Shimoda & Arhonditsis, 2016). For example, the EcoTaihu model has been integrated into a Windows software platform to predict algal blooms in Lake Taihu (Zhang et al., 2015). The PROTECH model was used to study the effect of an increase in water temperature and phosphorus loading on phytoplankton in Lake Windermere (Elliott, 2011).

High phosphorus release from lake sediments is frequently reported as an important mechanism delaying lake recovery after external loading of phosphorus has been reduced (Marsden, 1989; Philips et al., 2005; Sondergaard et al., 2005). A study of 78 stormwater ponds revealed that more than one-third of the sampled ponds may experience internal loading (Taguchi et al., 2020). A long-term survey of 35 lakes in Europe and North America concluded that internal release of phosphorus typically continues for 10–15 years after the external loading reduction (Jeppesen et al., 2005), but in some lakes, the internal release may last longer than 20 years (Sondergaard et al., 2005). In shallow lakes, it is common to observe negligible changes in phosphorus concentrations in lake water even after external load diversion (Welch & Cooke, 2009). For example, Lake Trummen in Sweden remained hypereutrophic even after 11 years of sewage diversion (primary source of external phosphorus loading), and the removal of 1 m of high phosphorus sediment reduced internal loading dramatically (Welch & Cooke, 2009).

2.2 MINLAKE2020-Nutrient Submodel

To provide better lake management and restoration strategies, a deterministic, one-dimensional water quality model MINLAKE2020 was modified from daily MINLAKE2012 by

incorporating chlorophyll-a, nutrients, and inflow-outflow submodels into the existing regional year-around temperature and dissolved oxygen (DO) model. In MINLAKE2020, the Chlorophyll-a (Chl*a*) model was modified to overcome the limitations of previous MINLAKE models. The model can simulate up to three algal groups (diatoms, green algae, and blue-green algae). The algal groups are distinguished by different rates of photosynthesis, respiration, settling, zooplankton grazing, and different nutrient requirements. Phytoplankton growth depends on the maximum growth rate of the algae, half-saturation coefficients for nutrients, water temperature, solar irradiance, external nutrient concentrations, and the current Chl*a* concentration. Phytoplankton populations are removed from a water column by four processes: respiration, mortality, settling, and zooplankton grazing. Each phytoplankton population is assigned a fixed or calibrated respiration rate, mortality rate, and settling rate. Respiration affects the available phosphorus and Dissolved Oxygen (DO) immediately whereas mortality contributes to the available phosphorus and DO with a time lag through detrital decay. The Michaelis-Menten equation is used to simulate the effect of Chl*a* concentration on grazing. It is assumed that no grazing occurs below a threshold Chl*a* concentration.

$$Change\ of\ Chlorophyll\text{-}a = Diffusion + Settling + Mortality + Respiration + Growth - Zooplankton\ Grazing$$

(2.1)

Algae need both nitrogen and phosphorus for growth. However, phosphorus is particularly important for algal growth as it is usually in short supply compared to other nutrients. In most cases, phosphorus is known to be the primary nutrient controlling the trophic state of lakes in the Upper Midwest USA and Canada (Dillon & Rigler, 1974). Phosphorus accumulated from detrital biomass, sediment release, and respiration are used by phytoplankton, in the presence of sunlight,

for growth. If it is assumed that nitrogen is in abundant supply, phosphorus becomes the only limiting nutrient for algal growth (green and blue-green algae), which is modeled in the application of MINLAKE2020. Uptake depends on the maximum growth rate, light limitation, nutrient limitation, Chl*a* concentration at that time, and the yield ratio of phosphorus to Chl*a*. The differential equation representing Soluble Reactive Phosphorus (SRP) fate and transport in a layer is given as Equation 2.2.

$$Change\ of\ Phosphorus = Diffusion + Growth - Detrital\ Decay - Respiration - Sediment\ Release$$

(2.2)

Aquatic organisms and fish depend on the availability of DO in the waterbody. DO is added to a water layer through diffusion and photosynthesis; and is removed by respiration of algae and zooplankton, detrital decay (BOD), sediment oxygen demand (SOD), and nitrification. The surface reaeration can add or remove DO depending on whether surface DO is less or greater than saturated DO (a function of surface temperature and lake elevation). Phytoplankton (modeled as Chl*a*) growth can add DO to the water layer through photosynthesis to the point where water could be supersaturated with DO in some cases. These dynamic processes can happen over time scales of less than one day (the time step of the MINLAKE2020 simulation). Therefore, the model outputs DO profiles as an integration of different physical (e.g., mixing), chemical, and biological processes over the day. DO removal from the water layer through phytoplankton respiration is simulated to occur at a constant rate throughout the day while photosynthesis occurs only during the hours with solar radiation. In MINLAKE2020, the adjustments for low DO levels on SOD, BOD, and algal respiration follow Edwards and Owens's (Edwards & Owens, 1965) formula. SOD is calculated for each layer, and it is treated

as a sink term in the one-dimensional (vertical) transport equation (Thomann & Mueller, 1987) . Oxygen uptake of the sediment depends on the area and composition of bottom materials in contact with the water (Henderson-Sellers, 1984). The differential equation representing DO dynamics in a layer is given as Equation 2.3.

$$Change\ of\ DO = Diffusion - BOD - SOD - Respiration + Photosyntheis - Nitrification + Reaeration\ (surface\ only) - Zooplankton\ Respiration \quad (2.3)$$

2.3 Modeled Lakes

In this study, six lakes (Table 2-1) were selected for model calibration, sensitivity analysis of model parameters/coefficients, and understanding the internal dynamics and cycles of nutrients over multiple years in lakes with different stratification and trophic characteristics: two shallow lakes (Pearl and Carrie), two medium-depth lakes (Riley and Thrush), and two deep lakes (Carlos and Elmo). The maximum depths range from 5.6 to 50.0 m. All six lakes are located in northeastern Minnesota since they have the necessary data for the study. Weather data were provided by the weather stations nearest each lake: St. Cloud Regional Airport for Pearl, Carrie, and Carlos lakes; Duluth International Airport for Thrush and Riley lakes; and Minneapolis/St. Paul International Airport for Lake Elmo. The geometry ratio ($GR = A_s^{0.25}/H_{max}$, A_s in $m^{2,}$ and H_{max} in m being the surface area and the maximum depth of the lake) is an important characteristic parameter of a lake related to stratification, lake habitat, etc. (Stefan et al., 1996). The lake geometry ratio for the lakes varies between 0.75 and 7.53. Lower lake GR generally indicates stronger lake stratification. Two medium-depth (6 m < $H_{max} \leq$ 20 m, (Stefan & Fang, 1994)) and two deep lakes (H_{max} > 20 m, (Stefan & Fang, 1994)) selected for the study are strongly stratified (geometry ratio less than 3), one medium-depth and one shallow lake are weakly stratified (geometry ratio between 3 and 10). Based on Chl*a*, Pearl Lake, Carrie Lake, and Riley Lake are eutrophic (mean Chl*a* > 10 µg/L (NAS and NAE, 1973)), Lake Elmo and Lake Carlos are mesotrophic lakes (mean Chl*a* between 4 and 10 µg/L (NAS and NAE, 1973)), and Thrush Lake is an oligotrophic lake. The nutrient model was calibrated and validated based on available measured water temperature, Chl*a*, phosphorus and DO profile data on particular

days, downloaded from the Minnesota Department of Natural Resources (MN DNR) LakeFinder website (https://www.dnr.state.mn.us/ lakefind/index.html).

Table 2-1 Characteristics of Six Study Lakes in Minnesota

Lake	Surface area, As, (km^2)	Max. depth H_{max}, (m)	Geometry Ratio $(m)^{0.5}$	Mean Chl*a* (µg/L)	Trophic Status	Simulation Years	Number of profile days (data points)
Pearl	3.05	5.55	7.53	16.91	Eutrophic	2010–2012	15 (134)
Carrie	0.37	7.90	3.12	6.71	Mesotrophic	2007–2010	36 (342)
Riley	1.19	14.9	2.22	24.00	Eutrophic	1985–1987	16 (148)
Thrush	0.048	14.63	1.01	1.71	Oligotrophic	2008–2015	18 (100)
Elmo	1.039	42.63	0.75	4.45	Mesotrophic	1989–2009	70 (864)
Carlos	10.54	50.00	1.15	3.84	Oligotrophic	2008–2015	54 (308)

2.4 Model Calibration

For the application of MINLAKE 2020 to the six study lakes, the temperature model was calibrated first and then the nutrient model was calibrated. Temperature model calibration ensured that thermal and mixing dynamics were modeled accurately because water temperature and mixing dynamics directly affect nutrients, chlorophyll, and zooplankton processes. The wind sheltering and the multiplier for diffusion coefficient in metalimnion are the main calibration parameters for temperature modeling. Although MINLAKE2020 has an integrated nitrogen model, for this study, only phosphorus was simulated since phosphorus is the limiting nutrient in these six lakes. Green algae and blue-green algae were simulated separately and then combined to represent the total Chl*a* concentration. The MINLAKE2020 development also included the

inflow and outflow subroutines from MINLAKE87, which were tested/verified to ensure they function appropriately; however, the inflow/outflow function was not activated for the simulation of the six study lakes (Table 2.1). Limited inflow and outflow are available for Carrie, Pearl, and Carlos Lake (Engel et al., 2012; Engel et al., 2010); inflows in the other three lakes are negligible, and inflow water quality data (nutrients and phytoplankton) are scarce. The approximation of not inflow/outflow is appropriate since the study objective is to examine/understand the internal dynamics and cycles of nutrients over multiple years in six lakes with different stratification and trophic characteristics.

Figure 2-1 shows an example of the calibration results of water temperature and DO time series at two depths (1 m and 7 m) at Lake Carrie including measured data. During 2008–2010, Lake Carrie had measured water temperature and DO profile data for 36 days or 342 data points in total. MINLAKE2020 simulated water temperature and DO with a root mean square error (RMSE) of 1.75^{o}C and 1.95 mg/L, respectively. Corresponding regression coefficients of measured versus simulated (R^2) are 0.99 and 0.93, respectively. The statistical results summarized in Table 2-2 show that for the six lakes, MINLAKE2020 model performed better than MINLAKE2012 (RegDO model), especially for DO simulations, when simulated profiles were compared with observed profiles. The main reason for this improvement is the simulation of Chl*a* concentration on daily time step rather than using the specified pattern of observed data. Table 2.2 shows the model performance improved significantly with the MINLAKE2020 (NCDO model) in Carlos and Thrush lakes. The average RMSE of DO simulations in six lakes from MINLAKE2020 decreased by 24.2%, and average Nash-Sutcliffe efficiency (NSE) (Nash & Sutcliffe, 1970) also increased with respect to MINLAKE2012. Chl*a* concentration affects the solar radiation attenuation in the water column and then affects water temperature simulation as

shown in Table 2-2 even though the average RMSE, NSE, and R^2 for temperature (regression coefficient of measured versus simulated) from the two models are almost the same.

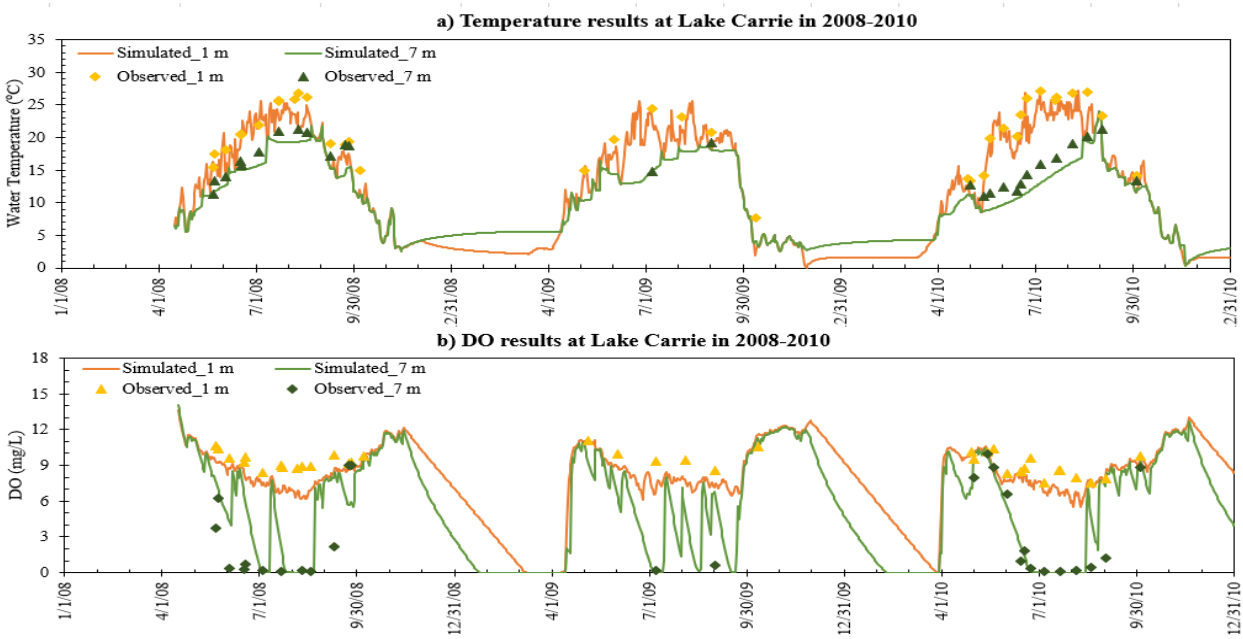

Figure 2-1 Time series of simulated a) water temperature and b) DO at two depths in Lake Carrie in 2008–2010.

Table 2-2 Statistical Parameters for Six Lakes (Simulated Profiles were Compared with Observed)

	NCDO Model (MINLAKE2020)					
	Water Temperature			Dissolved Oxygen		
Lake Name	RMSE [a] (ºC)	NSE [b]	R^2 [c]	RMSE (mg/L)	NSE	R^2
Lake Elmo	0.98	0.98	0.99	2.02	0.70	0.92
Lake Carlos	1.66	0.83	0.97	2.39	0.61	0.90
Riley Lake	1.50	0.50	0.98	1.79	0.80	0.93
Thrush Lake	1.88	0.70	0.95	2.43	0.40	0.92
Carrie Lake	1.75	0.68	0.99	1.95	0.70	0.93
Pearl Lake	1.30	0.87	0.97	3.42	-0.12	0.87
Average ± STD [d]	1.51±0.33	0.76±0.17	0.97±0.01	2.33±0.59	0.52±0.34	0.91±0.02
Lake Name	RegDO Model (MINLAKE2012)					
Lake Elmo	1.03	0.98	0.99	1.89	0.70	0.92
Lake Carlos	1.52	0.85	0.98	4.15	-0.19	0.85
Riley Lake	1.55	0.5	0.98	2.61	0.55	0.91
Thrush Lake	2.01	0.69	0.95	2.91	0.1	0.92
Carrie Lake	1.76	0.64	0.99	1.98	0.69	0.94
Pearl Lake	1.04	0.97	0.98	3.30	0.01	0.89
Average ± STD	1.49±0.39	0.77±0.19	0.98±0.02	3.08±1.11	0.11±0.69	0.90±0.03

Note: [a] – RMSE stands for Root Mean Square Error, [b] – NSE for Nash-Sutcliffe Efficiency (Nash & Sutcliffe, 1970), [c] – R^2 stands for regression coefficient of measured versus simulated, [d] – STD for Standard Deviation.

For Chl*a* simulation of the six lakes, RMSE ranges from 0.0006 to 0.0276 mg/L. Figure 2-2(a) shows an example comparison between simulated Chl*a* of NCDO model and specified Chl*a* from RegDO model for Lake Elmo. From 1980 to 2018, there were 74 days in 10 years with measured temperature and DO profiles (1506 data points) for model calibration but no profile data in 2007 and 2009. The average chlorophyll concentration was 0.0075 mg/L in 74 days but 0.0036 mg/L over 10 days in 2008. Even though there were no profile data in 2009, we identified some Chl*a* data in 2009 as shown in Figure 2-2(a). MINLAKE2012 uses the annual mean Chl*a* concentration and seasonal variation patterns (Fang & Stefan, 1994) (depending on trophic status) to specify daily Chl*a* for DO simulation. Therefore, the RegDO model had higher Chl*a* in 2007 and 2009 due to the lack of available profile data in these two years whereas the NCDO model predicts the Chl*a* reasonably well in 2008 and 2009 when comparing with data.

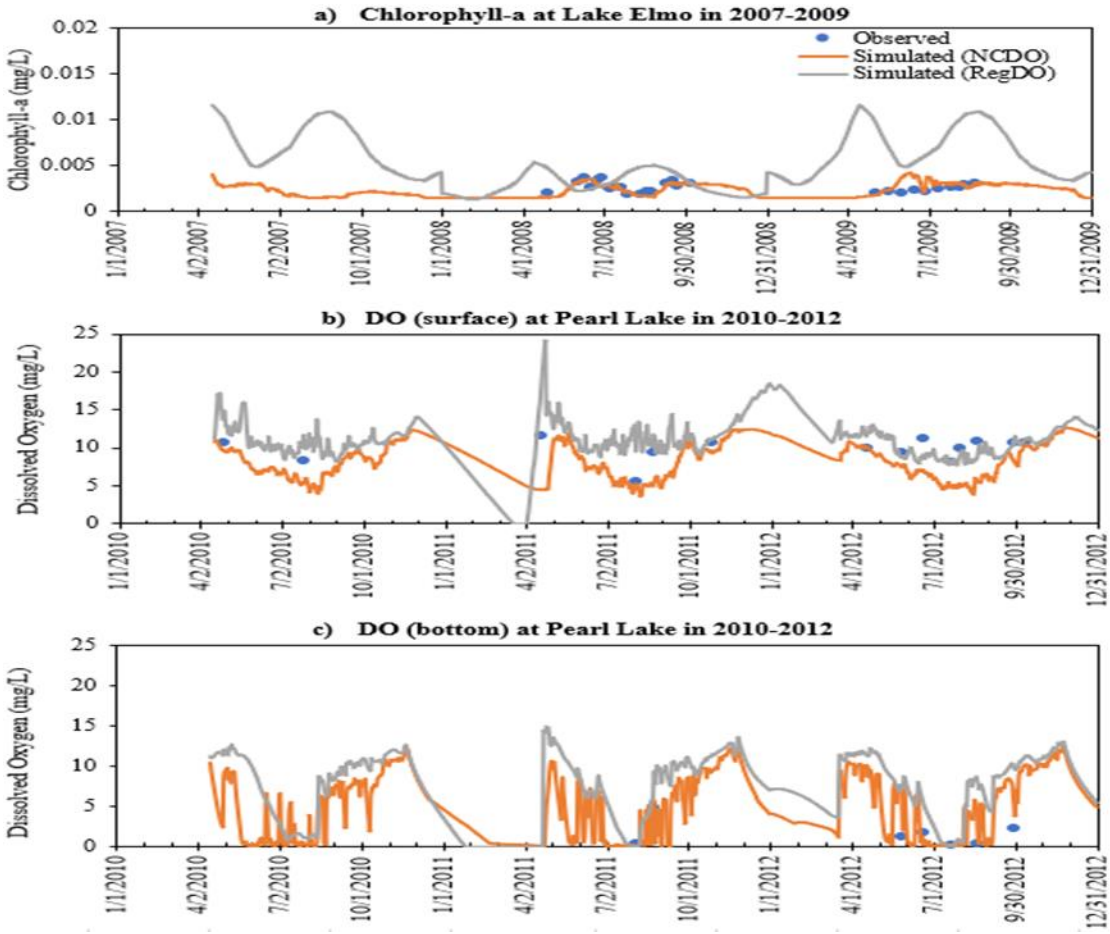

Figure 2-2 a) Simulated (NCDO model and RegDO model) and observed Chl*a* near the surface in Lake Elmo in 2007–2009, b) and c) simulated and observed DO near the surface (1 m) and bottom (5 m) in Pearl Lake in 2010–2012, respectively.

Some lakes such as Lake Elmo and Carrie Lake (Table 2-2) do not exhibit a noticeable change in simulated DO concentrations based on the model used for simulation. Some lakes, e.g., Pearl Lake, exhibit a noticeable change in simulated DO concentration depending on the model (RegDO or NCDO model). Figure 2-2(b) and (c) show the time series of DO concentrations simulated by the NCDO model and RegDO model including observed DO at the surface (1 m) and near the bottom (5 m) of Pearl Lake in 2010–2012, respectively. The RegDO model somewhat over-predicts surface DO concentration, but the NCDO model under-predicts

surface DO. The RegDO model over-predicts DO at the bottom layer. When BOD is simulated, the winter DO decreases predicted by MINLAKE2020 are smaller than that predicted by MINLAKE2012 (when BOD is specified as a part of the model inputs). There are a limited amount of measured phosphorus data to compare to model simulations results, and so this parameter should not be used to judge model performance. However, there are sufficient measured DO data to compare to simulated DO and thus DO is an appropriate parameter to judge overall model performance.

2.5 Results and Discussion

2.5.1 Chlorophyll-a and Phosphorus Profiles

Lake Elmo was extensively monitored in 1988 by the Metropolitan Council at St. Paul, MN (Osgood 1989) and had measured phosphorus concentration data at five depths (0, 8, 16, 24, and 32 m) and DO data at 31 depths for open water season. The comparison between simulated and observed concentrations for Chl*a*, phosphorus, and DO on three days in 1988 is presented in Figure 2-3. Since Lake Elmo is a deep lake and solar radiation cannot penetrate below the euphotic zone, the Chl*a* concentration becomes zero in the deep layers. On April 11th, 1988, the lake was more, or less well mixed and phosphorus concentration did not vary much throughout the depth. DO concentration gradually declined along with depth due to the contribution of more sink terms (Equation 2.3), however, slope was not steep in the profile plot. The Chl*a* concentration is highest at the surface with little variation throughout the depth. On 18th May 1988, stratification increased and simulated DO at the bottom is near zero. The maximum Chl*a* concentration occurs at 8 m depth from the surface. The phosphorus concentration is higher in the deeper layers because of detrital decay and phytoplankton respiration. On 19th October 1988, phosphorus near the surface layer was consumed by phytoplankton for growth, and the lake

became strongly stratified. The bottom layers of the lake became anoxic, and phosphorus released from sediment contributed to the higher phosphorus concentration at deeper depths, increasing along with depth from metalimnion and hypolimnion.

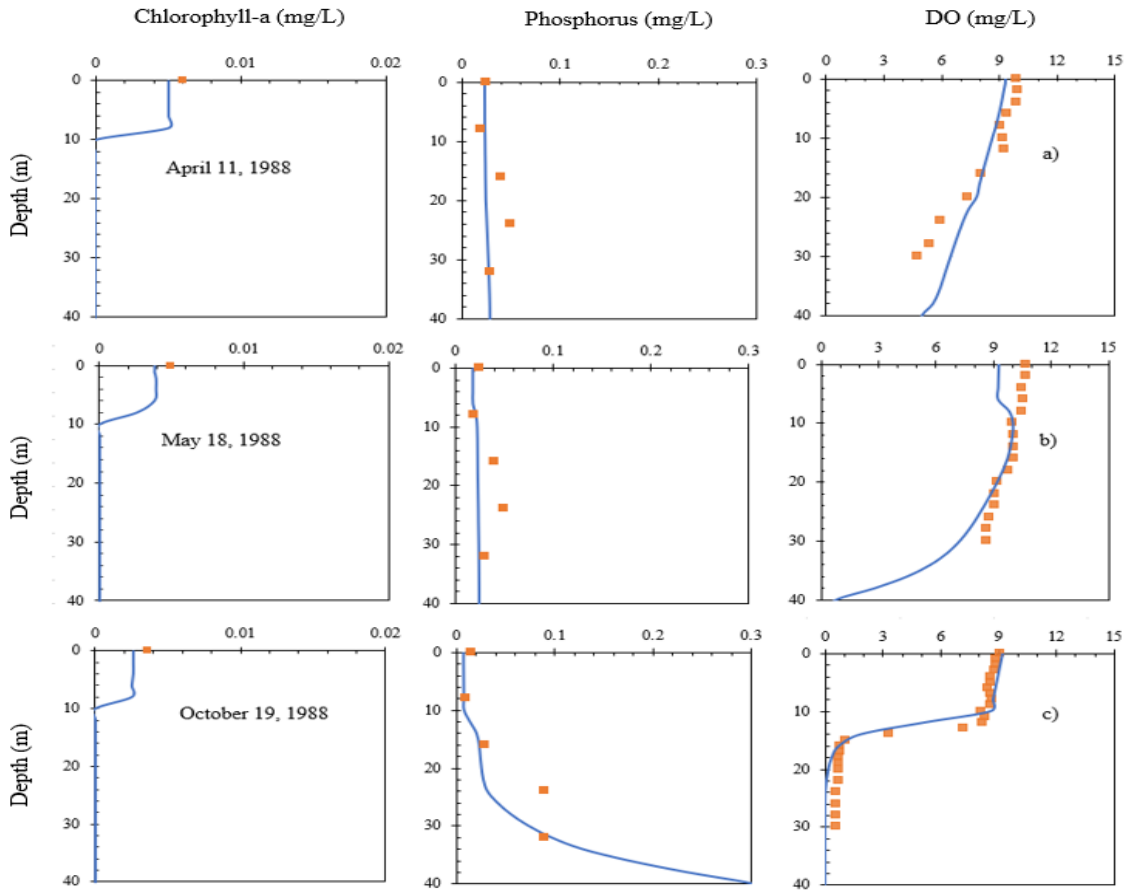

Figure 2-3 Simulated (line) and observed (dots) Chla, phosphorus, and DO profiles for Lake Elmo on a) 11 April, b) 18 May, and c) 19 October 1988.

2.5.2 Chlorophyll-a and Phosphorus Interaction

Figure 2-4 and Figure 2-5 show examples of simulated time series of P, Chl*a*, and DO with observed data for a deep lake (Lake Elmo) and a shallow lake (Carrie Lake), respectively. Figure 2-4 shows simulated and observed Chl*a* and phosphorus at three depths (at 1 m, 20 m, and 40 m from the surface) of Lake Elmo from 4-16-2007 to 12-31-2009. This is a continuous

two year simulation including two open-water seasons and two ice cover periods, which is the first time MINLAKE has been used for a simulation over this timespan. The first simulation year can be considered a transient, or "warm-up" period with potentially higher uncertainties in results due to the assumed initial conditions. For example, the low phosphorus concentration from the water surface to 20 m during the open water season (Figure 2-5(a) and Figure 2-5(b)). The simulated ice cover periods were from 12-5-2007 to 4-16-2008, 12-7-2008 to 4-10-2009 for Lake Elmo, which are marked by blue shaded regions in Figures 2-5(a) and 2-5(b).

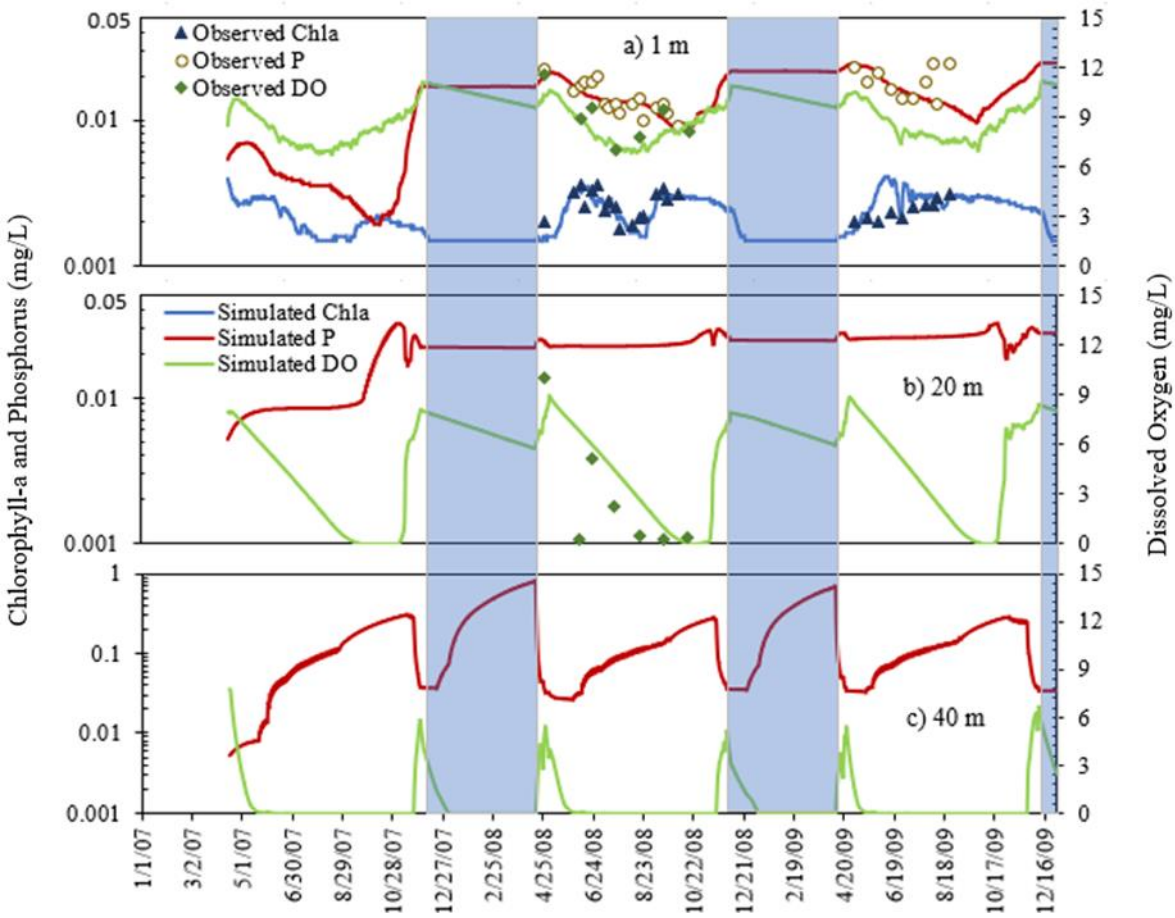

Figure 2-4 Simulated and observed Chl*a*, phosphorus, and DO concentration at a) 1 m, b) 20 m, c) 40 m depth from the surface at Lake Elmo in 2007–2009 (blue shaded area represents the ice cover period). The scale for the major y axis in c) is larger than one in a) and b).

Near the water surface (1 m), DO concentrations were near saturation as a function of temperature (lowest DO in the middle of summer) and ranged from 6.69–11.13 mg/L. From late October to late November, before ice began forming at the surface of the lake, phosphorus at the surface and near-surface layers began increasing due to more mixing and fall overturns. This increase is more evident in 2007 when phosphorus was low in the summer. During the ice cover period, the phosphorus concentration at 1 m and 20 m stabilized as photosynthesis slowed due to near-zero water temperatures and reduced sunlight (attenuated by snow cover). After the ice melted in late spring, simulated phosphorus concentrations at 1 m increased for a brief period due to spring overturn, before decreasing as phosphorus was utilized by phytoplankton. During the early summer (May) of 2008 and 2009, simulated Chl*a* concentrations increased gradually from 0.0016 mg/L to a maximum of 0.0033 mg/L (observed on June 15th).

At the deep layers (e.g., 20 and 40 m), DO became anoxic during the summer at deep hypolimnion since Lake Elmo was strongly stratified. Anoxic periods at 20 m and 40 m were on average 12 days and 210 days per year from 2007 to 2009, respectively. In the deeper layers, in addition to detrital decay and phytoplankton respiration, sediment release could add up to the available phosphorus. Since there was a long period of anoxic condition at 40 m during the summer, early fall, and some part of the ice cover period, phosphorus release from sediment contributed to a major portion of phosphorus increase. Phosphorus peaks in deepest layers were simulated to occur just after the anoxic condition ended and before the fall or spring mixing/overturns. These overturns sharply reduced phosphorus in very deep layers (e.g., 40 m) and increased phosphorus in other shallower layers. The calculated euphotic depth was 9 m for the simulation period; therefore, there was no photosynthesis below this depth and simulated

Chl*a* was zero at 20 m and 40 m. Chl*a* is typically measured near the surface; therefore, there is no measured Chl*a* at the deep depths to compare with simulated values.

Figure 2-5 shows simulated and observed P, Chl*a*, and DO at two depths (at 1 m, 7 m from the surface) of Carrie Lake from 16th April 2007 to 31st December 2009. The calculated euphotic depth ranged from 3.75 m to 4.23 m from the surface; therefore, the Chl*a* was zero at the bottom layers (e.g., 7 m). Phosphorus release from sediments due to anoxic conditions under the ice cover periods for both 2008 and 2009 winter was not only at 7 m but also at 1 m (does not happen in deep lakes like Lake Elmo) and triggered algal bloom at 1 m in early summer of 2008 and 2009 (after ice melting). During the summer of 2008 and 2009, the concentration of DO gradually increased at the surface, and sediment phosphorus release decreased which resulted in a gradual decrease in phosphorus concentration. The DO concentration decreased with depth because of no photosynthesis in the deeper layers (below the euphotic zone) plus sedimentary oxygen demands. Simulated DO at 7 m had some fluctuations in the summer of 2008 and 2009 due to short period strong mixing and results in anoxic conditions only in a few days. The simulated high phosphorus concentrations directly corresponded to the simulated anoxic DO conditions in the 2008 and 2009 winters (Figure 2-5(b)).

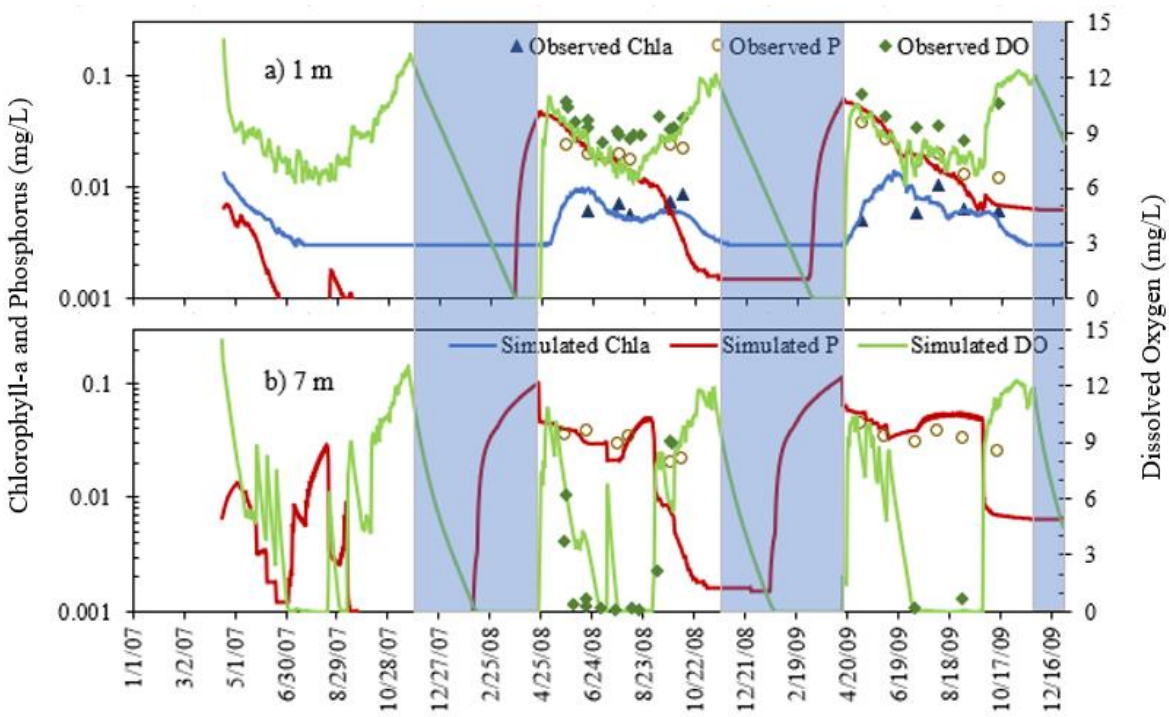

Figure 2-5 Simulated and observed Chl*a*, phosphorus, and DO concentration at a) 1 m and b) 7 m depth from the surface at Carrie Lake in 2007–2009 (blue shaded area represents the ice cover period).

2.5.3. Long-term Simulations Using MINLAKE2020

West and Stefan (West & Stefan, 1998) performed a multiple-year simulation (same calibration parameters) using MINLAKE98 for Lake Riley and Lake Elmo. For Lake Riley, a different set of calibration parameters was needed for different years whereas, for Lake Elmo, the model could simulate successfully for 1985–1990 with the regression coefficient for temperature and DO as 0.91 and 0.79, respectively. For a simulation of 1985–1990 using the MINLAKE2020 NCDO model, the regression coefficient for temperature and DO are 0.9944 and 0.9715 against 146 profile data points, respectively. Simulated phosphorus and Chl*a* concentrations at different depths were satisfactory as well. MINLAKE2020 performed well for multiple-year simulation allowing the user to simulate 20 consecutive years with the same calibration parameters (Figure

2-6). For a 30-year simulation (1989–2009) using the MINLAKE2020 NCDO model, the regression coefficients for temperature and DO are 0.9888 and 0.9419 against 864 profile data points, respectively. The simulated Chl*a* and phosphorus matched reasonably well with observed values with the same trend. Moreover, the phosphorus and Chl*a* concentration at five simulation depths (1 m, 8 m, 12 m, 20 m, and 30 m) matched well with the available observed data.

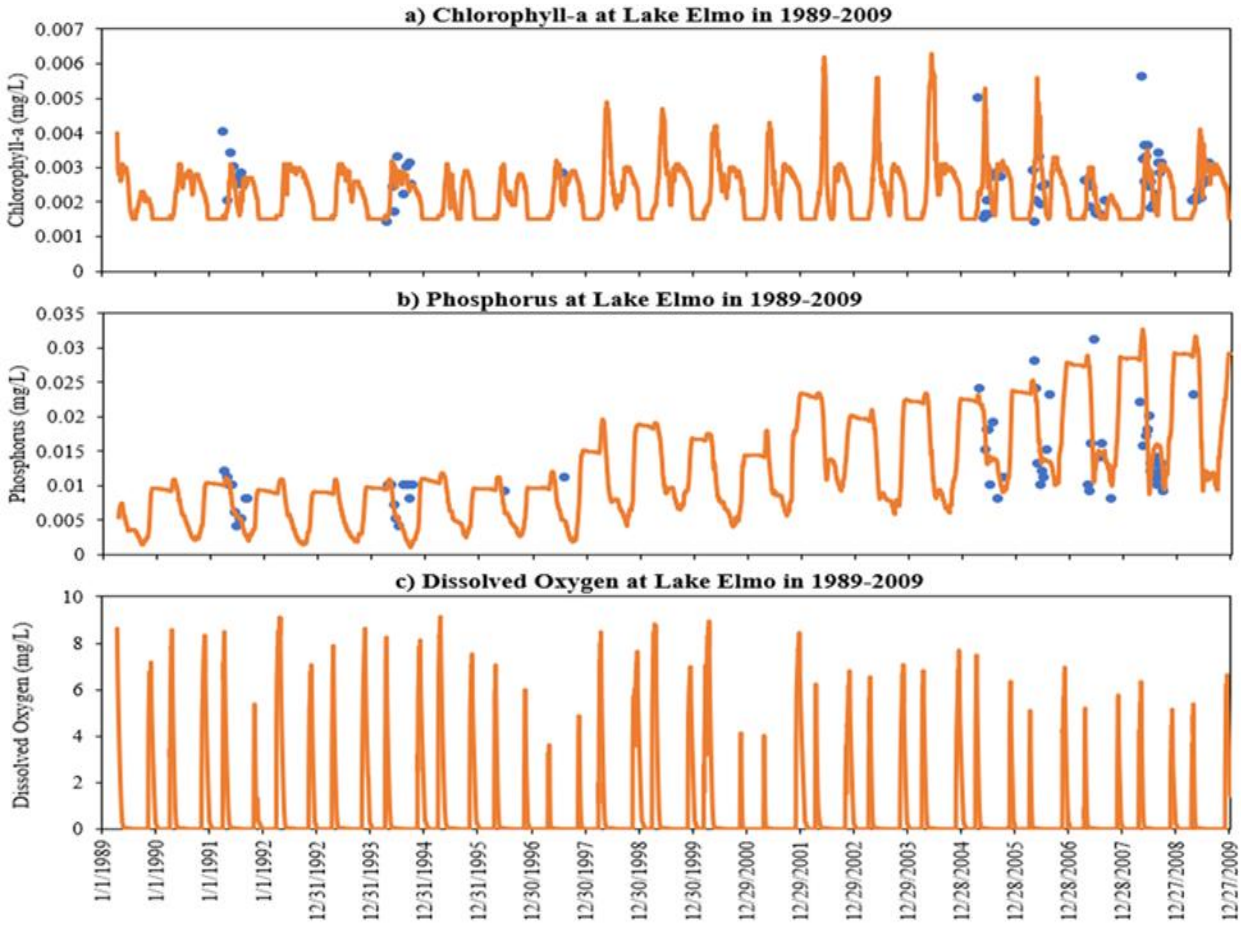

Figure 2-6 Simulated (line) and observed (dots) surface (1 m) a) Chl*a*, b) phosphorus, and c) DO for long-term simulation of Lake Elmo from 1989 to 2009.

From 1989 to 1996, both phosphorus and chlorophyll seasonal variations were reasonably stable. Phosphorus started to increase from 1997 and matched with observed data from 2004 to 2007. The average daily phosphorus was 0.0071 mg/L from 1990 to 1996 and .0158 mg/L from

1997 to 2009. Comparing these two periods, the average daily phosphorus increased by .0087 mg/L. As phosphorus increased, it resulted in some higher peaks in spring algal blooms as shown in Figure 2-6(a). The phosphorus increase trend was caused by the increase in phosphorus release from the lake sediment which is related to the anoxic condition in lakes. Therefore, the phosphorus release for each layer (the last term in Equation 7 times the layer volume) and then each day (sum for all layers) was added together for the annual phosphorus release amount. From 1990 (excluding 1989 for the initial condition effect) to 1996, the average yearly sediment phosphorus release was 151.8 kg (21.27 kg of standard deviation) but from 1997 to 2009 average yearly sediment phosphorus release was 244.1 kg (53.28 kg of standard deviation). The average annual phosphorus release increased by 60.8%. Figure 2-6(c) shows the time series of the simulated DO at 41 m (1 m above the deepest lake bottom) from 1989 to 2009 and clearly shows many anoxic days in the open water seasons and the ice cover periods, which resulted in phosphorus release from sediment. From 1990 to 1996, the average anoxic days was 228 but from 1997 to 2009 average anoxic days was 253 (34 days of standard deviation). An average of 25 days more of the anoxic condition was the major cause for the phosphorus increase trend.

2.6 MINLAKE2020-Inflow Outflow Description

MINLAKE2020, as described in Section 2.2, has an inflow-outflow submodel which allows the user to specify flow, temperature and nutrient concentrations for maximum five inflows/outflows. Limited inflow and outflow are available for Carrie, Pearl, and Carlos Lake (Engel et al., 2012; Engel et al., 2010) inflows in the other three lakes are negligible, and inflow water quality data (nutrients and phytoplankton) are scarce. Lake Carlos, Peral Lake and Carrie Lake has been simulated using the observed inflow-ouflow, and Lake Elmo, Trout Lake and Riley Lake has been simulated using hypothetical inflows.

Inflow and outflow are very important for lake processes, especially if the lake is receiving considerable amount of flow or wastewater discharge. The inflow-outflow subroutine simulates variations in stage throughout the season. The inflow must be in terms of water volume, the temperature of the inflow and concentrations of other state variables. The outflow is simply read in as a negative inflow with zero for the concentration of other state variables. The inflow-outflow subroutine computes to determine that the mass of water and other state variables are conserved. The inflow can be to any layer depending on the density of the inflowing water.

The inflow density usually differs from the density of the lake water surface, so the inflows enter and move through reservoir as density currents. A density current is defined as a gravity flow of liquid or gas through, under or over a fluid of approximately equal density. Contrary to normal fluid flows, in density flow, buoyancy of the surrounding fluid reduces the gravity force by the normalized density difference, $\Delta\rho/\rho$. Density difference is calculated as

$$\varepsilon o = \frac{\rho_{in} - \rho_{mix}}{\rho_{mix}} \tag{2.4}$$

where ρ_{in} is the density of the inflow and ρ_{mix} is the density of the lake water. Depending upon the density difference between the inflow and lake, density currents can enter the epilimnion, metalimnion or hypolimnion. When the inflow density is less than the water-surface density, the inflow will flow over the lake water; this is called overflow (Figure 2-7). This usually happens during spring when the inflowing river water is warmer than the lake water. If the inflow density is greater than the density of the water surface, the inflow will plunge beneath the water surface (Figure 2-7). The position of the plunge point is highly dynamic and changes with both flow and density. The location of the plunge point is more sensitive to changes in flow than to changes in the magnitude of the density difference between the inflow and lake surface water (Ford and

Johnson 1980). After the inflow plunges it can follow the old river channel as underflow. Entrainment of reservoir surface waters into an underflow result from turbulence generated by bottom roughness.

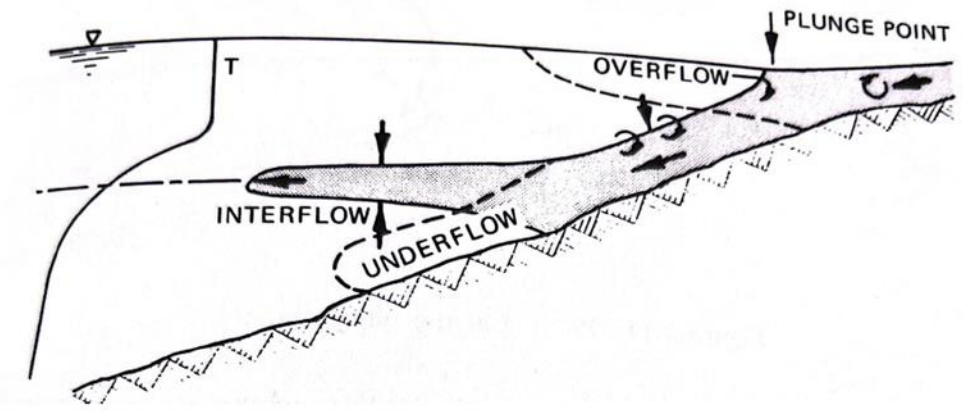

Figure 2-7 Schematic diagram representing how inflow incorporates into lake flow.

The density interflows occurs when a density current leaves the river bottom and propagates horizontally into a stratified body of water. Interflow moves through a lake at a level where the interflow and reservoir densities are similar. Interflows occur when inflow temperatures are less than the water surface temperature and greater than the hypolimnetic water temperature. The level at which an intrusion moves through the reservoir usually depend on the change in inflow densities. Entrainment into an interflow can usually be neglected because the density gradient in the metalimnion creates strong buoyancy forces that inhibit mixing.

Due to density difference between the inflow and the ambient water, the water is entrained from the previous layers. Recent studies have indicated that mixing from meteorological forcing can entrain the inflow constituents into the surface waters (Ford et al. 1980). Based on the inflow density and density current of each layer, the entrainment to or from

each layer is calculated (depending on the deepest layer at plunging point). Depth of plunging point is calculated by

$$h_p = 1.1 * \left(\frac{f*qo^2}{S*\varepsilon og}\right)^{\frac{1}{3}}, \gamma = 0.15 \qquad S \leq 6.667 * 10^{-3} \qquad (2.5)$$

$$h_p = 1.6 * \left(\frac{qo^2}{\varepsilon og}\right)^{\frac{1}{3}}, \gamma = 1.8\text{z} \qquad S > 6.667 * 10^{-3}$$

Here, h_p is the plunging depth, q_o is volume of inflow before plunging, S and f is the slope and Manning's roughness of the inflow channel. γ is initial entrainment at the plunge point. For the layer below the plunging point, the entrainment from a layer into density current is calculated using the following equations (Akiyama & Stefan, 1987).

$$fd = 1.875 \times 10^{-4} + f \qquad (2.6)$$

$$f43 = \left(\frac{fd+\sqrt{fd^2+0.00458*S}}{1.5*S}\right)^{4/3} \qquad (2.7)$$

$$\gamma = 0.0015 * \Delta z * \left(\frac{9.81*\varepsilon o}{qo^2}\right)^{\frac{1}{3}} * \frac{1}{f43*S} \qquad (2.8)$$

$$QE = \gamma * V(dc) \qquad (2.9)$$

For the layers above the plunging point,

$$QE = \frac{Qin(iw)*\Delta z}{\sum z} \qquad (2.10)$$

QE is the entrained flow, *z* is depth, *V(dc)* is the volume of density current. The volume and concentration of the state variables in the receiving layer are adjusted based on the ambient conditions and the volume and concentrations of the water added.

$$Tin(iw) = \frac{Tin(iw)*Qin(iw)+T2(i)*QE(i)}{Qin(iw)+QE(i)} \quad (2.11)$$

$$Qin(iw) = Qin(iw) + QE(i) \quad (2.12)$$

Here, *Qin (iw)* and *Tin(iw)* is the flow and temperature of inflow, T2(i) is the temperature of the entrained flow. *QE(i)* is the entrained flow in the selected layer.

$$T2(IPL) = \frac{Tin(iw)*V(dc)+T2(IPL)*V(IPL)}{V(dc)+V(IPL)} \quad (2.13)$$

IPL is index of layer receiving the interflow. *V(dc)* is the volume of water in density current, *V(IPL)* is the volume of water in the receiving layer. *T2(IPL)* is the final temperature in the layer which is receiving inflow. The new concentration of each state variable in the layer is the volume weighted average of the initial concentration in the layer and the concentration in the inflow. A layer thickness check is also included with the inflow-outflow subroutine.

2.7 Results for Inflow-Outflow Submodel

Among the study lakes, only Lake Carlos, Pearl Lake and Riley Lake have inflow data. Lake Carlos has flow, water temperature and phosphorus input data from two inflow sources: Lake Darling and Lake Le Homme Dieu and one outflow: Long Prairie River. The inflow and outflow data were collected by USGS for a period of 3/25/2010 to 11/08/2010. As mentioned in section 2.6, inflow can be mixed as overflow, interflow or underflow. Figure 2-8 shows the impact of inflow on water temperature of Lake Carlos. Water temperature did not differ much in the surface layers when the inflow was added. The inflow was treated as interflow, and it got mixed with the lake water in the middle layers. So, the water temperature shows noticeable difference from April to October of 2010 as a result of inflow mixing. The addition of inflow

into the Lake Carlos model improved the model performance, reducing the RMSE from 1.66 ^{o}C to 1.46^{o}C.

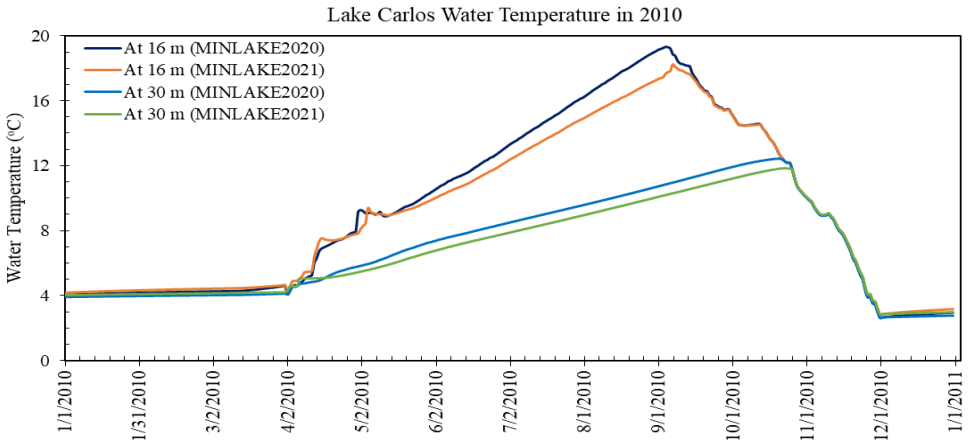

Figure 2-8 Lake Carlos water temperature at 16 m and 30 m from the surface using MINLAKE2020 (without inflow) and MINLAKE2021 (with inflow)

For Lake Elmo, Carrie and Thrush, a hypothetical scenario has been simulated. It was assumed that the lakes have three inflows and one outflow: inflows of 20, 40 and 60 cfs and outflow of 20 cfs. The inflow temperature was calculated as a function of air temperature(T_a)using equation ($T_w(t) = aT_a(t) + b$) (Chen & Fang, 2015).The inflow BOD and DO was set as 11 and 10 mg/L, respectively. For Lake Elmo, we assumed that all the inflows have a phosphorus concentration of 0.006 mg/L. Figure 2-9 shows the change in phosphorus concentration due to the inflow.

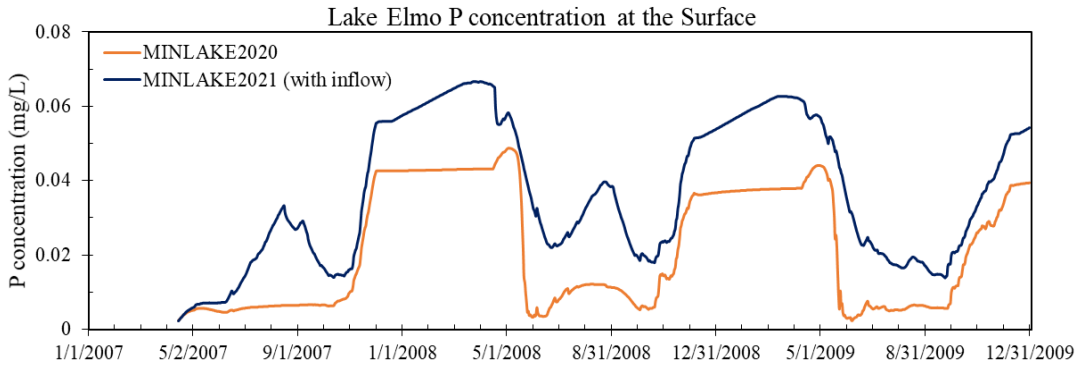

Figure 2-9 Lake Elmo simulated phosphorus concentration using MINLAKE2020 (without inflow) and MINLAKE2021 (with inflow)

2.8 Conclusion

A one-dimensional daily water quality model MINLAKE2020 was developed, incorporating phytoplankton, zooplankton, nutrient, and BOD simulation into the MINLAKE2012 model, which simulated daily temperature and DO. The inflow-outflow sub model was added into MINLAKE2020 and the updated version is MINLAKE2022. MINLAKE2020 and MINLAKE2022 were applied to six Minnesota lakes with varying characteristics in terms of depth (two shallow lakes, two medium-depth lakes, two deep lakes) and trophic status (two eutrophic, two mesotrophic, and two oligotrophic lakes). The simulated water temperature, DO, Chl*a*, and phosphorus time series and profiles were compared with available observed data in 15–36 days for two to four years. Simulation results from the MINLAKE2020 and MINLAKE2022 model provide the following conclusions:

1. MINLAKE2020 was calibrated against measured profiles in six Minnesota lakes (Table 2-2) for short term (2–4 years) with an average standard error of 1.51^{o}C for temperature and 2.33 mg/L for DO. The average standard error for DO simulation of these lakes decreased by 24.2%

from the original MINLAKE2012 model, which indicates better model performance. DO results reflect/integrate reasonably simulated phosphorus, Chl*a*, and BOD results at different layers (see Figures 2-3 to Figure 2-6).

2. The addition of phosphorus and Chl*a* simulation for MINLAKE2020 improved model performance in comparison to MINLAKE2012 where Chl*a* was specified input. It greatly affects the DO concentration in some lakes such as Pearl Lake (Figure 2-2). Thrush Lake and Carlos Lake also showed significant improvement in DO simulation with MINLAKE2020. The standard error decreased by 2.12 mg/L and 1.76 mg/L for Thrush and Carlos Lake, respectively.

3. The deep lake simulations exhibit a certain yearly trend for phosphorus and Chl*a*, whereas the shallow lakes might manifest a significant yearly change in phosphorus and Chl*a* concentration year by year due to two overturn periods (complete mixing) and the complex interactions/connections among phosphorus, Chl*a*, and DO (Figure 2-4 and 2-5), which are evident through governing equations and processes simulated.

4. DO concentration is the primary control of internal loading via anoxic release of phosphorus from the lake sediment. MINLAKE2020 was applied to Lake Elmo for a 20-year (1989 to 2009) continuous simulation with a single set of calibration parameters with regression coefficients of 0.99 and 0.94 for temperature and DO profiles, respectively. The simulation revealed an increasing trend of surface phosphorus from 1997 to 2009, agreeing well with the observed trend. This trend is directly related to sediment phosphorus release. The average yearly sediment phosphorus release increased from 151.8 kg in 1990–1996 to 244.1 kg in 1997–2009. This increase is caused by the average 25 days increase in the anoxic condition at the bottom depth (41 m).

5. Inflow has a significant effect on lake water temperature and water quality. Based on the density difference between the inflow water and lake water, inflow either get mixed into certain layers (Figure 2-8) or simply treated as overflow. The nutrient input entering through the inflow greatly affect the nutrient and Chl*a* concentration in the lake.

Chapter 3 One- and Three-Dimensional Hydrodynamic and Water Temperature Modeling Comparison

3.1 Introduction

Eutrophication and anoxia are unresolved issues in many freshwater systems. High water temperature and low DO concentrations in freshwater are a global concern (Stefanidis et al., 2022), and many aquatic ecosystems are suffering because of these conditions. Lack of oxygen can have negative effects on fish and other lake biota including reduced respiration rates, diminished reproductive activity, forced changes in habitat location, and ultimately reduced fish populations (Jiang & Fang, 2016; Jiang et al., 2017). As a result, water quality restoration is an important concern for many lake managers. Lake modeling is a useful tool to predict lake DO at a future time. Researchers are using lake models to simulate water temperature and DO in lakes to identify DO trends, leading to the development of numerous models. Over the past few decades, several 1-dimensional (1-D), 2-D and 3-D lake models have been developed and used to simulate hydrodynamics, temperature and water quality parameters in lakes and reservoirs (Cole & Wells, 2004; Hamrick, 1995; Tasnim et al., 2021).

1-D coupled hydrodynamic and water quality models (e.g., MINLAKE, DYRESM, and GLM) have been adopted to simulate thermal stratification dynamics and water-quality variables such as DO and nutrient concentrations with adequate accuracy in many water bodies (Andersen et al., 2022; Mesman et al., 2020). 1-D models are widely used (Imberger & Patterson, 1989; Tasnim et al., 2021) due to their low number of required input parameters and small computation time. Models with higher dimensionality (2-D and 3-D models) provide increased detail regarding hydrodynamic effects, spatially varying inflow, and transport mechanisms, such as density currents at river inflow locations. 3-D models provide the greatest hydrodynamic and

water-quality resolution but require larger computational effort for simulation time and output storage. Some researchers have successfully coupled the 3-D model ELCOM with the 1-D model CAEDYM to simulate nutrient and phytoplankton dynamics in lakes (Carraro et al., 2012; Romero et al., 2004). The 3-D model EFDC+ has been extensively used for hydrodynamics and water quality simulations because of its continuous development, computational accuracy, and flexibility (Chen et al., 2015; Devkota & Fang, 2015).

The main difference between coupled hydrodynamic/water quality models is the spatial dimensions considered in the model. Model selection depends on modeling goals, desired accuracy, and the location and characteristics of the waterbody. Sometimes, important information/process might be overlooked by one model. As a result, selecting the best model for a waterbody can be challenging. To aid in model selection, several studies have compared the performance of models having similar or differing spatial dimensions. For example, the Lake Model Intercomparison Project (Stepanenko et al., 2010) compared the performance of different 1-D models for a number of reference lakes (Stepanenko et al., 2013; Thiery et al., 2014). Mesman et al. (Mesman et al., 2020) compared the performance of three 1-D hydrodynamic models (Simstrat, GOTM, GLM) during storms and heatwaves. Yao et al. (Yao et al., 2014) compared four dynamic 1-D lake models for ice and temperature simulations in Harp Lake in Canada. The MINLAKE model performed well for the comparison studies where it was tested (Stepanenko et al., 2010; Yao et al., 2014). The selection of higher dimensionality does not always produce better simulation results (Wells, 2020). DeGasperi (DeGasperi, 2013) compared the performance of CE-QUAL-W2 (2-D) and CH3D-Z (3-D) in simulating the water temperature of Lake Sammamish in the USA. Both models produced similar results with slightly better performance statistics for the 2-D model. This might happen because of the higher sensitivity of

the 3-D model to certain parameters, and model output location and depth. Al-Zubaidi and Wells(Al-Zubaidi & Wells, 2018) evaluated the capabilities of CE-QUAL-W2, and a three-dimensional adaptation of the same software known as (CE-QUAL-W3) in modeling temperature stratification in Laurance Lake, Oregon, USA. The predictions of both models were in agreement with measurements, but to run the 3-D model was 60 times more expensive in terms of computational time. Ishikawa et al. (Ishikawa et al., 2021) compared hydrodynamic simulations of 1-D (GLM), 2-D (CE-QUAL-W2) and 3-D (Delft3D) models, concluding that higher dimensionality produced better results. Man et al. (Man et al., 2021) compared 1-D (GLM) and 3-D (Si3D) models for shallow reservoir water temperature and DO simulations. They recommended using the 1-D model for help with calibration but using 3-D model for simulating thermal stratification and management interventions.

Choosing a model based on dimensionality usually depends on the objectives of the study, the water body characteristics, and computational cost and time. A direct comparison of modeling results using 1-D and 3-D models may be helpful in identifying relative advantages and disadvantages of the two models in a quantitative manner. In numerical simulations, both temporal and spatial resolution are very important. Lower spatial resolution may fail to simulate hydrodynamic processes correctly or resolve bathymetry for waterbodies. The aim of this study is to quantify the relative advantages of 1-D and 3-D coupled hydrodynamic and water quality models and analyze ice cover and temperature dynamics simulated by the models. Ice cover, water temperature, and DO simulations are analyzed in three lakes in Minnesota: Pearl Lake (shallow); Trout Lake (medium depth), and Lake Carlos (deep) using the 1-D model MINLAKE, and the 3-D model EFDC+.

3.2 Methods

3.2.1. Models Used

For this study, the Minnesota Lake Water Quality Management Model (MINLAKE) (Riley & Stefan, 1988) was selected as the 1-D model because of its demonstrable efficiency and recent development. The MINLAKE model has been modified several times and has been successfully used for more than 30 years to simulate water quality parameters in different types of lakes. MINLAKE can reproduce selected constituent data to a relatively high accuracy (Batick, 2011). The latest version of MINLAKE, MINLAKE2020 (Tasnim et al., 2021b) is used for this study since the model is capable of simulating water temperature and other water quality parameters, as well as snow and ice cover during winter periods. MINLAKE2020 was used to simulate water quality in six Minnesota lakes of different characteristics in 2021 (Tasnim et al., 2021b) which is discussed in Chapter 2. The 3-D Environmental Fluid Dynamics Code (EFDC+) model was selected for its computational accuracy and ability to perform a variety of water quality computations. In the past decade, EFDC+ has been extensively used to predict algal blooms in lakes, rivers and reservoirs as well as in urban constructed ponds (Huang et al., 2017; Kim et al., 2017; Song et al., 2019; Wu & Xu, 2011; Zheng et al., 2021). For example, the lower section of Han River in South Korea experienced a severe algal bloom in 2015, and EFDC+ was used to understand algal dynamics in this system. Kim et al (2017) found that at least three algal groups need to be simulated to attain good Chla calibration accuracy for the study area. Zheng et al (2021) used EFDC+ combined with Long Short-Term Memory (LSTM) modeling (an artificial neural network modeling approach) to extend one-point data obtained by a single instrument to the entire 249 ha water area of their study domain on the BeiYun River in Beijing,

China, to predict harmful algal blooms (HABs). 3-D EFDC+ models have also been used for assessing the risk of hazardous materials (Huang et al., 2017), the effects of submerged aquatic vegetation in internal loading (Sun et al., 2022), fishway planning and construction (Song et al., 2019), eutrophication in urban ponds (Luo & Li, 2018), and other predictive scenarios.

3.2.2. Ice Modeling Algorithms in MINLAKE and EFDC+

The ice and snow algorithm in the MINLAKE model was originally developed by Gu and Stefan (Gu & Stefan, 1990), and revised and improved by Fang et al. (Fang et al., 1996). MINLAKE2020 uses a full heat budget equation to estimate surface cooling, quantifies the effect of forced convective (wind) mixing, and includes the latent heat removed by ice formation:

$$\rho_i \lambda_i \frac{d\delta_i}{dt} = \frac{T_m - T_a}{(\delta_i/k_i)+(\delta_s/k_s+(1/h_{sa})} + k_w(\frac{dT}{dz})_{z=0} \quad (3.1)$$

Here, ρ_i is the density of ice (kg/m^3), λ_i is latent heat of fusion of ice (kJ/kg), $d\delta_i$ is the change in ice thickness (m), h_{sa} is bulk heat-transfer coefficient (snow/air interface), δ_i and δ_s are ice thickness (m) and snow thickness (m), respectively. Thermal conductivity of ice and snow are represented by k_i and k_s, respectively (W/m/^{o}C), T_m is temperature at the bottom of ice layer (0 ^{o}C), T_a is air temperature (^{o}C), k_w turbulent conductive heat transfer coefficient (kcal/day ^{o}C m), and dT/dz is the water temperature gradient near the ice-water interface (^{o}C/m). The solar radiation penetrating the lake water below the ice is calculated by:

$$R_{iw} = R_s(1-\beta_s)(1-\alpha_s)(1-\beta_i)(1-\alpha_i)\exp(-\eta_s\delta_s)\exp(-\eta_i\delta_i) \quad (3.2)$$

R_{iw} is the solar radiation penetrating the lake water below the ice (Langley/day), R_s is the total incoming solar radiation flux reaching the snow surface in winter or water surface in summer (Langley/day), β_i and β_s are surface reflectivity (albedo) for snow and ice, respectively, α_i and α_s

are surface absorption coefficients for snow and ice, respectively, and η_i and η_s are attenuation coefficients(m^{-1}) in ice and snow, respectively.

This algorithm has a fine (0.02 m) spatial resolution near the water surface where water temperature gradients before freeze-over are the greatest. Predicted freeze-over dates were compared with observations in nine Minnesota lakes for multiple (1 to 36) years (Fang et al., 1996; Fang & Stefan, 1996b). The difference between the simulated and observed ice formation dates was less than 6 days for all lakes studied. Snow thickness is determined from snow accumulation (based on observations), followed by compaction, and melting of snow by surface heat input (convection, rainfall, solar radiation) and melting within the snow layer due to internal absorption of shortwave radiation, and transformation of wetted snow to the white ice when cracks in the ice cover allow water to spill onto the ice surface. In the model, ice growth occurs from the ice-water interface downward (black ice) and from the black ice surface upward (white ice). Ice decay occurs at the snow-ice interface, ice-water interface and within the ice layer. MINLAKE was used to predict snow- and ice-cover characteristics in small lakes (up to 10 km^2) in the contiguous US under past and future climate scenarios (Fang & Stefan, 1998; Fang & Stefan, 2009).

EFDC+ has the same ice sub-model as CE-QUAL-W2 (Cole & Wells, 2010). Ice formation and melt is simulated using a coupled heat approach. Ice forms when the surface water temperature lowers to the freezing point by normal heat exchange processes. With further heat removal, ice begins to form on the water surface and negative water temperature is converted to equivalent ice thickness. The ice model includes an ice cover with ice-to-air heat exchange, conduction through ice, conduction between underlying water and a melt temperature layer on the ice bottom. The overall heat balance for the water-to-ice-to-air system is:

$$\rho_i L_f \frac{\Delta h}{\Delta t} = h_{ai}(T_i - T_e) - h_{wi}(T_w - T_m) \quad (3.3)$$

ρ_i is the density of ice (kg/m^3), L_f is the latent heat of fusion of ice (J/kg), $\Delta h/\Delta t$ is the change in ice thickness (h) with time (t) (m/sec), h_{ai} and h_{wi} are the coefficients of ice-to-air heat exchange and water-to-ice heat exchange (through the melt layer) (W/m^2/^{o}C). T_i is the ice temperature, T_e is the equilibrium temperature of ice-to-air heat exchange, T_w is the water temperature below ice and T_m is the melt temperature. The solar radiation absorbed by water under the ice-cover is calculated by:

$$R_{iw} = R_s(1 - \alpha_i)(1 - \beta_i)\exp(-\eta_i \delta_i) \quad (3.4)$$

Here, R_{iw} is the solar radiation absorbed by water under ice cover (W/m^2), R_s is the incident solar radiation (W/m^2). The freezing temperature is set at 0^{o}C for freshwater, but for saltwater it is calculated as a function of total dissolved solids (TDS). Ice melting is calculated based on the net surface heat exchange. When net surface heat exchange is about to become positive, the ice begins to melt, and the energy stored internally is used to melt the ice. The ice sub-model used by CE-QUAL-W2 and EFDC+ does not simulate snow thickness above the ice. Though these models simulate solar radiation extinction for the ice cover period, they do not simulate the attenuation of solar radiation by snow. It is worth mentioning that snow has a much higher attenuation coefficient (20–40 m^{-1}) than ice so that a few centimeters of snow can completely attenuate all solar radiation.

3.2.3. DO Modeling Algorithm in MINLAKE and EFDC+

DO is one of the vital parameters of lake water quality simulation. Equation 3.5 and Equation 3.6 represent the governing equations for DO simulation by MINLAKE and EFDC+, respectively. Photosynthetic oxygen production and reaeration are source terms simulated in all

models. EFDC+ allows the user to choose the reaeration equation from five available options and three different equations for DO saturation calculation. Moreover, EFDC+ can include external DO load in the simulation. MINLAKE can simulate a maximum of 3 algal classes, but EFDC+ can simulate several algal groups (>3) specified by users. Though the models simulate the same processes, the representation of these processes are different in their formulation; detailed description can be found in the corresponding model documents.

MINLAKE:

$$Net\ change\ in\ DO = diffusion + algal\ photosynthesis - respiration - BOD - SOD - nitrification + reaeration - zooplankton\ respiration \quad (3.5)$$

EFDC+:

$$Net\ change\ of\ DO = algal\ photosynthesis - algal\ respiration - zooplankton\ respiration - nitrification - DOC\ decomposition - COD + Reaeration - SOD + external\ loads \quad (3.6)$$

3.2.4. Modeling Process

Three lakes in Minnesota were simulated using 1-D MINLAKE and 3-D EFDC+ models for this comparison study. The nearest weather station to the lake was selected for providing weather data: St. Cloud Regional Airport for Lake Carlos and Pearl Lake; Grand Marais Cook County Airport for Trout Lake. Bathymetry data for the lakes were downloaded from the Minnesota Department of Natural Resources (MN DNR) LakeFinder website (https://www.dnr.state.mn.us/lakefind/index.html). EFDC+ uses atmospheric pressure, dry bulb temperature, relative humidity, rainfall, evaporation, solar radiation, cloud cover, wind speed and wind direction as meteorological input. EFDC+ also has an algorithm to calculate solar radiation

and evaporation. For our study, we used solar radiation data (from the weather station) and EFDC+-simulated evaporation. Each lake was set up using a boundary polygon and dividing the surface area into uniform grids, incorporating bathymetry and boundary condition data. Lake inflow(s) and outflow(s) were added as flow boundaries, and time series of inflow/outflow, temperature, and water quality constituents were provided by USGS officials (Smith et al.,2014). EFDC+ simulates water temperature, organic carbon, organic phosphorus, organic nitrogen, ammonia nitrogen, nitrite nitrogen, silica and three algal classes (diatom, green algae, blue-green algae), and chemical oxygen demand (COD), in order to simulate DO (DSI, 2020). Setting up the 1-D MINLAKE model is much simpler than EFDC+. Bathymetry and inflow/outflow data with model parameters were fed into the model through an Excel spreadsheet user interface. Metrological data, including air and dew point temperature, solar radiation, cloud cover, wind speed, wind direction, precipitation and snowfall were saved as text files for each simulated year. The same inflow and outflow data were used in EFDC+ and MINLAKE modeling to have the same boundary conditions. The model was calibrated for each lake using continuous 15-minutes water temperature measurements collected by the USGS for the open water seasons (Smith et al., 2014) and DO profile data on monitoring days, downloaded from the MN DNR LakeFinder website.

The 3-D EFDC+ model gives users the opportunity to choose the coordinate system and the temperature model suitable for their particular waterbody from the available options. It has recently introduced Sigma-Zed (SGZ) coordinate system which has many advantages over the sigma coordinate system. EFDC+ also has three different water temperature models that are linked to meteorological data. Figure 3-1 shows example water temperature profiles for the stratification comparison in Trout Lake simulated using two coordinate systems against

measured profiles. From Figure 3-1, it is evident that SGZ layering results match well with the observed data whereas the standard sigma layering results show discrepancy with the observed temperature.

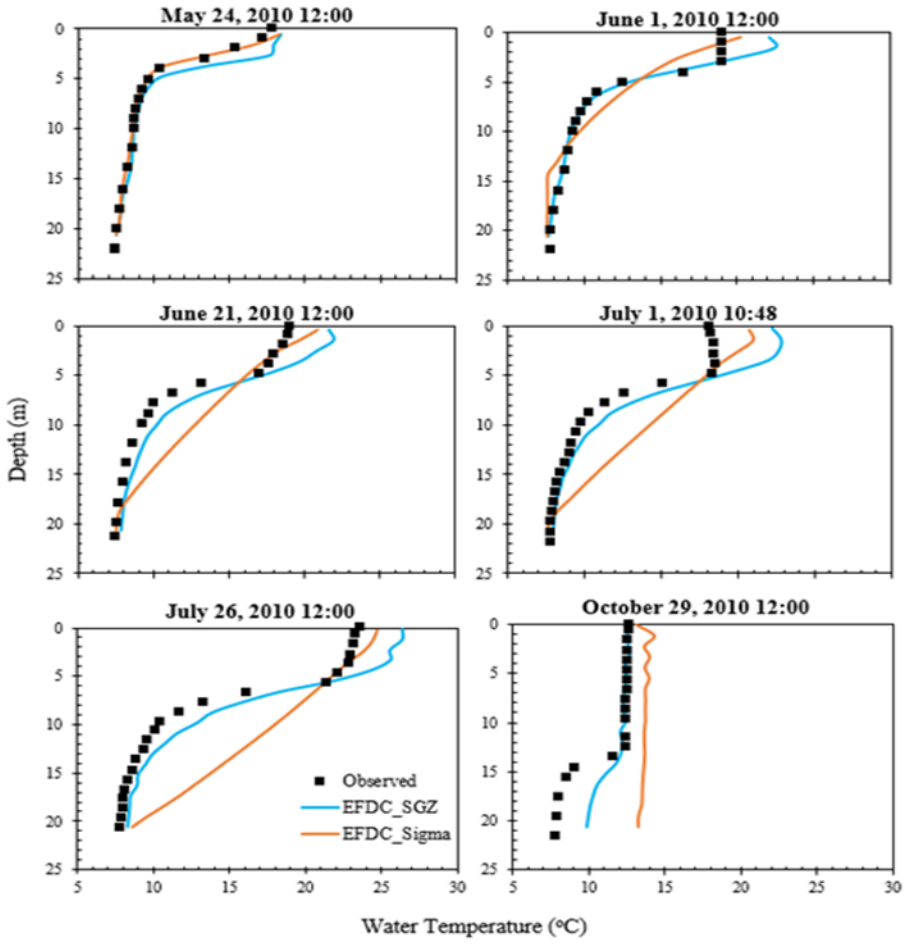

Figure 3-1 Water temperature profiles simulated using SGZ and standard Sigma coordinate compared with observed data in Trout Lake against with observed data.

Sigma coordinate models have issues handling sharp topographic changes from one grid to another. Because of its difficulty to handle horizontal density or pressure gradients (Craig et al., 2014), the standard sigma coordinate system cannot accurately represent stratified systems. The root mean square error (RMSE) for the sigma coordinate temperature is 2.6°C whereas it is

1.1^{o}C for the SGZ coordinate water temperature profiles on 5-25-2010 to 5-25-2011 in Trout Lake. Lake Carlos, being a deep and stratified lake, also had better stratification simulation using SGZ coordinate. However, for Pearl Lake, the simulated water temperature profiles showed no difference based on the layering option. The effect of coordinate system on stratification simulation correlated with lake's mixing scenario. Since the SGZ layering system calculates stratification based on the minimum active cell approach, the deep and stratified lakes show better results with the SGZ system.

EFDC+ has the option to simulate water temperature using three different model options that couple with meteorological data. During 2010–2011, Lake Carlos had continuous measured 15-minute water temperature data at 10 depths (1.65–37.5 m, 3–6 m interval) collected by USGS (Smith et al., 2014), which are total of 331,910 measurement points. These valuable measurements were used to compare simulated water temperatures by three model options: (1) full heat balance, (2) equilibrium temperature, and (3) full heat balance with variable extinction coefficient (Table 3-1). In full heat balance (legacy) option, the user needs to define the slow and fast attenuation coefficients. These coefficients do not depend on any other parameter and are constant throughout the simulation period. In full heat balance (variable extinction coefficient) option, the extinction coefficient is calculated at each time step using the user specified background (water) extinction coefficient and the simulated Chlorophyll-a (Chl*a*), TDS, particulate organic carbon, dissolved organic carbon and plant shoots. Table 3-1 lists RMSEs for water temperatures at all 10 depths. Water temperatures simulated by full heat balance with variable extinction coefficients approach has the minimum average RMSE among the three options, 1.16^{o}C. Based on the results, the SGZ coordinate system and 'Full heat balance with variable extinction coefficient' temperature model was used for this study.

Table 3-1 Root Mean Square Errors (RMSEs) of Simulated Water Temperature (^{o}C) by EFDC+ Different Temperature Model Options for Lake Carlos

Depth (m) *	1.65	4.65	7.65	10.65	13.65	16.65	19.65	25.65	31.65	37.65	Average
Full Heat Balance (Legacy)	1.61	1.43	1.7	3.25	2.3	1.78	1.58	1.36	0.74	0.88	1.67
Equilibrium Temperature	2.52	2.74	2.52	2.15	2.1	1.91	1.59	1.63	1.36	0.92	1.94
Full Heat Balance (Variable Extinction Coefficient)	1.23	1	1.27	1.94	1.11	0.88	0.94	1.22	1.2	0.84	1.16

Note: * - The measurement did not reach the maximum depth at 49 m.

3.3 Study Lakes

Three lakes with very different characteristics (Figure 3-2 and Table 3-2) were selected for this study. The geometry ratio ($GR = A_s^{0.25}/H_{max}$, A_s in $m^{2,}$ and H_{max} in m being the surface area and the maximum depth of the lake) is a characteristic parameter of a lake related to stratification (Stefan et al., 1996). The lower the geometry ratio, the stronger the lake stratification. Lake Carlos and Trout Lake are deep (H_{max} > 20 m) (Stefan & Fang, 1994), strongly stratified (GR < 2, Table 3-2), oligotrophic (mean Chl*a* < 4 µg/L, (NAS and NAE, 1973)) lakes, whereas Pearl Lake is a shallow eutrophic lake (mean Chl*a* > 10 µg/L, (NAS and NAE, 1973)) polymictic lake (GR > 7).

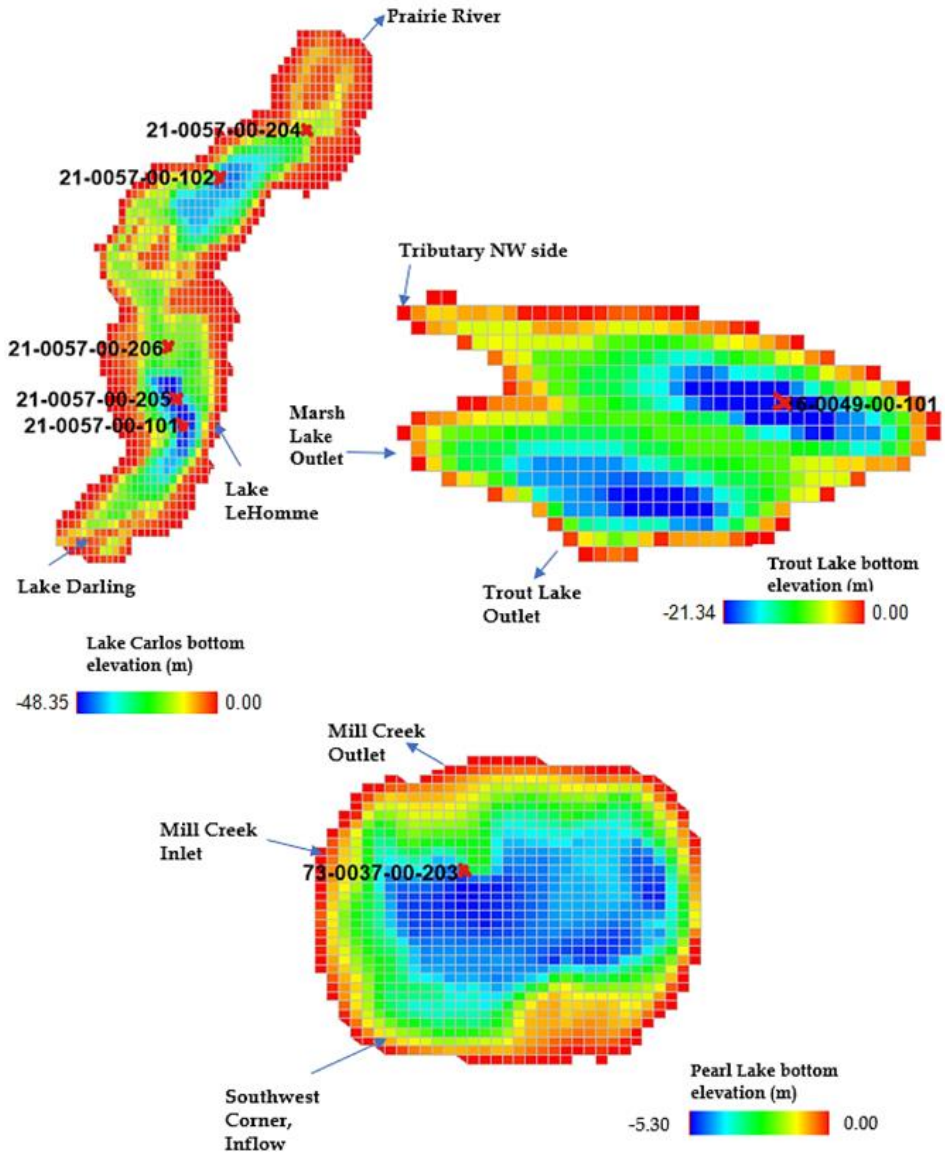

Figure 3-2 Bottom elevation (color contours, different scales for three lakes), inflow-outflow locations (blue arrows) and monitoring locations (red cross with station numbers) in Lake Carlos, Trout Lake, and Pearl Lake, Minnesota. The cell sizes and surface areas of the three lakes are in different scales for presenting the related information clearly.

Table 3-2 Characteristics of the Study Lakes along with Model Grid (EFDC+) and Layer (EFDC+ and MINLAKE) Information

Lake	Surface Area (km^2)	Max Depth (m)	Geometry Ratio $(m)^{0.5}$	Mean Chl*a* ug/L	Trophic Status	Simulation Years	MINLAKE Layers	EFDC+ DX (m)	EFDC+ DY (m)	EFDC+ Layers
Carlos	10.54	50	1.15	3.84	Oligotrophic	2010–2011	34	85	122	35
Trout	1	23.5	1.35	1.68	Oligotrophic	2010–2011	24	50	50	20
Pearl	3.05	5.6	7.53	16.91	Eutrophic	2014–2015	24	65	50	5

3.3.1. Lake Carlos

Lake Carlos is the terminal lake in the Alexandria Chain of Lakes, located in the North Central Hardwood Forests ecoregion in Douglas County, Minnesota. Primary inflow to Lake Carlos occurs in the southern part of the lake through two distinct channels out of Lakes Darling (USGS station number 05244780) and Le Homme Dieu (USGS station number 05244810). The headwater of the Long Prairie River (USGS station number 05244820) is the principal outflow channel for the lake. The lake has two extensive deep areas as shown in Figure 3-2. The Minnesota Pollution Control Agency (MPCA) has six data collection stations in Lake Carlos. Station 101 (maximum depth H_{max} = 49.12 m) and Station 102 (H_{max} = 41.67 m) are placed in relatively deeper areas whereas Station 204 is located in a shallower area (H_{max} = 23 m). 21-0057-00-101 (Station 101, Figure 3-2) and 21-0057-00-102 (Station 102) have profile data for several days in the summer.

3.3.2. Trout Lake

Trout Lake is located within the Lake Superior Basin, approximately 16 km north-east of Grand Marais in Cook County, Minnesota. Trout Lake is part of the Northern Lakes and Forests ecoregion and is occasionally differentiated as a Canadian Shield Lake. Trout Lake is located in

a bedrock basin and its geologic history is very different from Lake Carlos and Pearl Lake. Trout Lake is considered a dimictic lake, typically becoming stratified from May until October. Flow into Trout Lake is intermittent, making continuous discharge measurements difficult; therefore, periodic discharge measurements were completed at two small channels along the western margin of Trout Lake: (1) Trout Lake tributary, northwest side, near Covill, MN (USGS station number 04011140) and (2) Marsh Lake outlet (USGS station number 04011145). The Trout Lake outlet near Covill, MN is the principal outflow channel for the lake. Trout Lake is vulnerable to substantial changes in the surrounding forest since the forest acts as a buffer on wind-driven mixing. MPCA has six monitoring stations in Trout Lake but only one station was active in 2010–2011.

3.3.3 Pearl Lake

Pearl Lake is in the Sauk River Basin (part of the greater Mississippi River Basin) in Stearns County, MN. Pearl Lake is an intermittently stratified polymictic lake, having a slight decline in temperatures earlier in the year, but is generally well-mixed before early summer through late fall (Anderson et al., 2012). Pearl Lake has two inflow and one outflow locations: a) inflow at the southwest corner, near Marty, MN (USGS station 0520447), b) Mill Creek inlet (USGS station 05270448) inflow, and c) Mill Creek outlet (USGS station 05270449). Though five monitoring stations were placed in Pearl Lake, during our study period (2014–2015), only one station had profile data.

3.4. Result and Discussion

3.4.1. Water Temperature Simulation

For both the MINLAKE2020 and EFDC+ models, water temperature was calibrated first, followed by other water quality parameters. Water temperature simulation is very important

since all the water quality parameters depend on the water temperature. Although an hourly MINLAKE model, MINLAKE2018 is available for hourly water temperature and DO simulation, this model does not include Chl*a* and nutrients simulation. Therefore, the updated MINLAKE2020 model, which accounts for all physical and biological processes in the lake environment on a daily time step, was used. For EFDC+, a time step of 20 seconds was used for Lake Carlos and a time step of 10 seconds was used for Trout and Pearl lakes. However, the simulated results were extracted at an interval of 1 hour for EFDC+. Observed 15-minute water temperature data for Lake Carlos and Trout Lake were provided by USGS officials (Smith et al., 2014). For Lake Carlos, the water temperature time series was measured at a location close to station 21-0057-00-102 (Figure 3-2) and did not reach the maximum depth (48 m). The EFDC-simulated water temperatures were extracted at the deepest part. Trout Lake has observed water temperature data at 8 depths (0, 2,4, 6, 8, 12, 16, and 20 m) for the summer and early fall of 2010. Pearl Lake has 30-minute observed water temperature from the Sentinel Lake Program (MNDNR) at six depths (1.2, 1.7, 2.4, 3.4, 4.4, and 5 m). Lake Carlos water temperature data from the USGS was collected in two segments: 15 depths in summer 2010 (with maximum depth of 40.5 m) and 15 depths in fall 2010 and spring 2011 (with maximum depth of 37.5). For time series continuity, only 10 depths were used in this study.

MINLAKE gives one simulated profile each day over the maximum depth, which can be assumed to occur at the deepest location, while EFDC+ outputs one simulated profile each hour at each grid (different maximum depths at different grids) for the three study lakes. Simulated and measured water temperature profiles over time at the deepest location are used to construct contour plots to understand and compare water temperature dynamics and stratification characteristics. shows these contour plots of water temperature simulated by EFDC+ (3-D) and

MINLAKE (1-D) at Lake Carlos, Trout Lake and Pearl Lake including measured water temperature contours. EFDC+-simulated water temperature profiles were extracted at 21 depths, MINLAKE-simulated water temperature profiles were extracted at 34 depths for Lake Carlos, which was compared with water temperature measured at 10 depths. Lake Carlos is considered a dimictic lake, generally starting off well-mixed before summer, with a distinctive thermocline (stratification) that develops in the summer months, as clearly shown in Figures 3-3(a) and Figure 3-3(b), mixing again in the late fall, with inverse temperature stratification in winter. In Figure 3-3(a), MINLAKE2020 and EFDC+ simulated water temperatures have RMSE of 1.66 ^{o}C and 1.16^{o}C, respectively. At deeper depths (> 30 m), MINLAKE simulated gradual temperature increases, while EFDC+ simulated temperatures and observed data have very small increases (more or less horizontal contour lines before the fall mixing). Overall, EFDC+ simulates more detailed water temperature profiles compared to MINLAKE.

In Trout Lake, MINLAKE and EFDC+-simulated water temperatures were extracted at 14 depths and were compared with observed water temperatures at 11 depths (Figure 3-3(b)). Both EFDC+ and MINLAKE simulated water temperatures with RMSE of 1.5 ^{o}C. Both models slightly overestimate water temperature at the top layers during June–August. Compared with the observed water temperature, MINLAKE simulates lower water temperature in the bottom layers. Pearl Lake is a shallow lake having the maximum depth of only 5.5 m. MINLAKE and EFDC+-simulated water temperatures were extracted at 8 depths and were compared with observed water temperatures at 6 depths starting 1.2 m from the surface. In Figure 3-3(c), MINLAKE2020 and EFDC+ simulated water temperatures have RMSE of 1.79^{o}C and 1.30^{o}C, respectively. Detailed statistical parameters for water temperature and DO simulation are provided in Table 3-3.

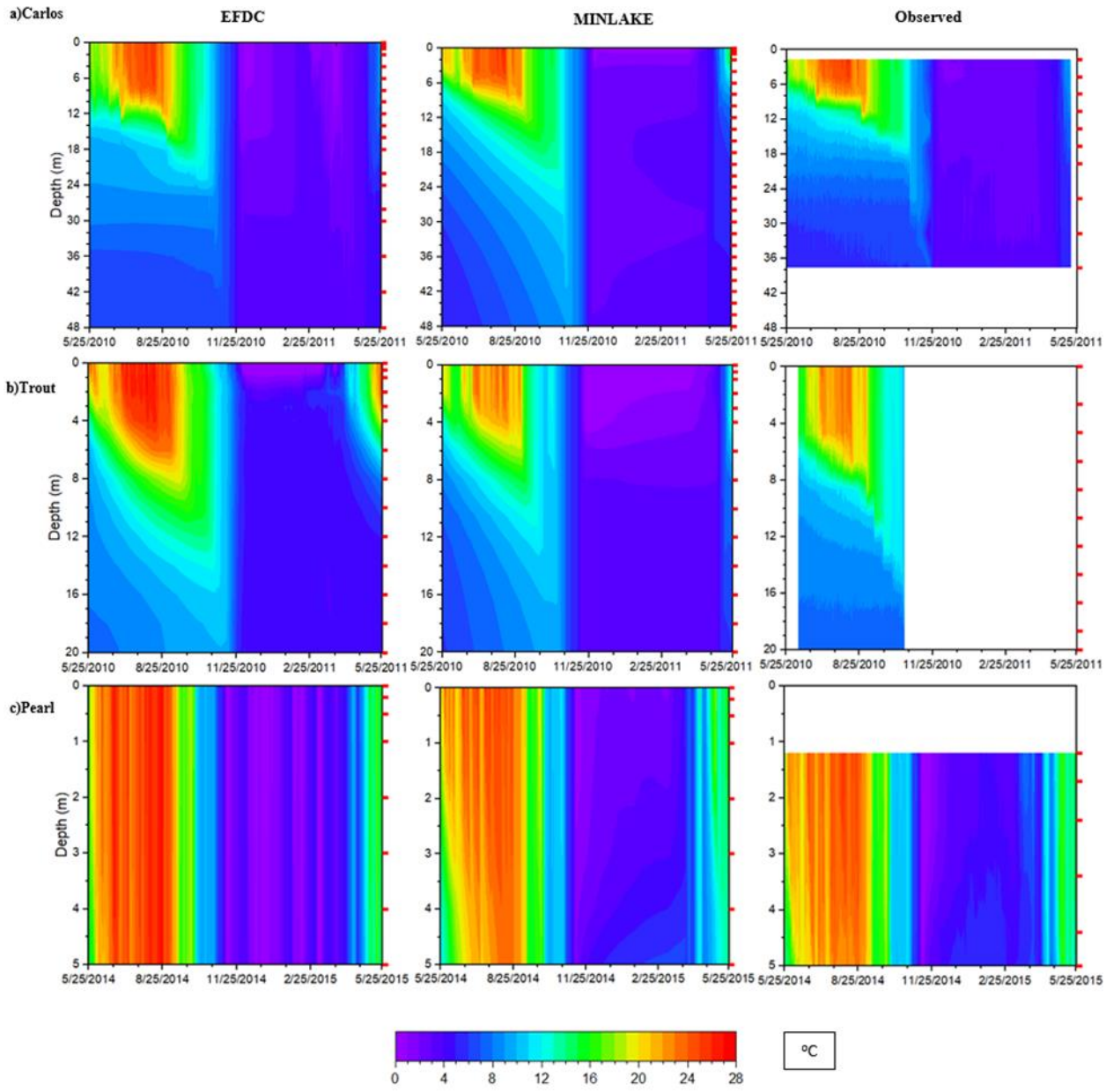

Figure 3-3 Contour plots of EFDC+ and MINLAKE-simulated water temperature (ºC) with observed water temperature (ºC) at different depths in a) Lake Carlos (2010–2011), b) Trout Lake (2010–2011) and c) Pearl Lake 2014–2015). The short red thick lines on the right end frame for each contour show depths where simulated or measured water temperatures were used to construct contours.

Table 3-3 Statistical Parameters for Study Lakes

	Lake Carlos (2010–2011)					
	Water Temperature			Dissolved Oxygen		
Model	RMSE [a] (°C)	NSE [b]	R^2 [c]	RMSE (mg/L)	NSE	R^2
MINLAKE	1.66	0.83	0.97	2.39	0.61	0.90
EFDC+	1.16	0.91	0.98	1.20	0.87	0.91
Model	**Trout Lake (2010–2011)**					
MINLAKE	1.50	0.98	0.99	1.45	0.70	0.92
EFDC+	1.50	0.50	0.98	2.12	0.55	0.91
Model	**Pearl Lake (2014–2015)**					
MINLAKE	1.79	0.98	0.99	3.42	0.70	0.92
EFDC+	1.30	0.50	0.98	1.12	0.55	0.91

Note: [a] – RMSE stands for Root Mean Square Error, [b] – NSE for Nash-Sutcliffe Efficiency (Nash & Sutcliffe, 1970), [c] – R^2 stands for regression coefficient of measured versus simulated

3.4.2. DO Simulation

Figure 3-4 shows the contour plots of simulated DO using EFDC+ (3-D) and MINLAKE (1-D) models at Lake Carlos, Trout Lake and Pearl Lakes, developed similarly to the temperature contours in Figure 3-3, except no observed DO contours are included, since continuous observed DO data were unavailable for any of the three lakes. In Figure 3-4, the right panel shows the comparison between observed and simulated DO near the surface and bottom of the lakes. MINLAKE simulated daily DO concentration, and hourly DO was extracted from EFDC+ results. In Figure 3-4(a), at Lake Carlos, both MINLAKE and EFDC+ simulated anoxic conditions at the lake bottom in summer 2010 and winter 2011, with EFDC+ simulating a shorter anoxic period compared to MINLAKE, followed by a gradual mixing of DO starting in April 2011. The EFDC+-simulated DO concentration during late fall of 2010 and late winter of 2011 is higher than that simulated by MINLAKE.

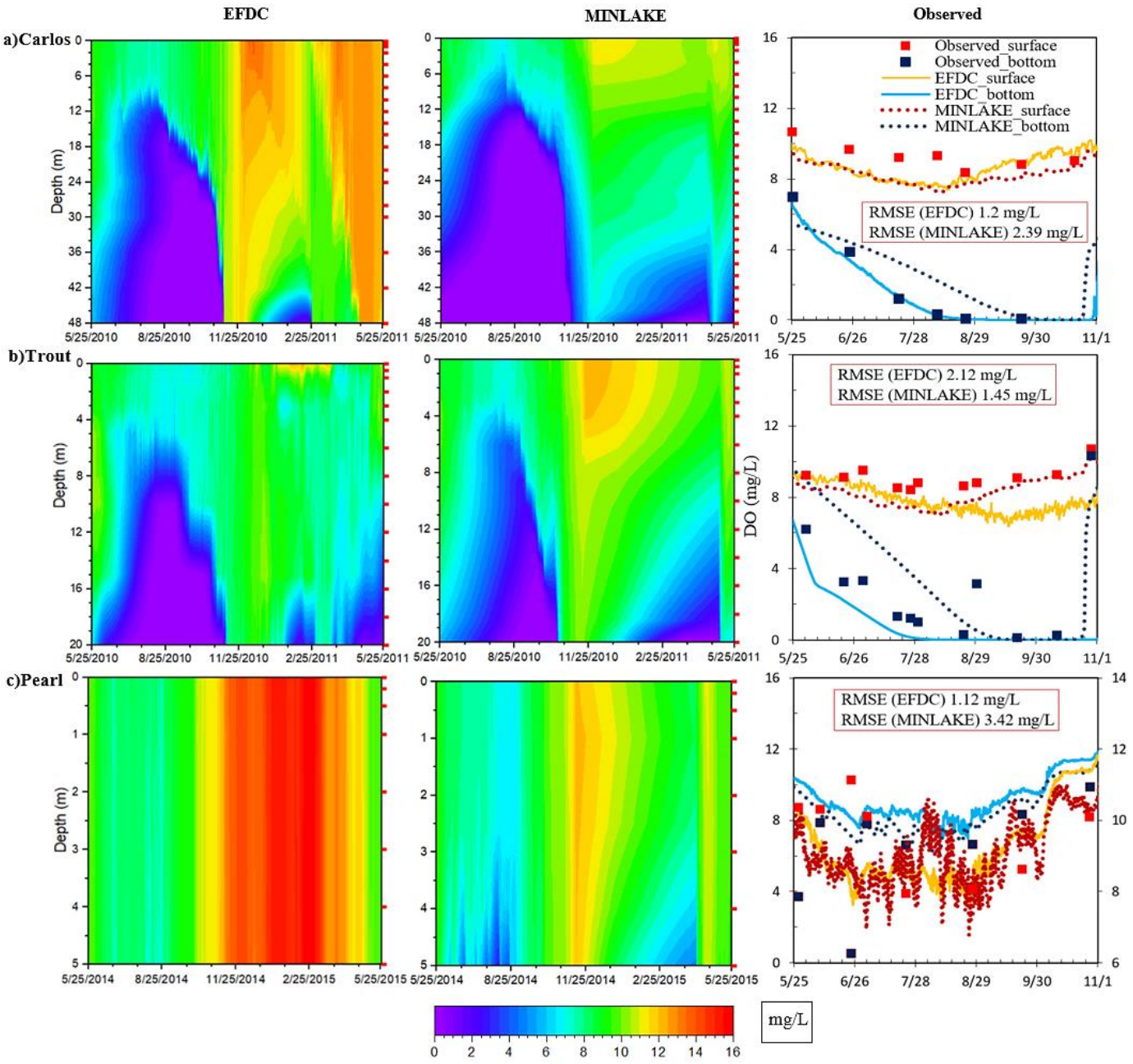

Figure 3-4 Contour plots of EFDC+ and MINLAKE simulated DO (mg/L) at different depths in a) Lake Carlos, b) Trout Lake and c) Pearl Lake. The short red thick lines on the right end frame for each contour show depths where simulated DO concentrations were used to construct contours. The right panel shows the observed and simulated DO near the surface (1 m) and bottom (40 m, 20m and 5 m for Lake Carlos, Trout Lake and Pearl Lake, respectively). The red

box in the right panel shows the RMSE of simulated DO for all depths at all stations where observed data were available (28/29 depths at Lake Carlos 101 station, 27/28 depths at Lake Carlos 102 station, 16/17 depths at Lake Carlos 204 station, 17 – 29 depths at Trout Lake, and 5 depths at Pearl Lake). This RMSE also includes one DO profile measured in the summer of the following year (which is not graphed here).

In Figure 3-4(b), at Lake Trout, MINLAKE simulated an anoxic period starting in March, and ice melts in the beginning of May. EFDC+ simulated two periods of anoxia: one in February and another one in late April. The difference in snow simulation mechanism causes this difference in DO concentration. The DO comparison was performed for the Summer of 2011. Trout Lake had snowfall until the beginning of May. As a result, snow simulation impacted the DO concentration and MINLAKE performed better than EFDC in Trout Lake DO simulation. Ice cover difference between the two models is explained in detail in Section 3.4.3. For Pearl Lake, MINLAKE simulated lower DO concentration in winter 2014.

Several DO profiles (8–10 profiles) were available for the summer and early fall on the LakeFinder website for each lake. The profiles were used to compare simulated results from EFDC+ and MINLAKE with observed data near the surface (1 m) and bottom of the lakes (Figure 3-4, right panel). Figure 3-4 (right panel) shows how the MINLAKE and EFDC+-simulated DO time series at two depths compare with the observed data. Based on the availability of observed DO profiles, DO concentrations were plotted near the surface and the bottom of all three lakes from May 25th to November 1st of the simulation year. For Lake Carlos, the observed DO at the top, and bottom layers match well with the simulated DO by EFDC+ (seven profiles on 5/25, 6/20, 6/24, 7/19, 8/24, 9/22, and 10/20). MINLAKE simulated anoxic conditions starting mid-September, whereas EFDC+ simulated it a month earlier, the

same as the observed data. In Trout Lake, with 11 measured profiles, EFDC+ simulates longer bottom anoxic conditions in the summer due to stratification compared to MINLAKE. The EFDC+-simulated bottom DO concentrations match well with the observed bottom DO. Overall, EFDC+ simulated surface and bottom DO with good agreement, while MINLAKE simulated higher DO in bottom layers during summer. Pearl Lake had 9 measured profiles in 2014–2015. Pearl Lake is a weakly stratified lake; it remains essentially well-mixed throughout the year. However, two observed data points had very low DO at the bottom, which does not agree with seasonal lake characteristics and could not be simulated through MINLAKE or EFDC+ simulations. This low bottom DO could be caused by short-term stratification which even occurs in some very shallow stormwater ponds, as noted in a recent study (Taguchi et al., 2020). Altogether, the simulated DO is in good agreement with the observed DO. At the end of October, the observed data matched well with the MINLAKE-simulated DO, whereas EFDC+ overestimates the DO concentration.

Lake stratification is an important physical characteristic of a lake that influences mixing, aquatic habitat, etc. If temperature or DO differences between the surface and bottom layers is more than $1^{o}C$ or 1 mg/L, the condition is typically defined as stratified. Figure 3-5 shows temperature and DO stratification simulated by EFDC+ and MINLAKE along with the observed stratification in the three study lakes.

Temperature stratification captured by EFDC+ and MINLAKE at Lake Carlos is very similar to the observed data. For DO, EFDC-simulated DO difference matches well with the observed differences. EFDC+ simulates complete mixing in early November due to fall overturn. Suddenly the hourly DO differences become negative for a very short period; the oxygenated top

layer DO go to the bottom due to overturn; the respiration and other biochemical processes might have consumed some additional DO from the top layer.

Figure 3-5(b) represents the simulated and observed stratification for Trout Lake. Both MINLAKE and EFDC+ models simulate slightly higher temperature stratification in the summer 2010 period where the observed data are available. EFDC-simulated DO stratification matches well with the observed stratification in summer, then EFDC+ simulates lower stratification in fall and a slightly later fall overturn. Though MINLAKE simulates slightly lower stratification in summer of 2010; in the fall, simulated stratification increases gradually and matches well with the observed stratification.

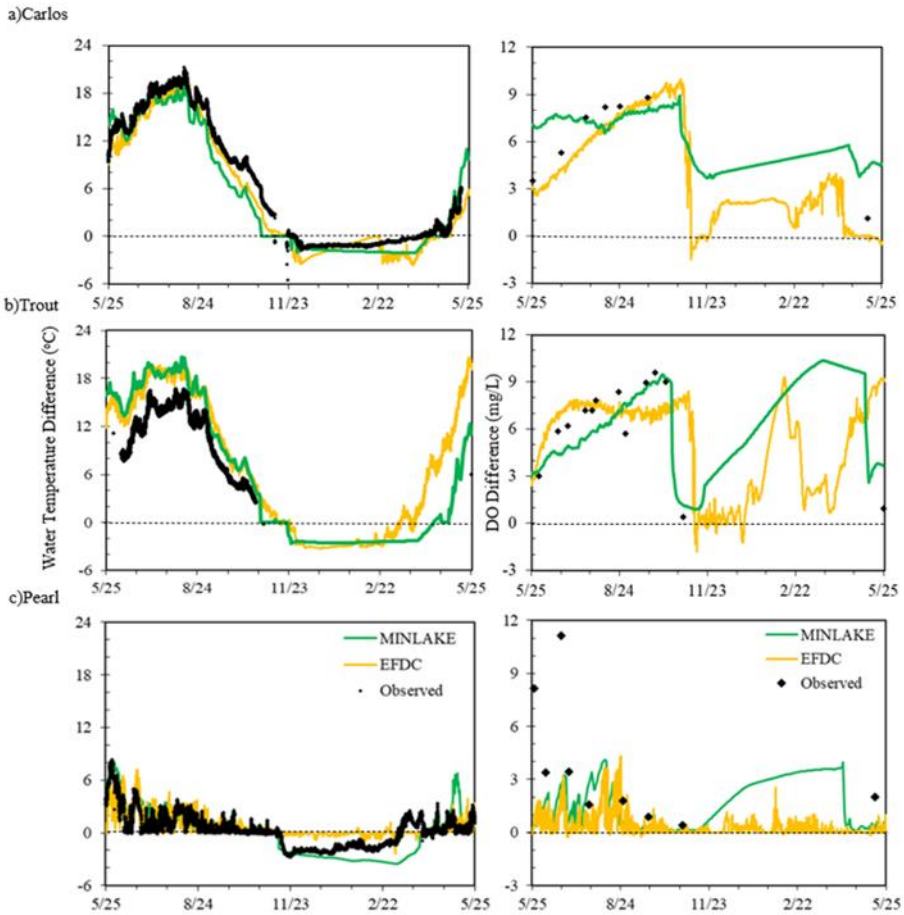

Figure 3-5 EFDC+ and MINLAKE-simulated water temperature and DO differences between the surface (1 m) and bottom layers for a) Lake Carlos, b) Trout Lake, and c) Pearl Lake compared with observed data.

EFDC+ simulates the overturn event later than that simulated by MINLAKE. The observed DO difference on 10/22/2010, being very close to the MINLAKE-simulated DO difference, confirms that MINLAKE simulates the overturn incident correctly. In Figure 3-5(c), for Pearl Lake, both EFDC+ and MINLAKE simulated temperature differences match well with the observed data during the summer; during the winter MINLAKE simulated still matches reasonably well with the observed data; neither MINLAKE could reasonably mimic the observed inverse water temperature stratification during the ice cover period, but EFDC+ could not (with negligible temperature difference). MINLAKE simulates higher DO stratification than EFDC+ does during the ice cover period but there are no data for comparison.

3.4.3. Ice Cover Simulation

MINLAKE uses snowfall as a meteorological input and predicts/estimates snow thickness above the ice. Both MINLAKE and EFDC+ simulate the growth and decay of ice thickness during the winter, but only MINLAKE incorporates/considers the impact of snow thickness on ice cover simulations. Figure 3-6(a) compares ice thicknesses simulated by EFDC+ and MINLAKE. Both models predict the same ice formation date (1/2/2011) on Lake Carlos, but EFDC+ simulates less ice thickness and a shorter ice cover period. EFDC+ simulates 3/14/2011 as the ice melting day, whereas MINLAKE simulates 4/10/2011 as the ice melting day. Correct estimation of ice-in and ice-out day will affect the availability of nutrients and the biological processes in the lake (Hampton et al., 2017). Since ice thickness data are not available for our study period in Lake Carlos, we used observed snow depth (m) data from the Saint Cloud

Regional Airport weather station (closest to Lake Carlos) as reference observation. However, there was a major snowfall event right after the ice melting simulated by EFDC+. The result is that EFDC+ underestimated ice thickness and the ice cover period, impacting DO simulations in the winter and spring periods. Similar results occurred for Lake Trout (Figure 3-6(b)) and Pearl Lake (Figure 3-6(c)).

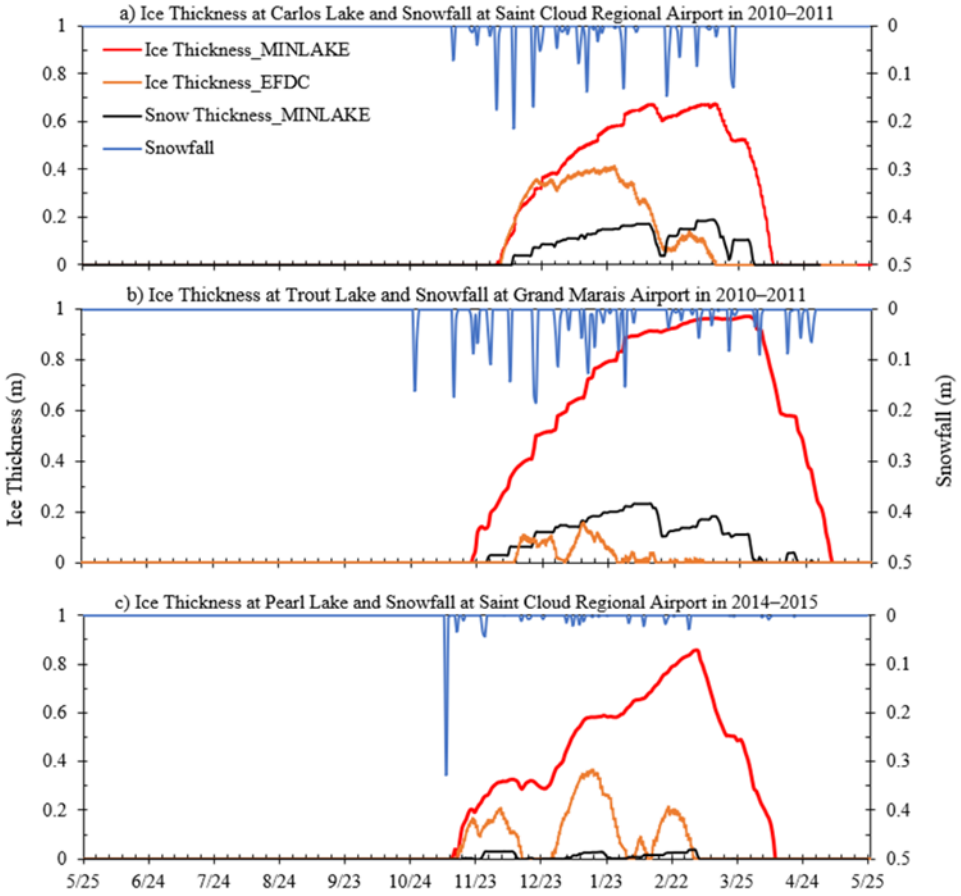

Figure 3-6 Simulated ice thickness (m) by EFDC+ and MINLAKE, snow thickness by MINLAKE, and observed snowfall at Lake Carlos (top panel), Trout Lake (Middle panel), and Pearl Lake (bottom panel).

A significant disparity in ice thickness existed for Trout Lake from the two models. The maximum ice thickness simulated in 2010–2011 was 0.97 m by MINLAKE and 0.15 m by EFDC+. Trout Lake is a very small lake having an area of only 1 km^2, situated in colder (northern) region, where snow accumulated above the lake ice could be thick and persist over a longer period than predicted by MINLAKE. These factors could explain the difference between model results, since EFDC+ does not simulate snow cover. Snow cover attenuation of solar radiation is much larger than the attenuation of ice and water (Fang & Stefan, 1996b); a thin layer of snow can attenuate most of the incoming solar radiation and promote ice growth. For Pearl Lake, EFDC+ simulates three periods of ice cover in the winter from 2014–2015, while MINLAKE predicts a continuous ice cover from 11/13/2014 to 4/11/2015. In that winter, Saint Cloud Regional Airport had 67% less snowfall compared to that of 2010.

The first few days after the snowfall were warmer, and EFDC+ predicted ice melting in some grids/areas which caused partial ice cover on the lakes. As a result, there were some gaps between ice cover periods, and solar radiation entered the lake through those openings and resulted in high phytoplankton abundance and well mixed conditions (Figure 3-4(c)). The results shown in Figure 3-4(c) were extracted from one simulation cell that is very close to the observation station. The different ice growth/decay rates in different cells were verified using the EFDC+ longitudinal view. MINLAKE, being a 1-D model, predicts growth/decay of ice cover over the whole lake surface and does not account for the spatial variability of ice growth/decay in different grids as in EFDC+.

Table 3-4 lists the simulated ice-in and ice-out dates predicted by MINLAKE and EFDC+, and the simulated snow cover periods predicted by MINLAKE for the study lakes. Overall, EFDC+ simulates shorter ice cover periods and smaller ice thickness. The MINLAKE

ice sub-model has been tested by several researchers. Fang and Stefan (Fang et al., 1996) tested the lake ice formation and melting day using the MINLAKE ice sub-model for 9 lakes in Minnesota for 9–36 years. This study showed that the observed ice melting days for the lakes were not more than 6 days before or after the simulated ice melting day. Yao et al. (Yao et al., 2014) compared four one-dimensional lake models: Hostetler, MINLAKE, SIM and General Lake Model for water temperature and winter ice cover simulation of Harp Lake (Ontario, Canada). MINLAKE generated the best agreement with observed ice-on and ice-off dates as well as ice thickness.

Table 3-4 Ice In and Ice Out Dates for the Study Lakes

	Ice In Day (MINLAKE)	Ice Out Day (MINLAKE)	Ice In Day (EFDC+)	Ice Out Day (EFDC+)	Snow Cover (MINLAKE)
Lake Carlos	12/3/2010	4/10/2011	12/5/2010	3/14/2011	12/11/2010–4/1/2011
Lake Trout	11/22/2010	5/6/2011	12/11/2010	2/17/2011	11/23/2010–4/4/2011 4/15/2011–4/22/2011
Pearl Lake	11/13/2014	4/11/2015	11/15/2014 12/29/2014 2/5/2015 2/13/2015	12/15/2014 2/1/2015 2/11/2015 3/4/2015	11/18/2014–11/22/2014 11/26/2014–12/13/2015 12/25/2015–3/7/2015 3/22/2015–3/24/2015

The effect of ice and snow thickness simulation can be explained using Figure 3-4. In Figure 3-4(a), for the DO simulated by EFDC+, the DO concentration begins to increase near the surface (due to surface reaeration) after ice melting on 03/15/2010 and then the lake mixing (spring overturn) results in high DO for all layers. EFDC+ does not simulate snow thickness and then solar radiation attenuation by snow (Equation 3.4). For MINLAKE simulated DO profiles, the DO concentration does not increase after March because of ice and snow cover. The lake has snow thickness until 4/2/2010, solar radiation is attenuated by snow and ice to prevent any significant oxygen production by photosynthesis. Snow attenuates most of the solar radiation since MINLAKE uses 40 m-1 and 1.6 m-1 as extinction coefficients for snow and ice,

respectively (equation 2, (Fang & Stefan, 1996b)). Under snow cover, oxygen productivity becomes very low because of little or no solar radiation reaching the water. In Figure 3-4(c), EFDC+ simulates high DO and well mixed conditions under ice cover since the lake had partial ice cover and the model assumed that phytoplankton growth and mixing both happened through the ice gaps. For lakes in cold regions, snow simulation holds considerable importance because of its influence on production and DO simulation.

3.4.4. Spatial Variance

The 1-D model MINLAKE cannot account for horizontal spatial variations of water quality constituents. Only 3-D models, such as EFDC+ can capture the spatial variability in all three directions. However, this difference is usually visible in large lakes (Rahaghi et al., 2019). Figure 3-7 shows the water temperature (top panel) and DO (bottom panel) profile comparison for two observation points 101 and 102 (Figure 3-2) in Lake Carlos.

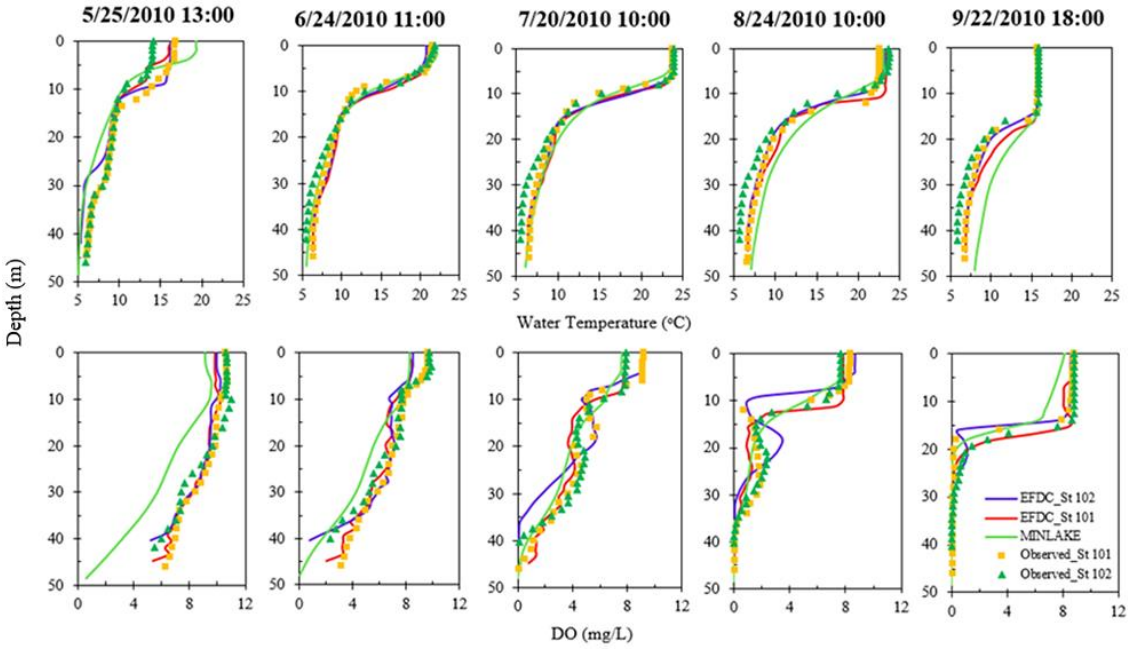

Figure 3-7 Simulated and observed water temperature (°C) and DO (mg/L) at two deep points in Lake Carlos.

The maximum difference in observed water temperatures between two locations at the same date and time is 2.3^{o}C, and the observed DO difference is 1.8 mg/L. It is evident that the water temperature at the surface layers were different on 5/25/2010 whereas water temperature varied in deeper layers from 6/22/2010 to 9/22/2010. The DO profiles also show some differences; surface DO is different in July and August. Overall, for June to August, the water temperature and DO differ in deeper layers. Two EFDC+ profiles simulated at the two grids that enclose monitoring points 101 and 102 match better with the observed data compared to one MINLAKE simulated profile for these five observation dates.

3.4.5. Effect of Inflow

Water flowing into a lake/reservoir can take different flow paths after entering the lake, depending on density stratification in the lake and inflow conditions. Inflows are classified as underflows (spreading along the reservoir bottom), interflows (spreading or entraining at an intermediate water depth) or overflow (spreading at reservoir surface). In 3-D models, inflow is discharged into a cell or several cells nearest the inflow location, whereas in 1-D models, the inflow eventually enters into the horizontal layer(s) where the inflow and ambient water have the same density. When several inflows enter into a large lake, spatial variance in temperature and other constituents may be observed.

Lake Carlos is a large, deep lake with inflow from two adjoining lakes, Lake Darling and Lake Le Homme Dieu (Figure 3-2). Observed inflow water temperatures from Lake Le Homme Dieu and Lake Darling are consistently slightly higher or very close to the surface water temperatures of Lake Carlos; therefore, the inflow regime for Lake Carlos is classified as overflow. When cooler water flows into the lake, the inflow water is entrained into the horizontal layers depending on inflow and lake water densities; this scenario is called interflow. To observe

an interflow condition or entrainment of inflow water in Lake Carlos, the inflow temperatures were reduced by 4ºC. Using the observed inflow-outflow rates and the hypothetical (reduced) inflow temperatures, MINLAKE and EFDC+ models were simulated again, and the spatial variance was compared (Figure 3-8(b)).

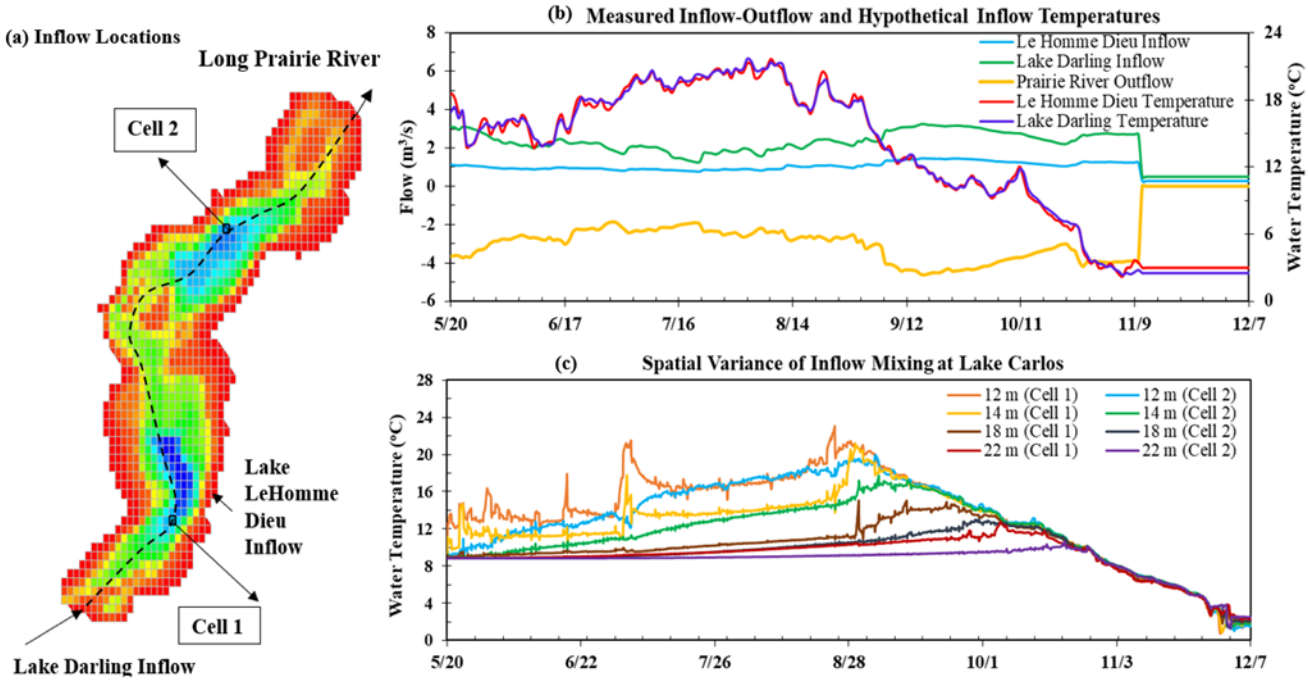

Figure 3-8 a) Location of inflow-outflow and the selected cells at Lake Carlos for temperature time series comparison; b) observed inflows, hypothetic outflow and inflow temperature time series for the scenario simulation, and c) EFDC-simulated water temperature time series at the selected cells (cell 1 and cell 2) at 12 m, 14 m, 18 m, and 22 m from lake surface in Lake Carlos.

The 1-D MINLAKE model simulated one vertical profile of temperature for the whole lake whereas the 3-D model simulated and calculated entrainment and vertical profiles for each grid. Based on proximity of the cell to the inflow location, mixing and entrainment vary location by location. Based on the MINLAKE-simulated water temperatures, the inflow was entrained more in the upper layers (0 m to 16 m) in the summer whereas it was entrained mostly in the

deeper layer (16 m to 48 m) in the fall. Figure 3-8(c) shows the differences in EFDC-simulated water temperature at four depths in two cells of same depth (~40 m): Cell 1 and Cell 2. Cell 1 is downstream of Lake Darling inflow but upstream of Lake Le Homme Diu inflow; therefore, the temperature profile at Cell 1 is mainly affected by the inflow from Lake Darling. Since Cell 2 is downstream of both inflows, its temperature profile is affected by both inflows. The maximum difference in water temperature between Cell 1 and Cell 2 is 9^{o}C at 12 m depth from the surface and occurred in early July. At 14 m, 18 m and 22 m depths, the maximum water temperature difference was 6.98^{o}C, 4.35^{o}C and 3.35^{o}C, respectively.

Cell 1 is mostly impacted by Lake Darling inflow. At 12 m and 14 m, the peaks observed on 5/30/2010 – 6/1/2010, 6/19/2010, and 7/1/2010–7/8/2010 resulted from increased mixing of the lake water aided by higher wind speed; the water temperature at 12 m is close to the water temperature near the lake surface on these days. The water temperature increased on 8/24/2010–9/6/2010 due to the higher air temperature on those days. In Cell 2, a drop in water temperature occurred at 12 m on 7/5/2010, caused by the low inflow temperature from both inflows. At 18 m and 22 m, there are lower water temperatures at Cell 2 compared to Cell 1. Cell 2 is impacted by both inflows; this cell represents the full effect of Lake Le Homme Dieu which has lower inflow temperature compared to Lake Darling.

Figure 3-9 shows the spatial variations of simulated water temperature (EFDC+, the MINLAKE-simulated profile is shown in the box at the right-bottom of each panel) on three days through a cross-section cut through the center of the lake from Lake Darling inflow to Long Prairie River outflow (as shown in Figure 3-8(a), black dashed path line). The cross-sectional view also shows two deep parts of the lake, the first near the Lake Darling inflow and the second near the Long Prairie River outflow.

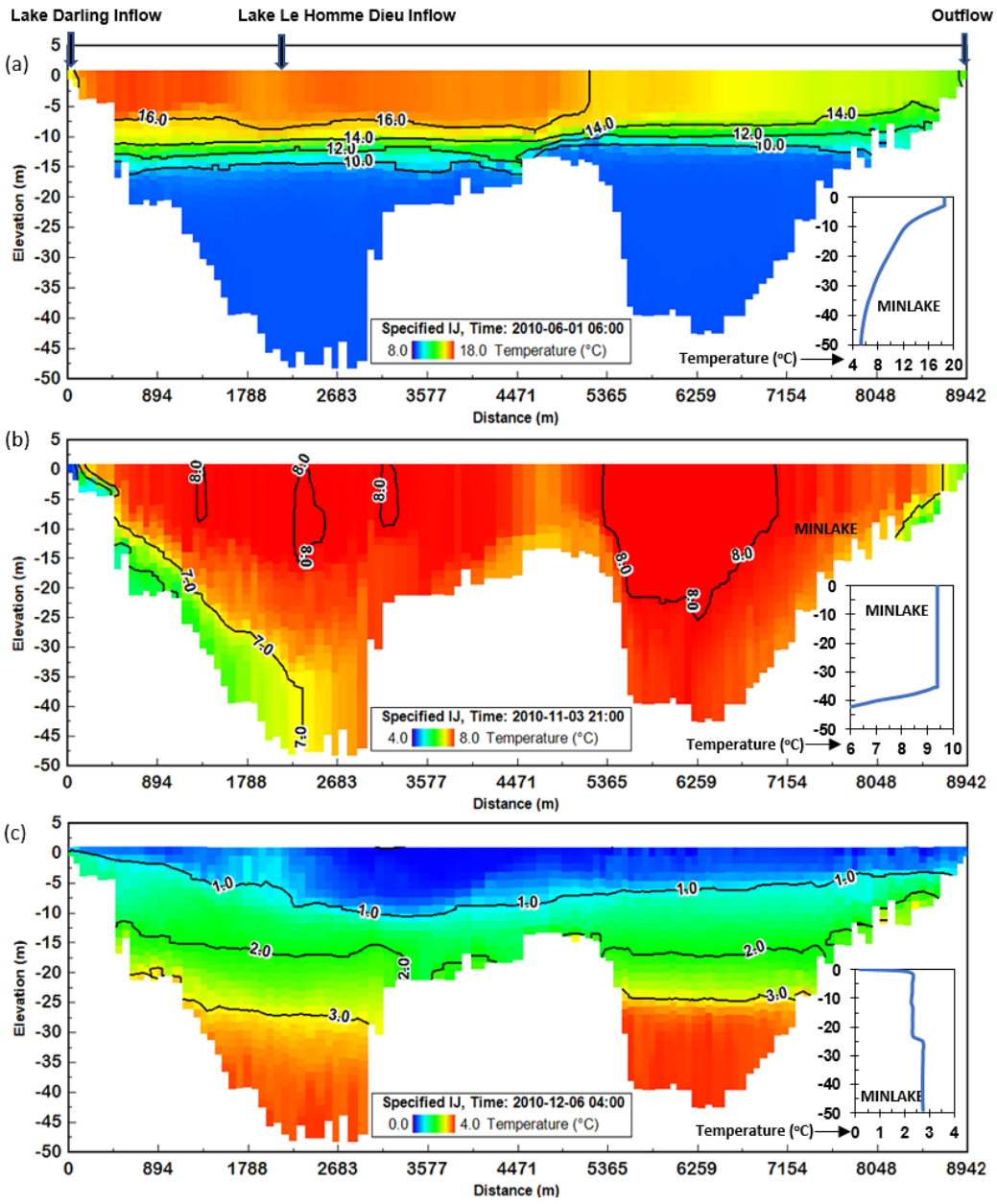

Figure 3-9 Longitudinal sections from Lake Darling to Long Prairie River through the centerline of Lake Carlos showing contours of EFDC+-simulated water temperature over depth at: a) 6:00 on 06/01/2010 b) 21:00 on 11/03/2010 c) 4:00 on 12/06/2010. Temperature color scales are different for these three days. The profile plots on the right-bottom of the panels show MINLAKE-simulated water temperature (oC) profiles on the same days for comparison.

Figure 3-9(a) shows spatial difference of water temperature during a summer day (6/1/2010). The inflow temperature was 16.03ºC at the Lake Darling inflow (2.42 m^3/s) and 15.98ºC at the Lake Le Homme Dieu inflow (0.97 m^3/s), with an outflow of 1.28 m^3/s. The surface water temperature ranges from 17.4ºC to 14.83ºC and at 12 m, the water temperature ranges from 13.65 to 9.1ºC (near the second deep part). MINLAKE simulated water temperatures of 18.5ºC near the surface and it then gradually reduced to 4.8ºC near the lake bottom. Though Figure 3-9(a) shows similar temperature stratification throughout the lake, the second deep part has lower surface water temperature which could happen due to the mixing of cold water from Lake Le Homme Dieu.

Figure 3-9(b) shows the density current flowing towards the deep layers of the lake; a clear distinction of cooler inflow water is observed on the first deeper area. The inflow temperature was 3.14ºC at the Lake Darling inflow (2.75 m^3/s) and 3.36ºC at the Lake Le Homme Dieu inflow (1.29 m^3/s), with an outflow of 2 m^3/s. The upper layers are well mixed and have a temperature close to 8ºC; the temperature drops to 7ºC at the lake bottom showing an example of underflow. MINLAKE simulated a well-mixed water temperature of 10.93ºC with a slightly lower temperature from 40 m below the surface.

Figure 3-9(c) shows the spatial difference of temperature during an ice cover period. Based on the ice thickness results from EFDC+, the ice starts melting on 12/4/2010 in areas close to Lake Darling. On 12/6/2010, the lake has ice cover only on the second deep part, limiting algae growth in that area. In response to Lake Darling inflow (0.3 m^3/s) of 3ºC and Lake Le Homme Dieu inflow (0.5 m^3/s) of 2.5ºC, the lighter inflow of water goes over the surface; this phenomenon is known as overflow. We can identify an increase in surface water temperature just upstream and downstream of Lake Le Homme Dieu inflow as a result of inflow from Lake

Darling and Lake Le Homme Dieu. The water temperature shows stratification opposite to Figure 3-9(a), cooler water on top and warmer water towards the bottom of the lake when temperatures are less than 4^{o}C. At the surface, the water temperature ranged from 0.029^{o}C to 0.85^{o}C. At 5 m depth, the temperature ranged from 0.13^{o}C to 1.5^{o}C. MINLAKE simulated near-zero water temperature at the top layer and ranged from 1.2 to 2.74^{o}C at the bottom layer. Since Lake Carlos is a large lake, the ice thickness varies over the longitudinal distance. Ice formation starts on 11/23/2010 near the outflow and gradually covers the whole lake by 12/8/2010. On 12/4/2010, the lake has ice cover on most of the cells along the centerline (Figure 3-8(a)) except some cells upstream and downstream of the Lake Le Homme Dieu inflow location.

3.4.6. Long-term Simulation Using MINLAKE

For the three study lakes, the 3-D EFDC+ model requires more time to simulate water temperature and water quality constituents compared to the 1-D MINLAKE2020 model. Although this study focused primarily on water temperature and DO, the EFDC+ eutrophication model also simulates algae (green algae, blue-green algae, diatom), nitrogen, phosphorus, organic carbon, and silica for model accuracy before DO can be simulated. For EFDC+, the time required to simulate water temperature and selected water quality constituents for this study ranged from 2.0 hours (for Pearl Lake) to 7.3 hours (for Lake Carlos) for a 13-month simulation period (1month warm-up period). Generally, simulation time depends on the number of computation grids and vertical layers. For Lake Carlos, 7.3 hours were required for 1127 horizontal cells and a maximum of 35 vertical layers. MINLAKE simulation over the same time period was significantly faster than EFDC+, taking only a few seconds. However, as noted previously, the EFDC+ model provides much more detailed temporal and spatial simulation results.

Figure 3-10 shows MINLAKE 10-year simulation results for Lake Carlos near the surface (1 m) and bottom (48 m) for past (using historical weather data) and future (CCCma CGCM3.1 A1B Scenario) climate conditions. The CGCM3.1 (Kim et al., 2002) is the third generation coupled General Circulation Model from the Canadian Centre for Climate Modeling and Analysis (CCCma). The maximum water temperature stratification is observed in September and October of each year. The lake shows maximum stratification in 2001. MINLAKE has been used for long-term simulation in several studies (Jiang et al., 2012). Tasnim et al. (Tasnim et al., 2021b) simulated Lake Elmo (a deep lake in Minnesota) for 20 years (1989–2009) with a regression coefficient (between simulated and observed) of 0.91 and 0.79 for water temperature and DO, respectively, using MINLAKE2020. This study also revealed that MINLAKE could mimic the increasing trend of phosphorus in 1997–2009. Moreover, MINLAKE can also simulate water quality using three future climate scenarios which are embedded in the model. Monthly air temperature increases projected by CGCM3.1 A1B scenario ranges from 2.91 to 4.84 ^{o}C near the St. Cloud weather station. As a deep oligotrophic lake, Lake Carlos had 24 days of anoxia for past climate conditions and is projected to have 78 days of anoxia for future climate conditions for the 10-year simulation period. Hypoxia (<1 mg/L DO) near lake bottom is simulated for 729 and 779 days for past and future climate conditions, respectively.

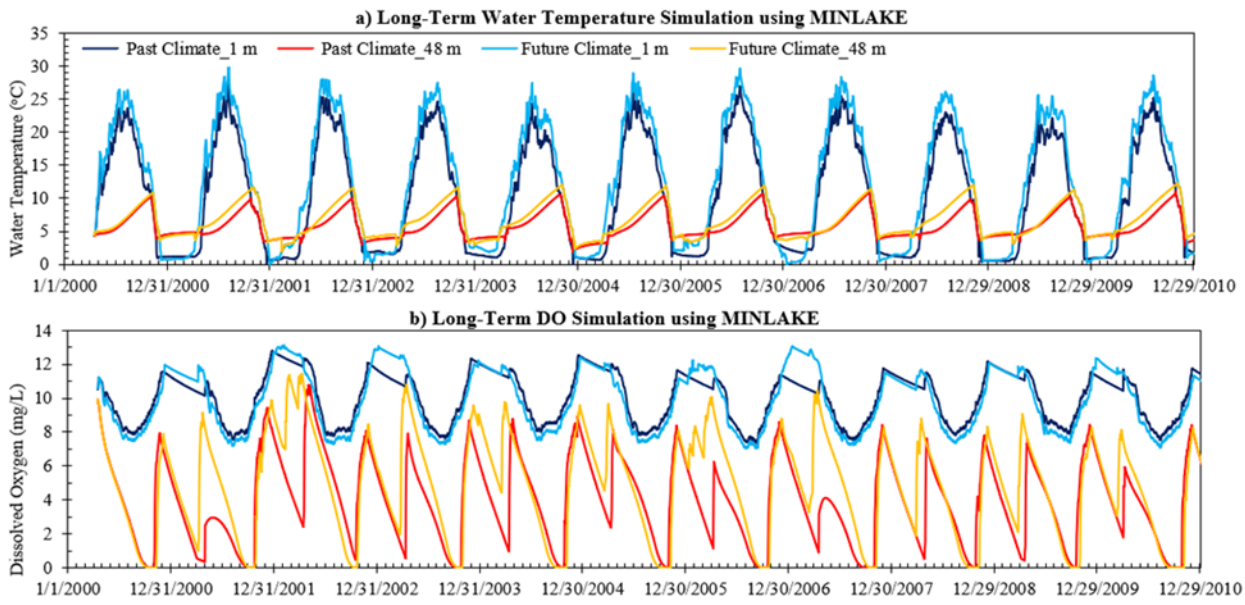

Figure 3-10 Time series plots (4/16/2000 – 12/31/2010) of simulated a) water temperature and b) DO at 1 m and 48 m depths from the surface under past and future climate conditions (CCCma CGCM3.1 A1B Scenario) for Lake Carlos (maximum depth 50 m).

EFDC+ would take considerable computational time to simulate over multiple years. As a result, EFDC+ is not recommended for long-term simulation targeting lake management decision-making. 1-D MINLAKE can simulate water quality with sufficient accuracy while taking much less computational time, which is an advantage when conducting long-term and scenario studies for lake management practices. However, if a detailed understanding of lake processes is required over shorter time intervals, then the 3-D EFDC+ model is a more appropriate simulation tool.

3.5. Conclusions

The 1-D model MINLAKE2020 and the 3-D model EFDC+ were used to simulate water temperature and DO at Lake Carlos, Trout Lake and Pearl Lake in Minnesota, USA. Inflow/outflow data and meteorological data were required by the models.

1. For Lake Carlos and Pearl Lake, the 3-D EFDC+ model performed better for temperature and DO simulations. EFDC+ DO simulation results were much better than MINLAKE (Figure 3-4), though the statistical results only represent the summer period. The RMSE for DO simulation for Lake Carlos and Pearl Lake is 1.20 mg/L and 1.12 mg/L, respectively. MINLAKE performed better than EFDC+ for Trout Lake, as a consequence of better ice cover simulation.

2. EFDC+ does not simulate snow thickness in cold region lakes. EFDC+ simulated shorter ice cover periods and smaller ice thicknesses in all three lakes. The early melting of ice predicted by EFDC+ can result in erroneous result for DO by simulating more mixing and overturns in the winter and spring.

3. EFDC+ considers spatial variance and performed well for both observation stations in Lake Carlos. The maximum difference in water temperature between two stations on the same date in Lake Carlos is 2.3ºC and the DO difference is 1.8 mg/L. This spatial variance is particularly important for very large lakes with complex bathymetry, or lakes having multiple inlets/outlets.

4. EFDC+ can extract detailed hydrodynamics and water temperature/quality variables. Inflow and outflow can be important in lake hydrodynamics. Inflow locations can influence the spatial variance of different constituents (Figure 3-8). In the case of a large lake receiving a significant amount of inflow, ice thickness, water temperature, velocity magnitude, flow etc. vary at different locations. The magnitude of differences depends on the distance of the comparing points, and the difference between the inflow temperature and lake water temperature.

5. MINLAKE requires considerably less computational time than EFDC+ to simulate lake water quality parameters over many years under the past and future climate scenarios, while providing useful information for long-term lake management decision-making.

Chapter 4 Three-Dimensional Hydrodynamics and Water Quality Model Development for the Cotton Bayou/Terry Cove System

4.1 Background

Estuaries are among the most productive ecosystems in nature. The mixing of fresh water and saline water in estuaries is predominantly responsible for this productivity (Bales et al., 2006). The transport of dissolved substances and suspended particles takes place during the interaction of riverine and marine systems. Phytoplankton growth and variations of nutrients in lakes or estuaries are connected with inflow from rivers and tributaries (Shen & Haas, 2004).HABs found in coastal waters are caused by lack of flow circulation, river inflows, and anthropogenic nutrient loading leading to eutrophication (S. Bricker et al., 2007). The dynamic forcings (inflow, tides, wind speed, and weather conditions) in the system result in the spatial and temporal variability of salinity, temperature, and nutrients in the estuary.

Tourism serves an important role in economic development, especially for coastal communities distant from local economic centers. One significant benefit of tourism is that it can quickly increase the local household average income because the primary recreational providers are micro-operators such as restaurants, short-term lodging rentals, equipment rental, and so on. However, it can also bring challenges if it is the primary revenue for local communities.

The Cotton Bayou/Terry Cove (CBTC) system (Figure 4-1) is in the heart of Orange Beach, AL and is a component of the larger Perdido Bay watershed which is connected to the Gulf of Mexico by Perdido Pass. The canals and other shallow waters of the CBTC system have historically served as nursery habitat for aquatic and avian wildlife.

Figure 4-1 Location of study area in Perdidod Bay-Wolf Bay system.

Over time, development and re-development have replaced much of the natural shoreline with seawalls and other structures, and sediment has accumulated in ways that disrupt natural hydrodynamic mixing. These and other unknown factors are contributing to water and sediment

quality degradation; fluctuating temperature, salinity, and dissolved oxygen concentrations; driving algal blooms, fish kills, and other indicators of poor ecological health. Eutrophication can greatly deplete DO in rivers and estuaries, negatively impacting aquatic organisms. Fish kills are a phenomenon referring to a localized die-off of fish populations. It is primarily caused by reduced oxygen in the water, which is the combined result of a variety of causes including algae blooms, increased water temperature, and the presence of toxic chemicals and pollutants. Unexpected fish kill events have the potential to negatively impact local tourism.

Perdido Bay has been of interest to many researchers due to its sensitivity to water quality degradation (Li, 2019; Robert J. Livingston, 2001). Eutrophication processes in the Perdido Bay system have been extensively studied through an 11-year study period (1988 to 1999) primary through monthly field data collection at a large number of locations in the bay and inflow rivers/creeks. These studies documented 26 algae/phytoplankton blooms from 1994 to 1999 (R.J. Livingston, 2001; Livingston, 2003) which occurred at a variety of times over a given year. Improvements in eutrophic conditions can be achieved by management, research, and monitoring programs working together (S. B. Bricker et al., 2007). The studies conducted by Livingston documented what happened over the 11-year study period and identified possible causes and some nutrient sources for algal blooms. However, there are no decision support or warning systems for management agencies to target nutrient reductions and project timing of occurrence of algal blooms in Perdido Bay.

Algal blooms consume DO and can lead to hypoxia (DO < 2 mg/L, https://oceanservice.noaa.gov/ hazards/hypoxia/) and anoxic conditions at various locations within Perdido Bay (Figure 4-1). Algal blooms are related to the type and quality of water entering the bay: streamflow, tidal inflow, urban stormwater runoff, and groundwater input;

nutrients from point and non-point sources; water temperature, and salinity stratification (Harris et al. 2015, Kim et al. 2012). Algal blooms can occur when conditions of nutrients, light, and temperature are optimum for the growth of phytoplankton (algae). *Gulf Menhaden* (*Brevoortia patronus*) is an important commercial fish species found in the Gulf of Mexico estuaries and marine waters, and is the primary species in many documented fish kills in Cotton Bayou (Figure 4-1) (Li, 2019; VenderKooy & Smith, 2015) For example, widespread fish kills of *Gulf Menhaden* were reported beginning on 7/31/2015 in the Cotton Bayou and Terry Cove areas of Perdido Bay (Figure 4-1). The lifecycle of *Gulf Menhaden* can be categorized into four stages (larvae, post larvae, juveniles, and adults) based on age and fork length (measured from the tip of the snout to the end of the middle caudal fin rays) of the fish. *Gulf Menhaden* health is sensitive to water quality conditions, especially water temperature and DO concentrations. A 1983 U.S. Fish and Wildlife Service (USF&W) report summarizing the environmental requirements for *Gulf Menhaden* ((Lassuy, 1983). In estuaries, juvenile *Gulf Menhaden* have been captured over a salinity range of 0 to 35 ppt and a temperature range of 5 to 35 °C (Benson 1982; Christmas and Waller 1973). Lassuy (1983) reported that water temperature less than 30° is ideal for *Gulf Menhaden* health, although definitive data on the optimum temperature (upper and lower lethal limits) are lacking (Lassuy 1983). A 1982 USF&W reported juveniles of *Gulf Menhaden* commonly occurred in waters with salinity ranging from 9 to 67 ppt ((Christmas et al., 1982). *Gulf Menhaden* are among the species negatively impacted by low DO in estuaries (Christmas and Waller 1973; Etzold and Christmas 1979). Post larvae and juveniles in restricted bays and backwaters (e.g., Cotton Bayou in Perdido Bay; Figure 4-1) are particularly susceptible to low DO because they have low mobility and capacity to avoid these low DO areas (Lassuy 1983). A

minimum DO level of 3 mg/L for *Gulf Menhaden* health was recommended by Christmas and Waller (1973).

Several studies have been conducted to simulate hydrodynamics and water quality in Perdido Bay. Xia et al. (2011) simulated salinity and DO in Perdido Bay and immediate near-shore Gulf of Mexico marine waters using the Environmental Fluid Dynamics Code (EFDC). These researchers divided Perdido Bay into two sections: lower Perdido Bay influenced by tidal forcing and upper Perdido Bay influenced by tidal forcing and freshwater inflows. This study confirmed that winds and tides influence salinity and DO distributions within Perdido Bay. Dynamic and complex interactions between tides from Gulf of Mexico and inflows from freshwater sources were revealed by the age of water (Devkota, 2014). Dolphin Pass linking to Big Lagoon and Perdido Pass linking to the Gulf of Mexico are the boundaries where most of the salt exchange took place (Figure 4-1) (Devkota & Fang, 2015). Sigsby (2013) used field and historical data to develop a three-dimensional sediment transport model. Freshwater inflow is the primary forcing factor in sedimentation, and it is the main contributor to sediment entering Perdido Bay. Xia and Jiang (2015) used the calibrated model previously developed by Xia et al (2011) to simulate bottom hypoxia in Perdido Bay in response to variable local winds and river discharges (Xia et al., 2011). Xia and Jiang (2015) found that freshwater could reach the bottom of the bay in shallow areas (depth <1 m) under high volume river discharge, reducing the severity of hypoxia and anoxia. Increasing river discharge had little effect on the bottom hypoxia and nutrient variation in deepwater. Also, a 5 m/s (11.2 mph) or greater southerly wind was sufficient to reduce nutrient stratification and reduce areal coverage of hypoxia.(Herb & Stefan, 2005). The influence of sea level rise and future morphology on tidal hydrodynamics along the northern Gulf of Mexico coast was also investigated (Passeri et al. 2016). An EFDC 3-D

hydrodynamic and water quality analysis was done by Li (2019) where the temporal and spatial distribution of salinity, water temperature and dissolved oxygen was simulated. The model covered the entire Perdido Bay-Wolf Bay system and had very little observed data for calibration.

Three-dimensional hydrodynamic-water quality modeling can potentially be used for conceptualizing and designing remedial strategies for improving water quality in complex estuarine systems. This chapter and the following chapter (Chapter 5) detail an EFDC+ study of areas within Perdido Bay critical to maintaining Gulf Menhaden health and examines potential remedial strategies for sustainably improving water quality within these areas. The approach used includes acquisition of historical data and collection of discrete and continuous monitoring data from specific locations useful for model development, calibration, and validation. Calibration and validation of the EFDC+ model is presented in this chapter. In the following chapter (Chapter 5), the calibrated and validated model is used to test several conceptual remedial strategies as a means of identifying the most appropriate remedies for improving and sustaining water quality, using Gulf Menhaden health requirements as indicators of sufficient water quality improvement.

4.2 Materials and Methods

4.2.1 Study Area

The CBTC system is located in the heart of Orange Beach, Alabama, and is a component of the larger Perdido Bay watershed, which is connected to the Gulf of Mexico by the Perdido Pass. The major freshwater inflow to Perdido Bay is from the Perdido River, which enters the bay from the northeast. Cotton Bayou is a shallow semi-closed water body that is in the Perdido and Wolf Bay system, with a surface area and average depth of 0.73 km^2 and 1.36 m,

respectively. The eastern end of Cotton Bayou is connected to Terry Cove and Perdido Pass; the pass is the only connection for the Perdido Bay system with the Gulf of Mexico (Figure 4-2).

Figure 4-2 Cotton Bayou-Terry Cove area

4.2.2 Model Used

EFDC+ was used to develop a site-specific model for the CBTC system. The EFDC model solves three-dimensional continuity, momentum, and free surface equations of motion (Hamrick 1992b) and uses a turbulence closure scheme (Mellor and Yamada 1982). Water level, water temperature, salinity and nineteen water quality parameters were simulated. DO was the main water quality parameter used for calibration and validation purposes. Several simulated water quality parameters are incorporated in the simulation of DO. Three algal classes were also simulated (green algae, blue-green algae and diatoms). Carbon (refractory particulate organic carbon, labile particulate organic carbon, dissolved organic carbon), phosphorus (refractory

particulate organic phosphorus, labile particulate organic phosphorus, dissolved organic phosphorus, total phosphate), nitrogen (refractory particulate organic nitrogen, labile particulate organic nitrogen, dissolved organic nitrogen, ammonia nitrogen, nitrate nitrite), silica (particulate biogenic silica, dissolved available silica), chlorophyll-a, and Chemical Oxygen Demand (COD) are also simulated to capture nutrient dynamics. The EFDC+ sediment sub-model was also used since for productive estuary systems, sediment fluxes play an important role in nutrient dynamics. Additional model details and related governing equations are provided in Section 1.3.2.

4.3 Continuous and Discrete Data Collection

Continuous monitoring data for model calibration were collected at three locations within the CBTC model domain using three In-situ Inc. Aqua Troll 600 vented probes: Terry Cove (L1), Marine Police (l2) and Sportsman's Marina (L3) (Figure 4-3). The probes were attached to adjacent existing structures approximately 2 ft above the sediment surface.

In-Situ Inc. Aqua Troll 600 probes are a five-port multiparameter sonde with capacity for four interchangeable sensors and an antifouling wiper (In-Situ Inc., 2022). Data are stored on the probes and periodically downloaded. Sensor options include temperature, conductivity, pH/ORP, optical dissolved oxygen (RDO), turbidity, chlorophyll-a, Phycocianin (BGA-PC), Phycoerythrin (BGA-PE), FDOM, Crude Oil, Rhodamine WT, Fluorescein WT, ammonium (ISE), chloride (ISE) and nitrate (ISE). The installed probes recorded water depth, chlorophyll-a, RDO concentration, RDO saturation, oxygen partial pressure, BGA-PE fluorescence, actual conductivity, specific conductivity, salinity, resistivity, density, total dissolved solids, temperature, and barometric pressure at two hours interval from 11/7/2023 to 7/28/2023 (264 days total).

Discrete water and sediment sampling was conducted at thirteen locations on 2/20/2023 and 7/28/2023. Water samples were analyzed for DO, total phosphate, ammonia nitrogen, nitrate-nitrite, dissolved available silica and chlorophyll-a. Sediment samples were analyzed for percent solids, total phosphate, ammonia nitrogen and nitrate-nitrite. These data are provided in Appendix B. Following initial model development, the model was calibrated using observed water level, temperature, salinity and water quality within the study area (Figure 4-3).

Figure 4-3 In-situ Inc. Aqua Troll 600 vented probes for continuous water data collection.

Table 4-1 Continuous Data Collection Probe Locations

Probe	Longitude	Latitude	Depth (m)
Terry Cove (L1)	-87.553273	30.286096	1.93
Marine Police/Perdido Pass (L2)	-87.554949	30.278656	1.07
Sportsman's Marina/Cotton Bayou (L3)	-87.563955	30.278656	0.98

Figure 4-4 Data collection map.

4.4 EFDC+ Model Calibration and Validation

The EFDC+ model for CBTC system was configured, calibrated, and validated in multiple steps (Table 4-2). An initial model domain was created and calibrated using a single grid mesh with relatively coarse cell dimensions covering the entire Perdido Bay-Wolf Bay system. Validation simulations for this initial model domain provided unacceptable results when comparing key validation parameters to direct sampling/monitoring (primarily DO), salinity, and water temperature). Based on this outcome, the model was reconfigured to include a nested grid mesh for Cotton Bayou-Terry Cove with smaller grid dimensions embedded within the initial model domain. Continuity of hydrodynamic conditions and material fluxes are maintained along

the boundaries delineating the initial grid mesh and the nested grid mesh. This new configuration provided acceptable results for key validation parameters when compared to observed results from direct sampling/monitoring, using calibration parameters employed when configured for the initial model domain. Sections 4.4.1 through 4.4.7 summarize model calibration; Section 4.4.8 summarizes the incorporation of the nested grid mesh into the model. The model calibration and validation periods are provided in Table 4-2. The simulation was conducted from 9/1/2023; the first two months of simulation helped the model parameters to stabilize.

Table 4-2 Calibration and Validation Timeline

		Start	End
Period 1	Calibration	11/07/2022	02/28/2023
	Validation	03/01/2023	03/31/2023
Period 2	Validation	05/01/2023	07/10/2023

4.4.1 Initial Model Domain

The initial EFDC+ model grid mesh is shown in Figure 4-5. The grid was used from a previous study (Li, 2019). The grid was further refined in the CBTC region and used for the current study. The initial model domain grid had a total of 5303 curvilinear cells with 118 grid rows and 267 grid columns. The cells had a mean dimension of 188.190 m (range: 6.219 m – 1212.807 m) and 213.896 m (range: 2.750 m – 783.421 m) in X and Y directions, respectively. Four vertical layers were simulated using a Sigma vertical grid.

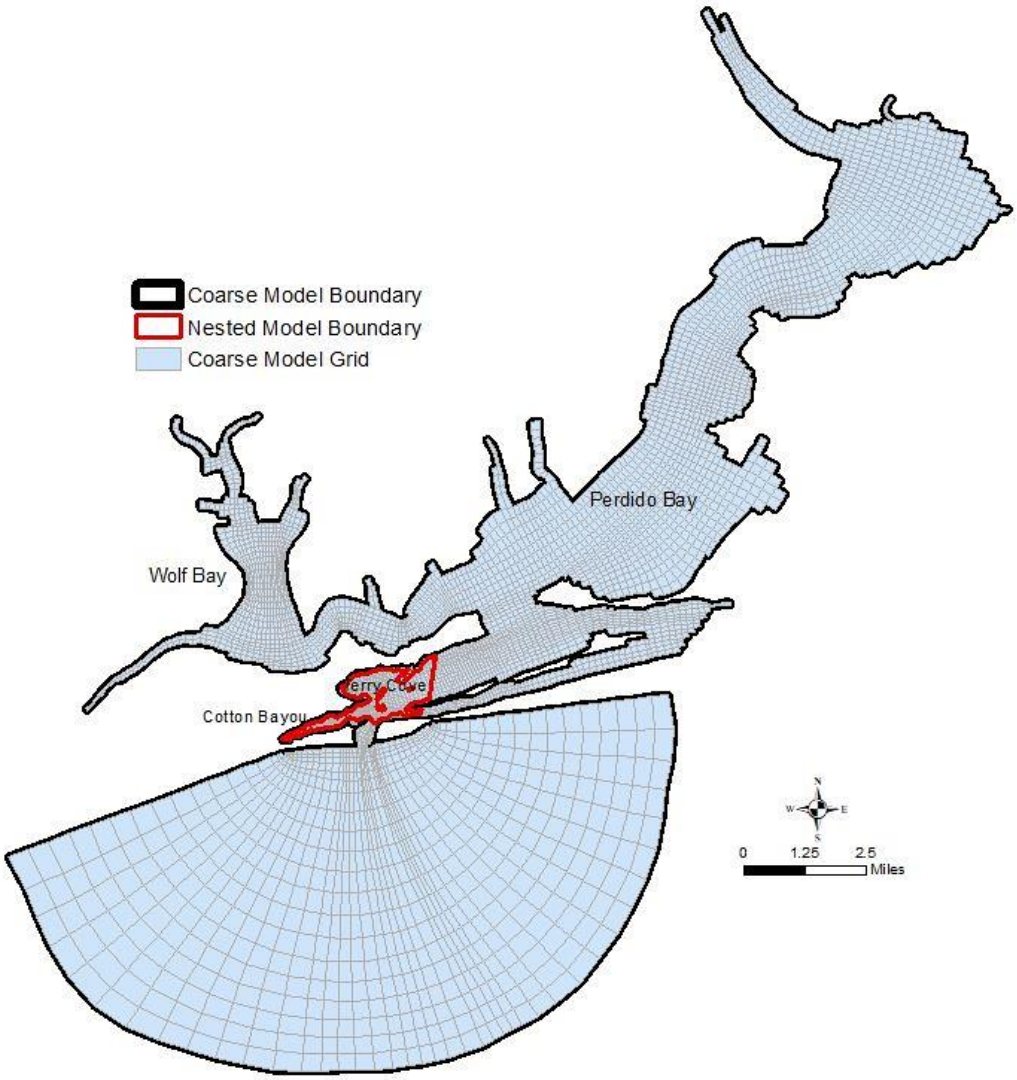

Figure 4-5 Model grid for the initial (coarse) model domain.

4.4.2 Bathymetry

Existing data were used to construct model domain bathymetry. Publicly available bathymetry data from the National Oceanic and Atmospheric Administration (NOAA) were used for the larger Perdido Bay-Wolf Bay system. The NOS Hydrographic Survey dataset was used for the bathymetry data. Measurement dates vary across the Perdido Bay system: the most recent bathymetry data for this area were collected in 2007 and the oldest data in 1985. For Cotton

Bayou, the most recent NOAA bathymetry data were measured in 1994. Bathymetry data were manually edited using ArcGIS to account for Robinson Island, Walker Island, and shore areas. The updated bathymetry data was used for modeling.

4.4.3 Boundary Conditions

Boundary conditions for the model domain are shown in Figure 4-5. The model domain was configured to account for the three primary hydrodynamic boundaries: (1) Perdido Pass into the Gulf of Mexico (GOM), (2) Dolphin Pass (between Perdido Bay and Pensacola Bay), and (3) Portage Creek (the Gulf Intracoastal Waterway (GIWW) between the Perdido Bay system and Mobile Bay). These are the primary boundaries where flow exchanges (inflow to Perdido Bay and inflow from/outflow to the Gulf of Mexico) take place. Open flow boundaries were used to represent the flow exchanges. Input data for the open boundaries were obtained from the nearest available observation stations. The open boundary at Perdido Pass used observed water temperature and dissolved oxygen (DO) data from the Alabama Real Time Coastal Observing System (ARCOS) Dauphin Island station. Water surface elevation data for Perdido Pass was collected from the Dauphin Island NOAA Station (Station 8735180). A constant salinity of 35 ppt was used for Perdido Pass. Measured water surface elevations at the Pensacola NOAA station (Station 8729840) from NOAA Tides and Currents were used for open boundary at Dolphin Pass to represent tidal influences from the Gulf of Mexico. The measured temperature at this station was used as the temperature boundary at Dolphin Pass. The time series of observed salinity at Florida Point from the Alabama Department of Environmental Protection (ADEM) monitoring station was used as the salinity boundary at Dolphin Pass. The open boundary at Portage Creek (GIWW) included measured water surface elevations at the US Geological Survey (USGS) Station 02378185, measured water temperatures at NOAA Station 8735180, and

measured salinity at the ADEM Orange Beach Waterfront Park (OWFP) monitoring station. Apart from these three primary open boundaries, the larger Perdido Bay-Wolf Bay has nine flow boundaries.

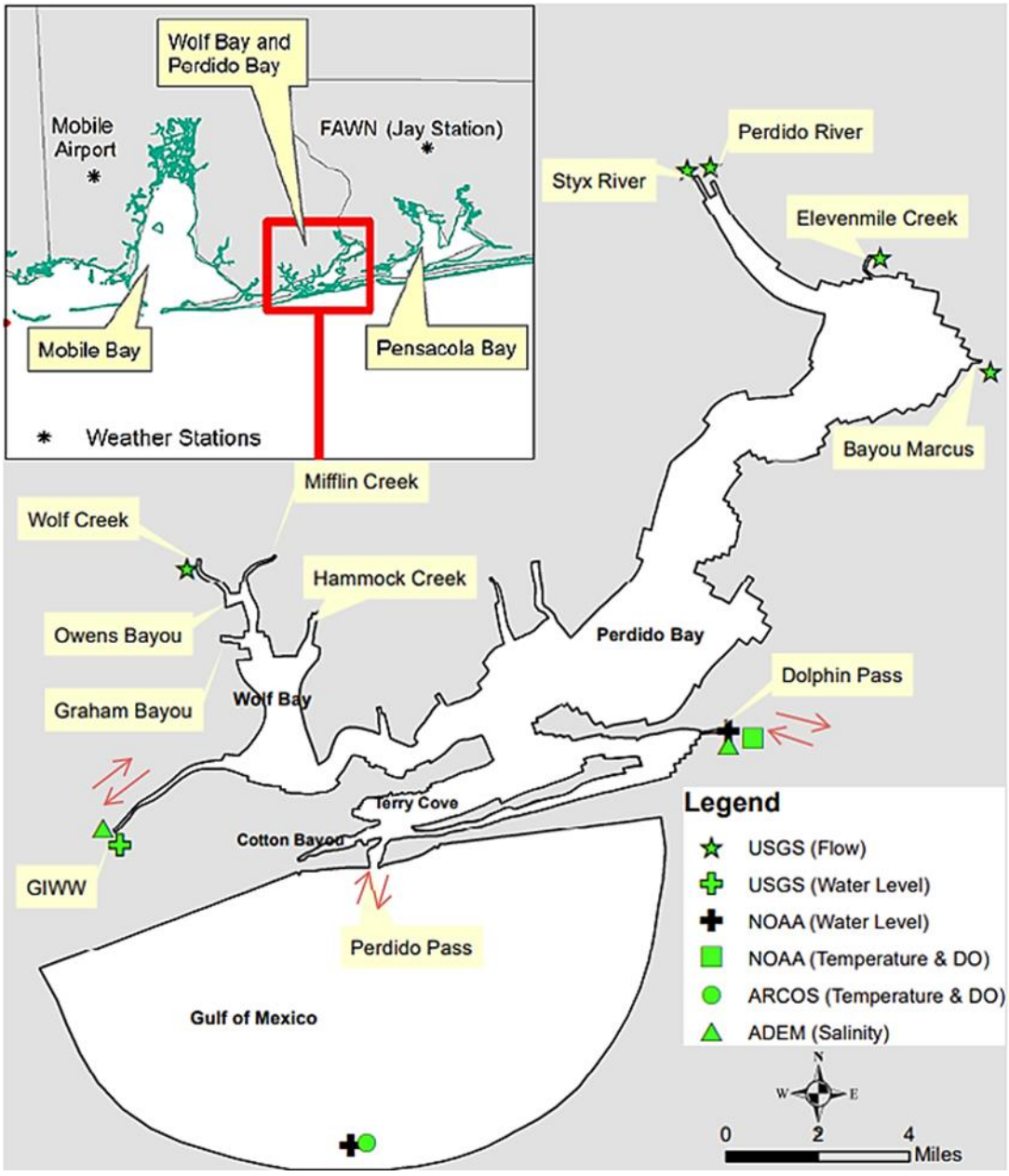

Figure 4-6 Unsteady boundary condition locations with the source of water level, water temperature and DO data. Locations of meteorological stations are presented in top-left corner.

The larger Perdido Bay system has four primary surface water inflows. Each of these four inflows has an associated USGS gauge station: Styx River (USGS 02377570), Perdido River (USGS 02376500), Elevenmile Creek (USGS 02376115) and Bayou Marcus (USGS 02376100). All these stations have up-to-date discharge and gauge height data that were used to establish hydrodynamic boundary conditions; however, the most recent water quality data are from 2005. Wolf Bay has five small inflow tributaries: Wolf Creek (USGS 02378170), Mifflin Creek, Owens Bayou, Graham Bayou and Hammock Creek. Only Wolf Creek has up-to-date discharge and gauge height data. For the other four tributaries, a constant flow of 0.15 cms was used.

4.4.4 Meteorology

EFDC+ water temperature and water quality simulations require meteorological data. EFDC+ atmospheric forcing input variables include nine meteorological parameters: atmospheric pressure (millibars), air temperature (°C), relative humidity (fraction), rainfall (m/day), evaporation (m/day), solar radiation (W/m^2), cloud cover (fraction), wind speed (m/s) and wind direction (degree). The required data were acquired from two monitoring stations: (1) the Mobile Regional Airport (40 miles northwest of Wolf Bay) and (2) the South Alabama Mesonet Jay Station (25 miles northeast of Wolf Bay). The South Alabama Mesonet is a network of 26 automated weather stations, located in the north-central gulf coast area. The Mobile Regional Airport monitoring station records all required meteorological parameters except solar radiation, and the Mesonet Jay Station records all parameters except atmospheric pressure and cloud cover. Meteorological data requirements were met by combined data from these two stations in the EFDC+ model.

4.4.5 Hydrodynamics

The Smagorinsky method (Catano-Lopera et al. 2023) was used to determine horizontal eddy diffusivity. A range of values were selected for horizontal eddy viscosity and horizontal momentum diffusivity. The most appropriate values were selected based on water level comparisons at the three continuous monitoring probe locations (Figure 4-3). The method developed by Kantha and Clayson (Kantha and Clayson, 1994) scheme was used to select parameters for vertical eddy viscosity and diffusivity. The Coriolis Effect plays an important role in hydrodynamics. EFDC+ computes a value for the Coriolis Effect based on the general latitude of the modeled site.

4.4.6 Water Quality

All EFDC+ water quality algorithms are dependent on water temperature. Meteorological data and water temperature at the model domain boundaries are used to calculate water temperature inside the model domain. EFDC+ has several surface heat exchange subroutines for use in a variety of climatological settings. The most appropriate subroutine for the model domain is the full heat balance model with variable extinction coefficients. A background light extinction coefficient of 0.7/m is used. The background light extinction coefficient was calculated from the Secchi depth data of previous years (Chapra, 1997). Coefficient of light extinction for Dissolved Oxygen matter (DOM), Chl-a and Particulate Organic Carbon (POC) are all selected as 0.01.

EFDC+ has the capability to simulate a broad range of water quality parameters. Out of the 22 available water quality parameters, 19 were selected for this study based on their relevance to this study. This includes three algal classes: green algae, cyanobacteria and diatoms; carbon (refractory particulate organic carbon, labile particulate organic carbon, dissolved organic carbon), phosphorus (refractory particulate organic phosphorus, labile particulate organic

phosphorus, dissolved organic phosphorus, total phosphate), nitrogen (refractory particulate organic nitrogen, labile particulate organic nitrogen, dissolved organic nitrogen, ammonia nitrogen, nitrate nitrite), silica (particulate biogenic silica, dissolved available silica), chemical oxygen demand (COD) and DO. EFDC+ algorithms for calculating COD, DO, and algal concentrations include parameters that are constants and were selected during model calibration based on measured values from field observations. Table 4-3 shows the various calibration parameters for cyanobacteria growth, metabolism, and predation.

Table 4-3 Water Quality Calibration Parameters

Parameter	Green Algae	Cyanobacteria	Diatom
Maximum Growth Rate (1/day)	2	1.5	0.5
Basal Metabolism rate (1/day)	0.5	0.3	0.1
Predation rate (1/day)	0.2	0.1	0.01
C: Chlorophyll ration (mg ^{o}C /µg Chla)	0.065	0.065	0.065
Stoichiometric algae O_2: C ratio (g O_2/g ^{o}C)	2.67	2.67	2.67
Nitrogen half-saturation (mg/L)	0.01	0.01	0.01
Phosphorous half-saturation (mg/L)	0.001	0.001	0.001
Lower optimal temperature for growth (^{o}C)	20	20	20
Upper optimal temperature for growth (^{o}C)	28	28	28
Reference temperature for basal metabolism (^{o}C)	20	20	20
Temperature effect Coeff for basal metabolism	0.069	0.069	0.069
Optimal depth for growth (m)	0.065	0.065	0.065

Some coefficients related to algal growth were adjusted based on the ranges suggested by relevant literatures (Burn and McBean, 1985). Reaeration is another factor that influences DO, and EFDC+ provides several subroutines for calculating this mechanism. In this study, the most

appropriate reaeration subroutine is the Constant & Wind Generated model, using the DO saturation formulation developed by Garcia and Gordon (Garcia and Gordon, 1992). In algal growth algorithms, EFDC+ uses a percentage of total incident solar radiation for photosynthesis based on calibration comparisons to field observations. In this study, 45% of the incident solar radiation was used.

4.4.7 Sediment Flux

EFDC+ allows a variety of methods for accounting for the exchange of nutrients, oxygen, and other water constituents with sediment (Fitzpatrick and Ditoro, 1993). For this study, constant flux values for key sediment nutrients and other water constituents were used, based on observed field parameters and adjustment during calibration. However, different COD values were used for different areas of the initial model domain to account for spatial variance. Figure 4-7 shows how different COD release rates were used in the EFDC+ model. The model was first simulated using a COD flux of 5 g/m^2/day for the whole model. Then, comparing with the observed DO data, it was found that Cotton Bayou and Terry Cove area has higher COD release rates. As part of the calibration effort, different COD release rates higher than 5 g/m^2/day were applied to these two areas. By comparing the simulated DO with the observed data at specific probe locations, the COD released rates were selected as 14 g/m^2/day and 9 g/m^2/day for Terry Cove and Cotton Bayou, respectively. Figure 4-8 represents how the sediment flux of COD affects DO concentration.

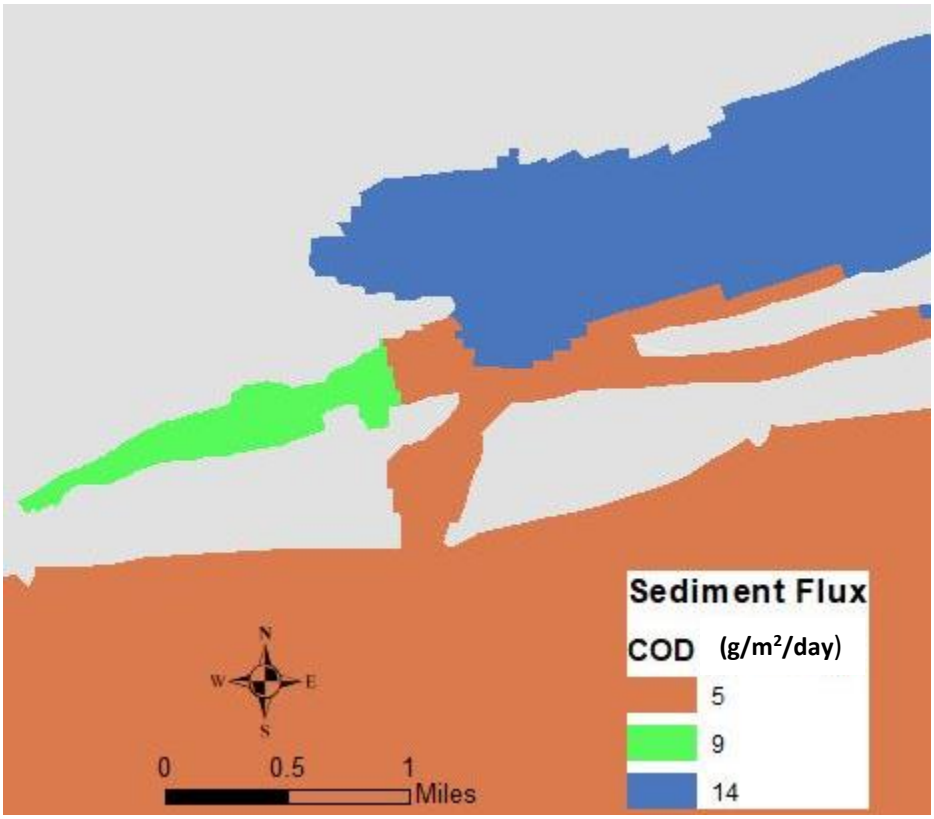

Figure 4-7 Sediment flux input of COD (from sediment to water, g/m^2/day) at CBTC in the coarse model

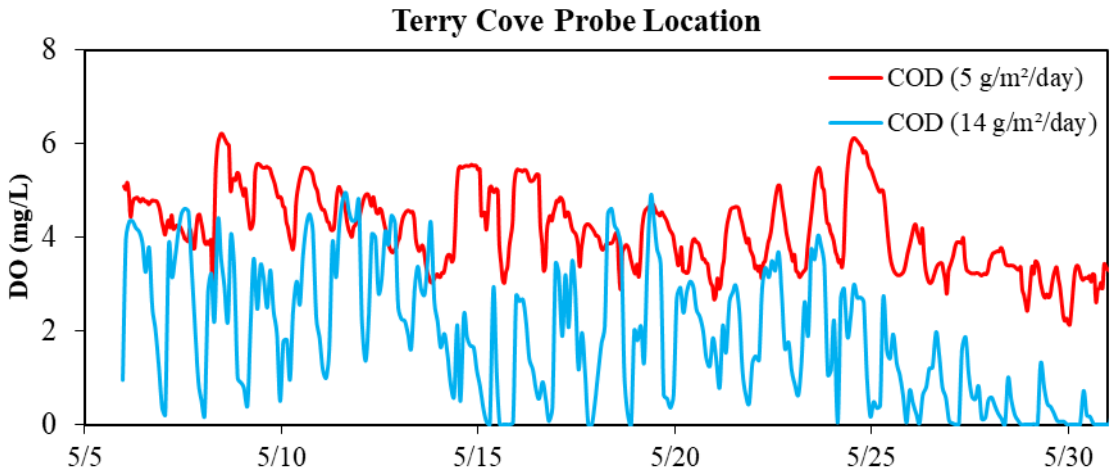

Figure 4-8 Simulated DO concentrations at Terry Cove probe location using two different COD sediment fluxes for that area.

4.4.8 Nested Model

The calibrated EFDC+ model includes a nested grid mesh for CBTC system with smaller grid dimensions embedded within the initial model domain. The nested grid was prepared using Grid+, a tool for creating 2D curvilinear orthogonal grids. The nested grid cells have a mean dimension of 36.707 m (range: 21.018 m – 141.012 m) and 37.074 m (range: 4.741 m – 105.587 m) in X and Y directions, respectively. The more spatially refined nested model more realistically represents spatial variations in bathymetry, which is especially important within the narrow confines of Cotton Bayou. This sensitivity is reflected in hydrodynamic and water quality representativeness when compared to observed data. Figure 4-9 shows the nested model grid for the CBTC system. Figure 4-8 shows the refined bathymetry within the nested model domain and the nested model grid boundary conditions, set at the southern and eastern boundaries. Hydrodynamic and material fluxes are passed between the two model grids along these boundaries.

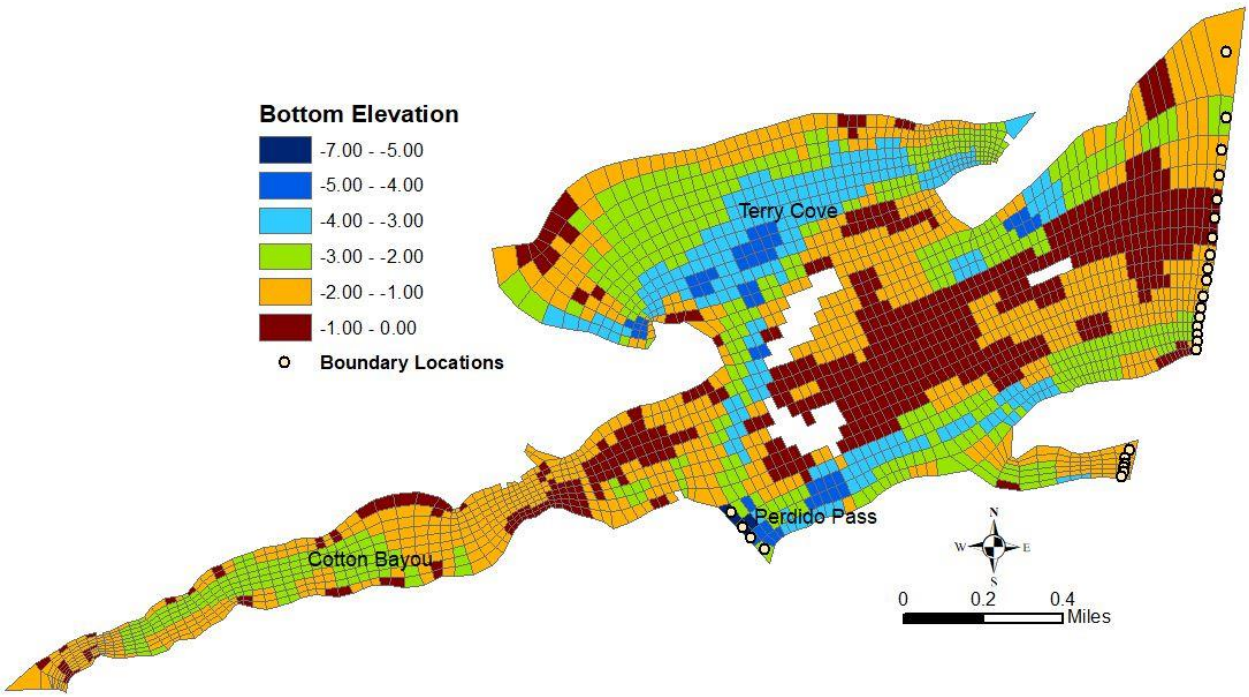

Figure 4-9 Boundary conditions and bottom elevation of nested model domain.

4.5 Calibration Results

4.5.1 Water Level Calibration

As the first step of calibration, model water levels were calibrated to match observed water levels at the three continuous monitoring probe locations. The parameters for the hydrodynamic modeling were adjusted. Figure 4-10 shows the comparison between the simulated water level and observed data. For the seasonal spring period, simulated water levels were higher than observed water levels at the Perdido Pass/Marine Police probe location (L2). For seasonal summer period, simulated water levels were lower compared to observed water levels at the Cotton Bayou probe location (L3). However, the Cotton Bayou probe water level data shows a sharp decrease during the summer period which was not observed for Terry Cove or Perdido Pass probe locations. Visual inspection of the L3 probe indicated that organic growth on the probe likely affected data collection during this period.

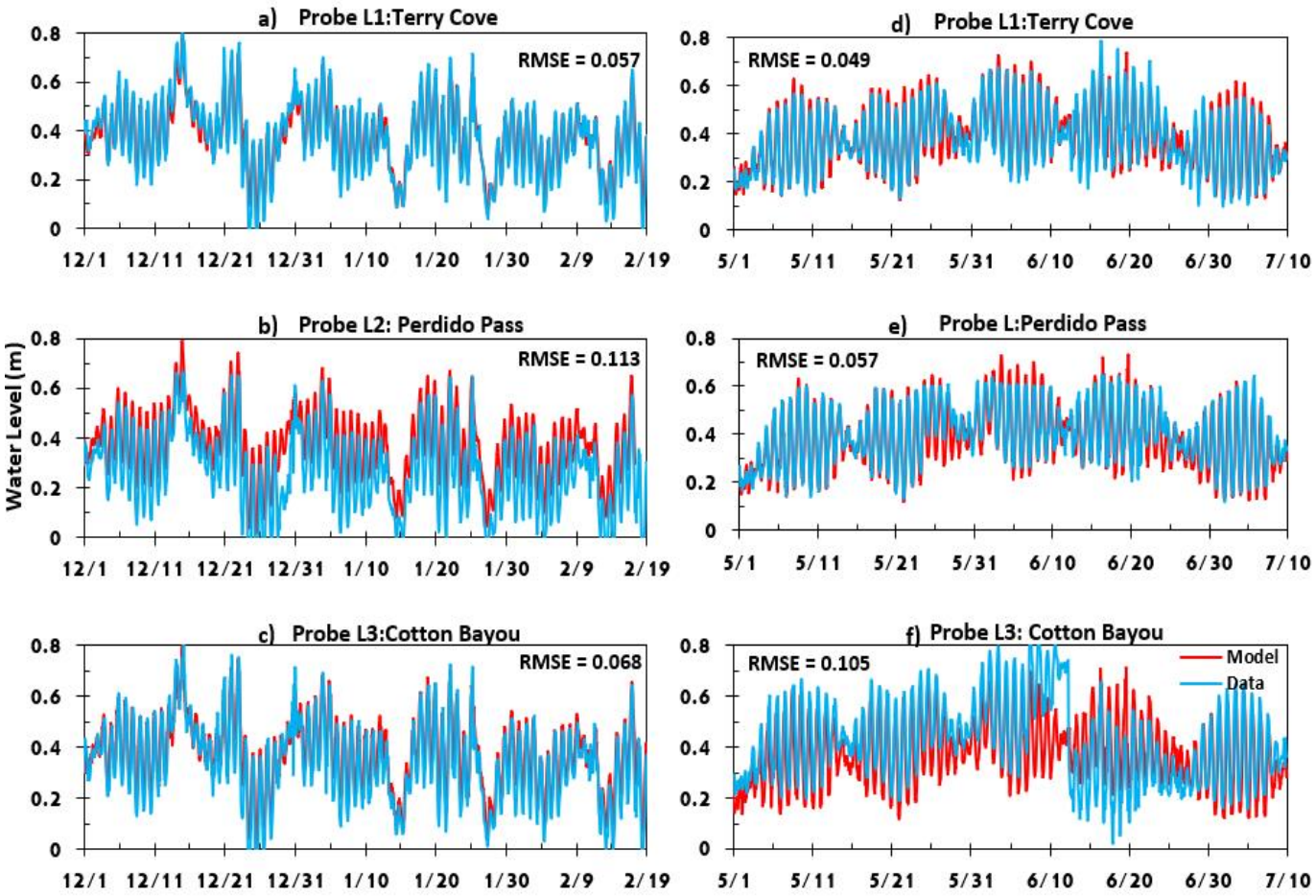

Figure 4-10 Observed and simulated water level at a) Terry Cove probe location from 12/01/2022 to 2/19/2023 (81 days); b) Perdido Pass probe location from 12/01/2022 to 2/19/2023 (81 days); c) Cotton Bayou probe location from 12/01/2022 to 2/19/2023 (81 days); d) Terry Cove probe location from 05/01/2023 to 07/10/2023 (71 days); e) Perdido Pass probe location from 05/01/2023 to 07/10/2023 (71 days); f) Cotton Bayou probe location from 05/01/2023 to 07/10/2023 (71 days).

4.5.2 Water Temperature Calibration

Figure 4-11 shows simulated and observed water temperatures at the three continuous monitoring probe locations. At Cotton Bayou, the model predicted lower temperatures than those

observed from 05/03/2023 to 06/20/2023 (48 days), after which the simulated temperatures matched well with observed data.

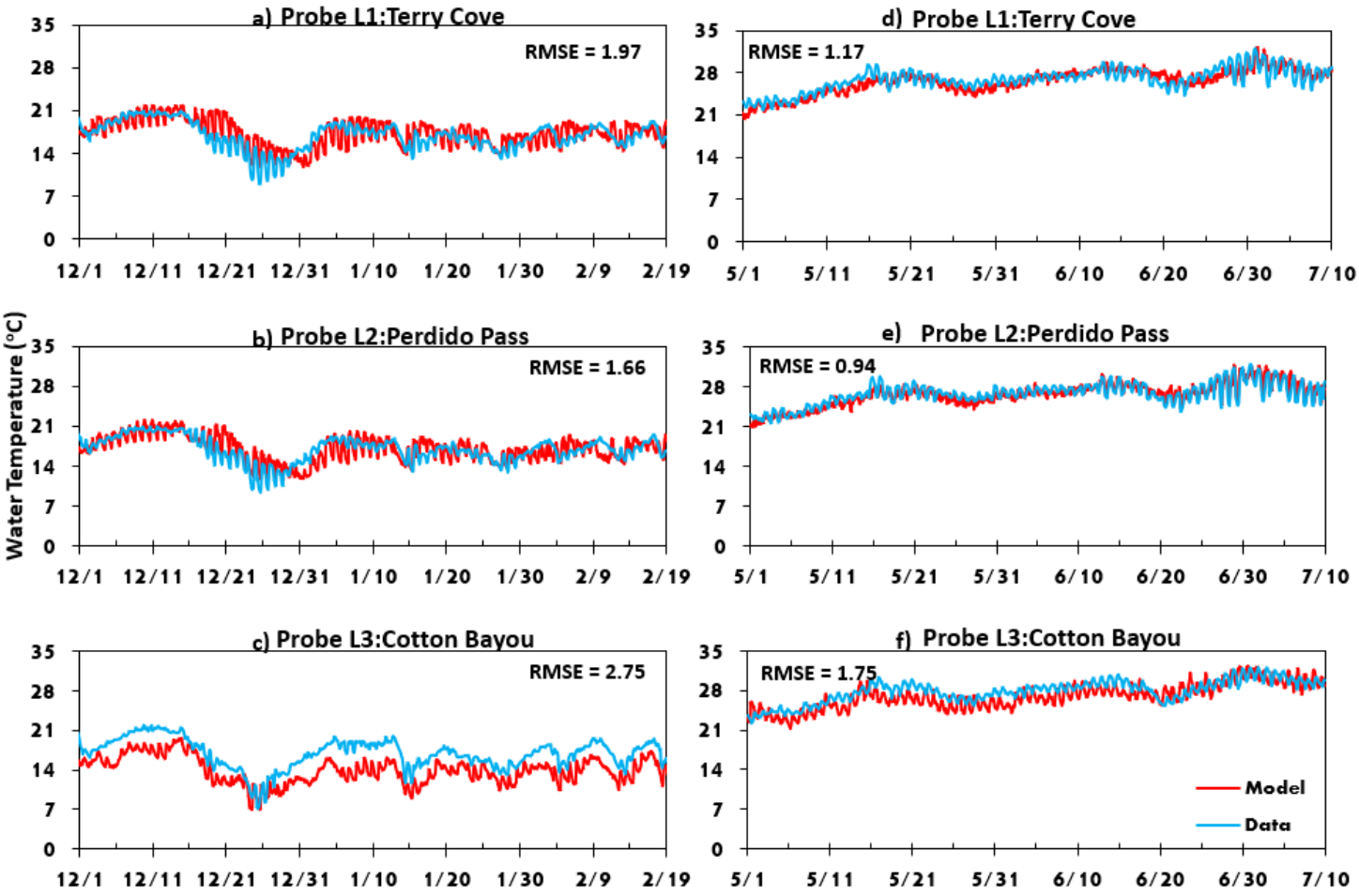

Figure 4-11 Observed and simulated water temperature at a) Terry Cove probe location from 12/01/2022 to 2/19/2023 (81 days); b) Perdido Pass probe location from 12/01/2022 to 2/19/2023 (81 days); c) Cotton Bayou probe location from 12/01/2022 to 2/19/2023 (81 days); d) Terry Cove probe location from 05/01/2023 to 07/10/2023 (71 days); e) Perdido Pass probe location from 05/01/2023 to 07/10/2023 (71 days); f) Cotton Bayou probe location from 05/01/2023 to 07/10/2023 (71 days).

4.5.3 Dissolved Oxygen Calibration

Eighteen simulated water quality parameters contribute to the simulation of DO. Figure 4-12 shows simulated DO during the seasonal spring period (81 days) at the three continuous monitoring probe locations. The Terry Cove, Perdido Pass, and Cotton Bayou probes collected DO data at 1.93 m, 1.23 m, and 0.98 m from the water surface, respectively. Simulated DO was extracted at the same depth as the probe measuring depths. Figure 4-12 shows the DO comparison between the calibrated model and observed data in the spring period (12/01/2022 to 02/19/2023, 81 days) at the three probe locations. The Root Mean Square Error (RMSE) at Terry Cove and Perdido Pass is 0.94 mg/L and 1.17 mg/L, respectively. At the Cotton Bayou probe, the RMSE is 2.7 mg/L. Hypoxic conditions were negligible at the Terry Cove and Perdido Pass probe locations. The observed DO time series at the Cotton Bayou probe location was considerably lower compared to the other two probe locations over the same time period. It is evident from Figure 4-11 that the Terry Cove and Perdido Pass areas maintained sub-lethal DO for *Gulf Menhaden* during the spring season. However, at Cotton Bayou, lethal DO was observed over several days in early December and early January.

Figure 4-13 shows the DO comparison between the calibrated and observed data during the seasonal summer 2023 period. This figure also demonstrates the differences between the coarse and nested models by comparing the simulated DO series extracted at the three probe locations. The coarse model simulated much higher DO at the Terry Cove probe location compared to observed data. The coarse model simulated nearly identical DO at the Terry Cove and Perdido Pass probe locations whereas the nested model captured DO differences between the Terry Cove and Perdido Pass probe locations. Due to complex hydrodynamics limiting mixing of inflowing and outflowing water in some CBTC areas, spatiotemporal variation in DO is

significant. Hence, a detailed nested grid with finer grid sizes can simulate water quality parameters more accurately.

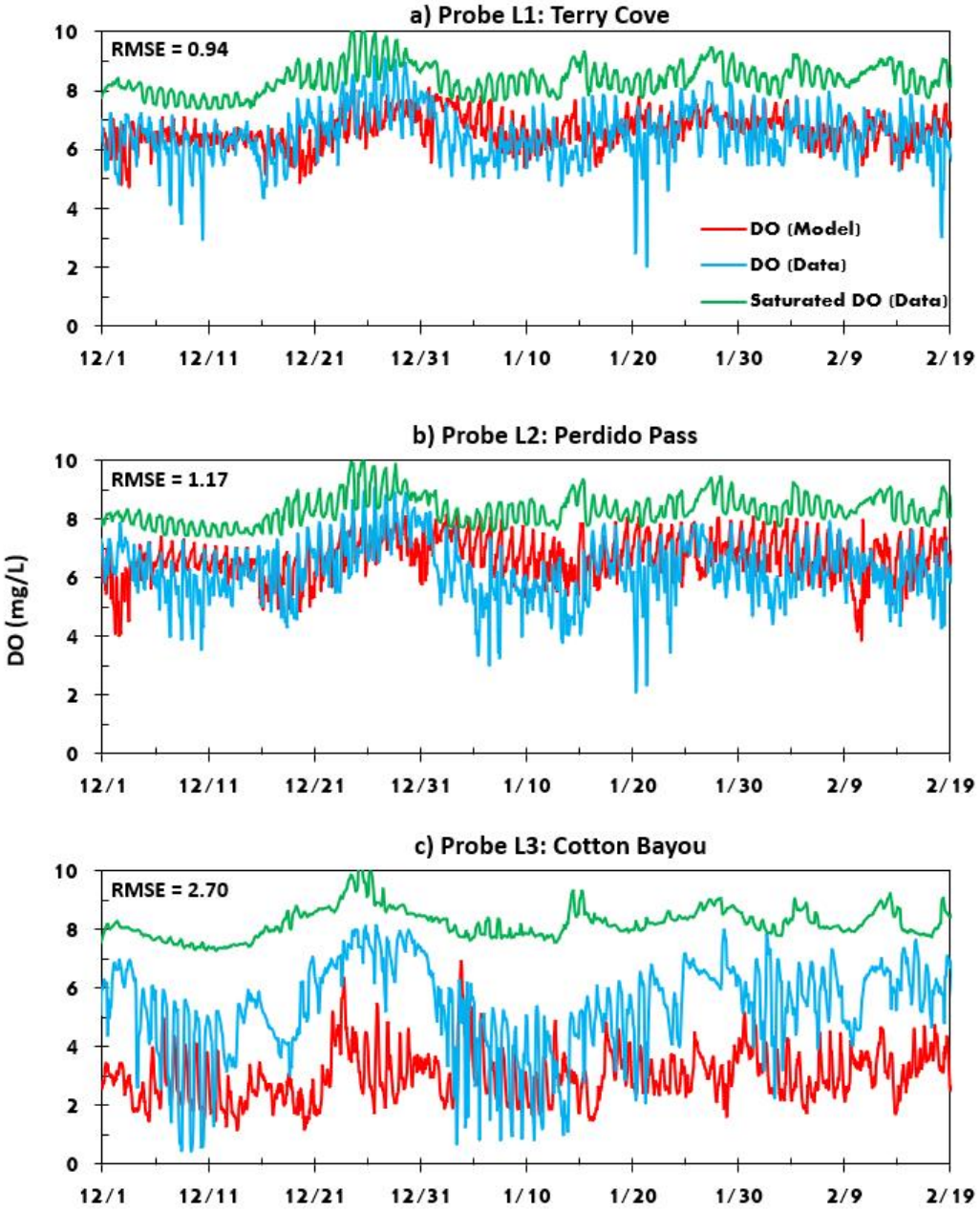

Figure 4-12 Simulated DO along with observed DO and saturated DO at a) Terry Cove probe location, b) Perdido Pass probe location and c) Cotton Bayou probe location from 12/01/2022 to 2/19/2023 (81 days).

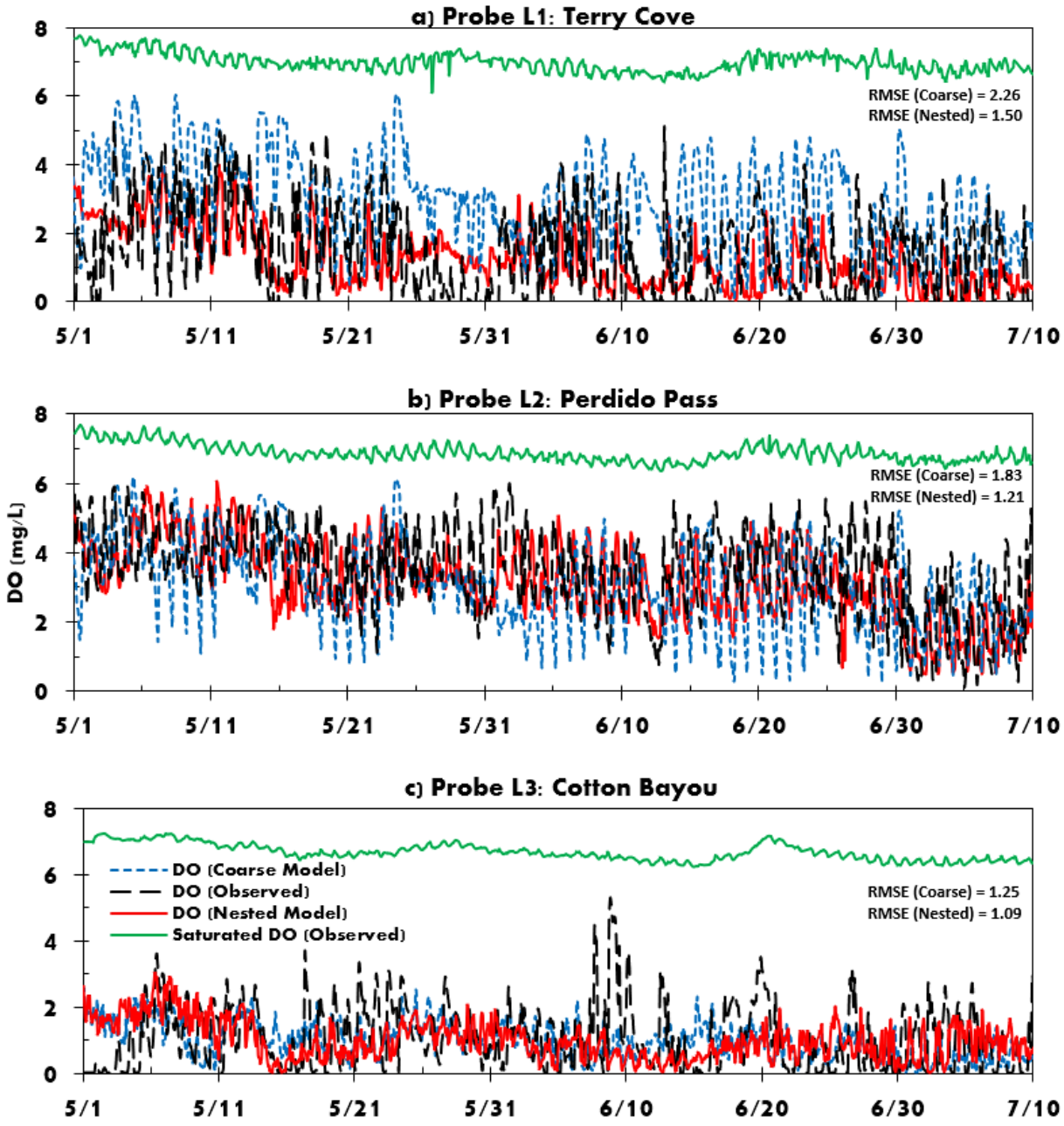

Figure 4-13 Observed and simulated DO concentrations at a) Terry Cove probe location, b) Perdido Pass probe location and c) Cotton Bayou probe location from 05/01/2023 to 07/10/2023 (71 days) using the Coarse Model and Nested Model.

Table 4-4 shows detailed low DO temporal distribution in observed probe data. In Spring, the Terry Cove and Perdido Pass probe did not have low DO days (with 2/3 days exception).

During the summer, DO at Perdido Pass remained below lethal DO for 278 hours. At Terry cove probe location, DO remained below lethal limit for 726 hours. The Cotton Bayou probe location had 810 hours of lethal DO and 119 anoxic hours. It can be said that the Terry Cove and Cotton Bayou locations had alarming lethal DO conditions. It should be noted that the probes were placed approximately 0.61 m above the sediment bottom.

Table 4-4 Number of Low DO Hours in Three Cells that has Continuous Probe Measurements (Figure 4-3)

	Number of hours					
	Probe L1: Terry Cove		Probe L2: Perdido Pass		Probe L3: Cotton Bayou	
	At 1.93 m from surface(max depth 2.54 m)		At 1.23 m from surface(max depth 1.63 m)		At 0.98 m from surface(max depth 1.54 m)	
	Spring	Summer	Spring	Summer	Spring	Summer
DO< 3 mg/L	2	726	3	278	78	810
DO < 1 mg/L	0	353	0	36	15	454
DO < 0.5 mg/L	0	258	0	8	2	319
DO = 0 mg/L	0	102	0	0	0	119

Note: The simulation period covers 1688 hours.

4.5.4 Spatial Variance of Dissolved Oxygen

Simulated DO in the CBTC area indicated that low DO persisted in Cotton Bayou and Terry Cove areas and near the islands south of Terry Cove. To further examine spatiotemporal variation in DO, three observation cells within the model domain were selected (Figure 4-14). Cell 1, 2 and 3 have bottom elevations of 3.4 m, 0.76 m and 2.2 m respectively.

Figure 4-14 Location of the reporting cells based on low DO.

Figure 4-15 shows the DO concentrations at the selected stations in the summer seasonal period in the surface and bottom layers. The surface layer had higher DO due to reaeration and photosynthesis. The surface DO started decreasing on 06-05-2023 due to water temperature being higher than the optimum temperature for algal growth. Simulated results indicate that CB has anoxic conditions over the time periods noted: 05-09-2023 to 05-11-2023, 05-13-2023 to 05-23-2023, 05-28-2023 to 06-01-2023 and 06-02-2023 to 07-10-2023. CB bottom layer DO was less than the lethal DO for the entire summer simulation period. Cotton Bayou had surface DO with levels above the lethal conditions for Gulf menhaden on 05-08-2023 to 05-09-3023.

Figure 4-15(c) shows significant stratification in Cotton Bayou. At Cotton Bayou, there were three periods of mixing in May which can be correlated with the high westward wind speed. The mixing period ranges from 05-01-2023 to 05-09-2023, 05-11-2023 to 05-13-2023, 05-23-2023 to 05-29-2023. The maximum wind speed in these three periods are 10.21 m/s, 14.87

m/s and 9.81 m/s, respectively whereas the average wind speeds are 4.5, 6.41, 5.2 m/s, respectively. These are higher than the average speed of 3.72 m/s for the Summer period. The bottom DO was highly dependent on COD and SOD, which was simulated individually in EFDC+. SOD ranges from 1.84 to 2.15 g/m^2/day on 05-01-2023 to 06-15-2023. However, from 06-16-2023 onwards, SOD started to increase ranging from 2.15 to 2.68 g/m^2/day.

Being located in a very shallow area between Robinson and Walker Island, Cell 2 had well-mixed conditions throughout the period. DO time series showed significant sensitivity to wind speed, wind direction and tides. Cell 2 had lethal bottom DO for 1595 hours (approximately 66 days). At the bottom layer, anoxic condition was observed in 31 hours at the bottom layer and DO of less than 1 mg/L was observed in 1123 hours.

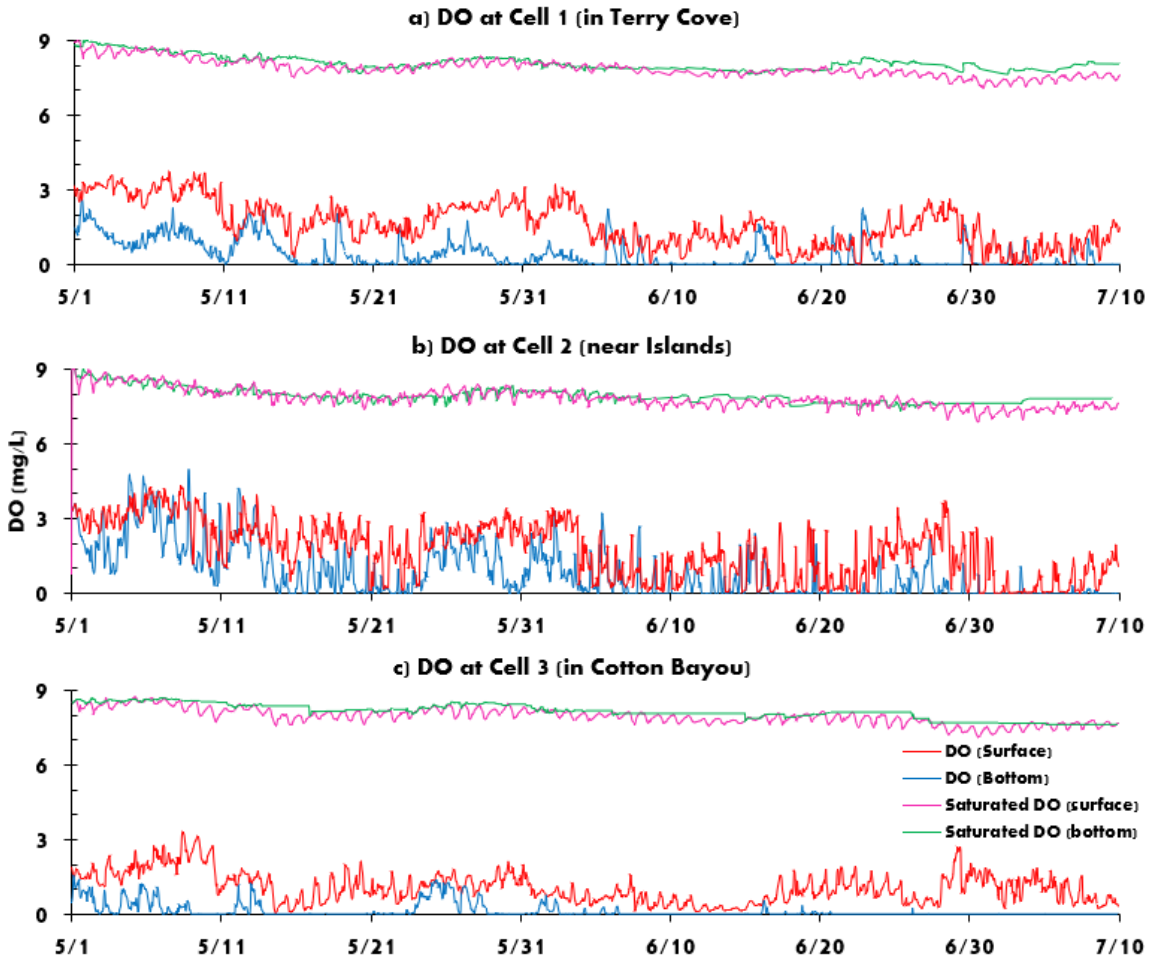

Figure 4-15 Simulated DO at surface and bottom layers at a) Cell 1 (in Terry cove); b) Cell 2 (near Islands); c) Cell 3 (in Cotton Bayou) locations from 05/01/2023 to 07/10/2023.

Table 4-5 Number of Low DO Hours in Three Reporting Cells (Figure 4-13)

	Number of hours					
	Terry Cove North (Cell 1)		Near Island Areas (Cell 2)		Cotton Bayou (Cell 3)	
	Surface Layer	Bottom Layer	Surface Layer	Bottom Layer	Surface Layer	Bottom Layer
DO< 3 mg/L	1542	1680	1444	1595	1670	1680
DO < 1 mg/L	453	1409	528	1123	836	1618
DO < 0.5 mg/L	177	1156	369	931	341	1501
DO = 0 mg/L	0	565	0	496	0	1163

Note: The simulation period covers 1688 hours.

Cell 1 is located on the north side of Terry Cove and has a depth of 3 m. Cell 1 experienced some stratification but had more mixing periods compared to Cotton Bayou. Cell 1 had lethal bottom DO for1680 hours, DO less than 1 mg/L in 1409 hours and anoxic condition on 565 hours. DO concentration and mixing varied significantly throughout the CBTC system. In July, much less stratification was observed in Terry Cove and near island areas compared to Cotton Bayou. Terry Cove had lower SOD in July compared to Cotton Bayou, which, in turn, caused higher DO at the bottom layers. SOD is calculated as a combination of carbonaceous SOD and nitrogenous SOD, which is dependent on particulate organic matter (POM) and ammonium (NH4) concentration, respectively. The change in SOD was due to the change in POM, while the NH4 concentration remained unchanged.

4.6 Conclusions

This chapter outlines the data collection and model calibration procedure for water level, water temperature and water quality parameters in CBTC system.

- The nested model simulated water level, water temperature and DO with good agreement with observed data. In Summer 2023, the RMSE for simulated DO at Terry Cove, Perdido Pass and Cotton Bayou probe locations were 1.50, 1.21 and 1.09, respectively.

- The nested model performed better than the coarse model in DO estimation as presented in Figure 4-12. The finer cell sizes and higher resolution enabled the model to capture the spatial difference in DO more accurately. Nested model approach is not usually used. However, it is a preferred approach when there are sub-domains in large model domain where more resolution is desired. For the CBTC area, the mean cell size was reduced by 80% in the nested model. Since the CBTC system is a small area in the overall coarse

(interim) model domain, the refined grid did not increase the simulation time significantly. The simulation time for the nested model was 30% more than the coarse model.

- The recommended DO level for *Gulf Menhaden* is 3 mg/L. However, based on the observed data and simulation results, there are periods of time in certain areas within the CBTC where *Gulf Menhaden* health is at risk. During 90% of the seasonal summer simulation period (05/01/2023 to 07/10/2023; 71 days), DO in the CBTC system was below the *Gulf Menhaden* lethal limit (Figure 4-14). Among the simulated 1688 hours in seasonal summer period, Cotton Bayou (Cell 3) had anoxic conditions for1163 hours. Terry Cove (Cell 1) and near-island (Cell 2) had anoxic conditions for 565 and 496 days, respectively. Cotton Bayou has less DO than the Terry cove and near-island region.

- DO concentration in the CBTC system is very sensitive to SOD and COD. Any natural system has different sediment characteristics at different parts of the waterbody. Therefore, in the initial model domain, different sediment flux of COD were assigned for Terry Cove, Cotton Bayou and Perdido Pass area. This approach resulted in a reasonable DO concentration (Figure 4-7) and captured the spatial differences more prominently.

Chapter 5 Predictive Modeling in Response to Different Restoration Techniques

5.1 Introduction

In the United States, 40% of the total population (over 124 million people) live along the coastline (NOAA, 2019b). Diverse habitats along the coasts provide many valuable ecosystem goods and services (EGS) that the coastal populations depend on (Barbier, 2013). Coastal counties produce more than $7.9 trillion in goods and services per year (NOAA, 2019). In 2006, the Gulf of Mexico lost over $800,000 per hectare (2018 USD) worth of EGS in the areas of property protection, recreation, food, and waste treatment due to land use change and coastal habitat loss (Mendoza-Gonzalez et al., 2012). While these losses in Gulf of Mexico were due to urbanization, it shows that the services provided by those habitats would not exist if the habitats were lost, including a loss from environmental change. The long-term losses of the EGS exceeded the short-term gains of urbanization (Mendoza-Gonzalez et al., 2012). Habitat loss that is already occurring due to development and urbanization is being exacerbated by environmental stressors. As urban development of coastal watersheds continues, estuaries and bays are becoming more eutrophic, and cascading effects are being felt at every trophic level. Managers and stakeholders need to have a suite of effective management tools that can be applied to coastal watersheds to minimize these effects of eutrophication.

There have been several studies regarding choosing the most effective management practices for estuaries (Bowen & Valiela, 2004). Bowen and Valiela (2004) combined an N loading model and estuary loading model to simulate the effectiveness of a number of potential management options that could be implemented in Waquoit Bay, Cape Cod, Massachusetts. Improvement of septic system performance, use of zoning regulations, preservation of forested tracts and freshwater bodies, installing wastewater treatment plants, controlling fertilizer use,

harvesting macroalgae, diversion of runoff from impervious surfaces, dredging etc. have been modeled as potential treatment options for the estuary. The choice of management practices depends on the water quality issue faced by the estuary. Harris et al. (2015) examined the effect of destratification and reaeration on nutrient and DO dynamics in Rock Creek, a 353-ha tidal creek tributary to the Patapsco River in the northern portion of Chesapeake Bay. In 1988, following the recommendation of the engineering company Dames and Moore (1988), an aeration system was installed that currently consists of 830 m of aeration pipes and 138 diffusers. The purpose of aeration is to destroy saline and thermal stratification that isolate bottom water from oxygen-rich surface water. Consequently, the destratified water column becomes responsive to tidal and wind energy that readily mixes oxygen-rich surface water to the bottom, thereby preventing anoxia. The installation cost for the aeration system in Rock Creek was $253,000 in 1988, with average annual electrical costs of $11,000 that have ranged from $6,350 to $14,000 between 2000 and 2010 (CH2MHILL, 2011). Although aeration can provide cost-effective improvement to water quality in estuaries, additional remedial actions (for example, reduction in nutrient loading) can provide cumulative positive environmental impacts (Conley et al., 2009).

The Waquoit Bay case study provides an example of a protocol that leads to identification of the most promising management options (Bowen et al., 2002). Dredging is another management technique for decreasing flushing time of the water in an estuary. Enhanced estuary transport of land derived N mixes nutrient-rich freshwater with nutrient-poor coastal marine water, reducing overall nutrient concentrations (Monsen et al. 2002). Targeted dredging to decrease flushing times has been proposed as a solution to eutrophication in many shallow coastal estuaries (Mallin et al. 2000). Bowen and Valiela (2004) assessed the potential of

dredging as a management option to improve water quality in estuaries through two-dimensional modeling.

Since the implementation of any management practice to enhance estuary water quality bears economic costs, assessment of potential remedial solutions leading to the selection of the most effective restoration techniques is very important. This chapter examines the utility of three-dimensional hydrodynamic and water quality modeling in the assessment and selection of remedial measures designed to materially improve water quality in an estuary, using the CBTC area within the Perdido Bay estuary as a test case. The calibrated EFDC+ model described in Chapter 4 is used for this examination, considering targeted dredging and forced aeration (both individually and in combination). The overarching goal of this study is to identify the most effective remedial measures for reducing hypoxia in the CBTC area (Figure 4.1), using Gulf Menhaden DO requirements as a guide, and predict overall improvements in water quality resulting from implementation of selected remedial measures.

5.2 Materials and Methods

5.2.1 Water Quality Conditions in the Study Area

The Perdido Bay watershed encompasses approximately 3238 km^2, roughly 2/3 of which is in Alabama and 1/3 is in Florida. Land use in the watershed includes urban development (primarily in the southern portion of the watershed including Orange Beach), upland forest, and agriculture. There are major timber companies operating in the watershed, including International Paper Corporation, DuPont Champion, and Scott Paper Company. Additionally, facilities associated with the Pensacola Naval Air Station are located in the watershed. There are a number of known hazardous waste sites within the watershed, including a former Superfund site and several Florida Department of Environmental Protection (FDEP) hazardous waste sites.

Degradation of water quality within the watershed resulting from known and unknown point and nonpoint pollution has been well documented (McPherson et al., 2004; Hadley, et al., 2006). Because Perdido Bay is shallow (average depth of 2 m) and small (130 km^2) relative to its watershed (3238 km^2), water quality varies rapidly in response to meteorological events and tidal movement (Hadley, et al., 2006).

Several documented fish kills have occurred within Perdido Bay (Cole, 2017; Li, 2019), suspected to be caused by periodic hypoxia events in areas within the bay susceptible to poor hydrodynamic mixing (in particular the CBTC area, Figure 4-2). The primary species involved in these fish kills is *Gulf Menhaden*. In estuaries, juvenile *Menhaden* have been captured in water with a salinity range of 0 to 35 ppt and a temperature range of 5 to 35 °C (Benson 1982; Christmas and Waller 1973). Lassuy (1983) reported that the suitable water temperature for *Menhaden* is around 30 °C. Post larvae and juveniles in restricted bays and backwaters (e.g., Cotton Bayou) are particularly susceptible to DO due to their low mobility and inability to avoid low DO areas (Lassuy 1983). A minimum DO level of 3 mg/L was suggested for *Gulf Menhaden* survival (Christmas and Waller 1973).

The most impacted area for fish kills in Perdido Bay is the CBTC area (Figure 4-3), and the EFDC+ model developed and calibrated in the previous chapter focused on this area. In this chapter, the calibrated EFDC+ model for Perdido Bay and the CBTC area is used to test proposed remedial measures for the CBTC area. These remedial measures include forced aeration, dredging, and combination of both, with the primary modeling goal of maintaining DO concentrations above 3 mg/L.

5.2.2 Model Used

The calibrated 3-D hydrodynamic and water quality model EFDC+ was used to test the proposed remedial measures. Jet/Plume and open boundary conditions were used to simulate aerator effects. Dredging was simulated by changing bottom elevations. Water level, water temperature, salinity, DO and 18 other water quality parameters were simulated. The calculation procedure of the jet/plume sub model is mainly based on Lee and Cheung (1990). The trajectory of a group of plume particles is traced in time using a Lagrangian formulation. The plume puff gains mass as ambient fluid is entrained and mixed within it, but once entrained, the new mass becomes an indistinguishable part of the plume puff. In the simplest version, the plume is assumed to be essentially a cylindrical segment whose radius grows as mass is entrained. The initial plume mass is identified as the mass issuing from a diffuser with radius b_0

$$M_0 = \rho_0 \pi b_0^2 h_0 \tag{5.1}$$

where, M_0 is the initial mass, ρ_0 is the initial density, b_0 is the diffuser radius, h_0 is the length of the plume mass and is chosen to be comparable to b_0. For example, h_0 = r and b_0 = r, where r is the radius of the diffuser. The initial length of the plume can be estimated from the initial plume velocity V_0 and time Δt: $h_0 = V_0 \Delta t$. The increment in the plume mass at the n^{th} time step is the sum of the plume mass increment due to the shear-induced entrainment and the forced entrainment. The increase in mass of the plume element is due to turbulent entrainment of the ambient flow. Close to the discharge point, or in a very weak current, shear-induced entrainment dominates. In general, however, the forced entrainment of the cross flow dominates, except very close to the source. In the model, assuming the total entrainment is a function of the horizontal

currents and a shearing action of the plume relative to the currents, the increase in mass due to shear entrainment, ΔM_s; is written as

$$\Delta M_s = \rho_a 2\pi b_n h_n E|V_n - u_a \cos\Phi_n \cos\theta_n|\Delta t \quad (5.2)$$

Where the jet axis makes an angle of Φ_n with the horizontal plane, and θ_n is the angle between the x-axis and the projection of the jet axis on the horizontal plane. ρ_a is the ambient density and u_a is the ambient current. The subscript n denotes the value of the plume element at the n^{th} step of calculation, the subscript a denotes the local ambient value, E is the entrainment coefficient which is dependent on the local densimetric Froude number F_1 and jet orientation

$$E = \sqrt{2}\frac{0.057 - 0.554\frac{\sin\theta_n}{F_1^2}}{1+5\frac{u_a\cos\Phi_n\cos\theta_n}{|V_n - burn}} \quad (5.3)$$
$$u_a\cos\Phi_n\cos\theta_n|$$

$$F_1 = \alpha\frac{|V_n - u_a\cos\Phi_n\cos\theta_n|}{\sqrt{g\frac{\Delta\rho_n}{\rho_a}b_n}} \quad (5.4)$$

α is a proportionality constant.

Experimental observations by Chu and Goldberg (1984) and Stuart Churchill (1975) have shown that the transfer of horizontal momentum is complete beyond a few jet diameters. It is assumed that all the ambient flow on the downdrift side of the plume is entrained into the plume element. This forced entrainment of the ambient flow into an arbitrarily inclined plume element can be formulated as

$$\Delta M_f = \rho_a u_a[2b\Delta s\sqrt{1-\cos^2\Phi\cos^2\theta} + \pi b\Delta b\cos\Phi\cos\theta + \frac{1}{2}\pi b^2\Delta(\cos\Phi\cos\theta)] \quad (5.5)$$

In the equation, the first term represents the forced entrainment due to the projected plume area normal to the cross flow; the second term is a correction due to the growth of the plume radius; and the third term is a correction due to the curvature of the trajectory.

The jet-plume model is implemented by calculating the mass entrained at each step. Given the increase in mass due to turbulent entrainment, the plume element characteristics at the next step are obtained by applying conservation of mass, horizontal and vertical momentum, energy, and tracer mass to the discrete element using generalized Lagrangian model.

5.3 Potential Restoration Scenarios

Predictive simulations to examine potential restoration scenarios and determine the most effective restoration alternatives for improving water quality, were performed using the final calibrated and validated EFDC+ model for CBTC system (Chapter 4). In order to eliminate the issue of low DO in the summer, the low DO regions were first identified at different time periods. Figure 5-1 shows the DO distribution in the study area at 15 day intervals starting from 05-01-2023. Figure 5-1 shows that hypoxia was observed in the CBTC area during the entire study study period (05-01-2023 to 07-10-2023; 71 days). The suggested DO concentration for *Gulf Menhaden* survival is 3 mg/L (Li, 2019). The lowest DO concentration in the CBTC system was observed between 12 pm to 4 pm (Figure 5-2). Throughout this chapter, the simulated DO concentrations at the bottom layer were extracted at three selected cells (Figure 5-3) to identify the effect of different restoration measures. The proposed restoration measures tested in this chapter are presented in Table 5-1.

Table 5-1 Potential Restoration Scenarios to Enhance Water Quality, Guided by Final EFDC+ Model Predictive Simulations.

Restoration Scenario
1. Targeted placement of forced aeration system in critical locations predicted by model
2. Modification of bathymetry (dredging) in critical locations predicted by model
3. Combinations of 1 and 2 as guided by model
4. Installation of hydraulic connection between the Gulf of Mexico and Cotton Bayou

The calibrated model of CBTC system explained in Chapter 4 was used as the base model. The predictive simulations were conducted for Summer 2023 (05-01-2023 to 07-10-2023, 71 days). To implement the aerator installation into the model, two different approaches were used: Jet/Plume boundary condition and open boundary condition.

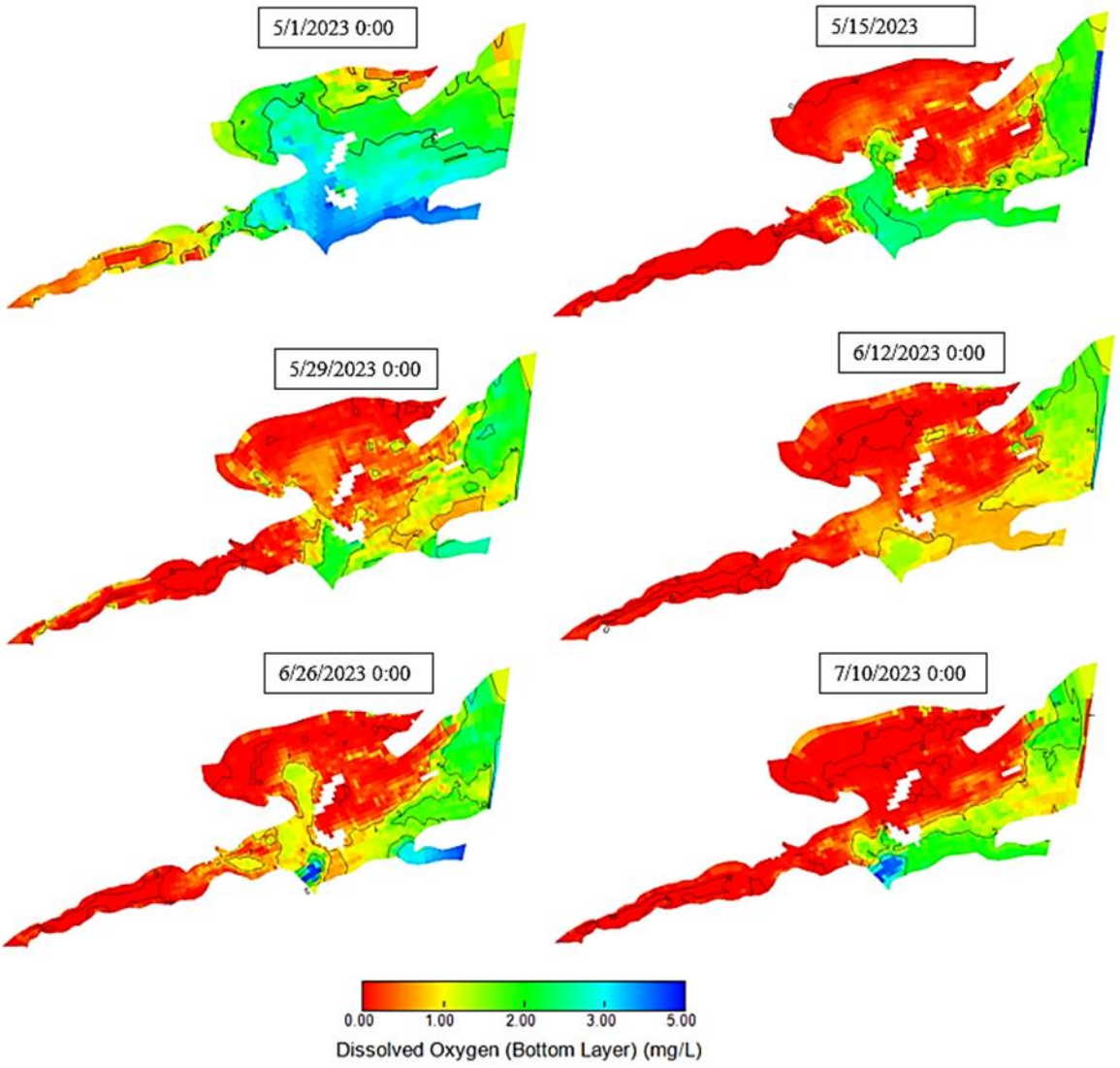

Figure 5-1 DO distribution in the CBTC system from existing (baseline) condition nested model simulation.

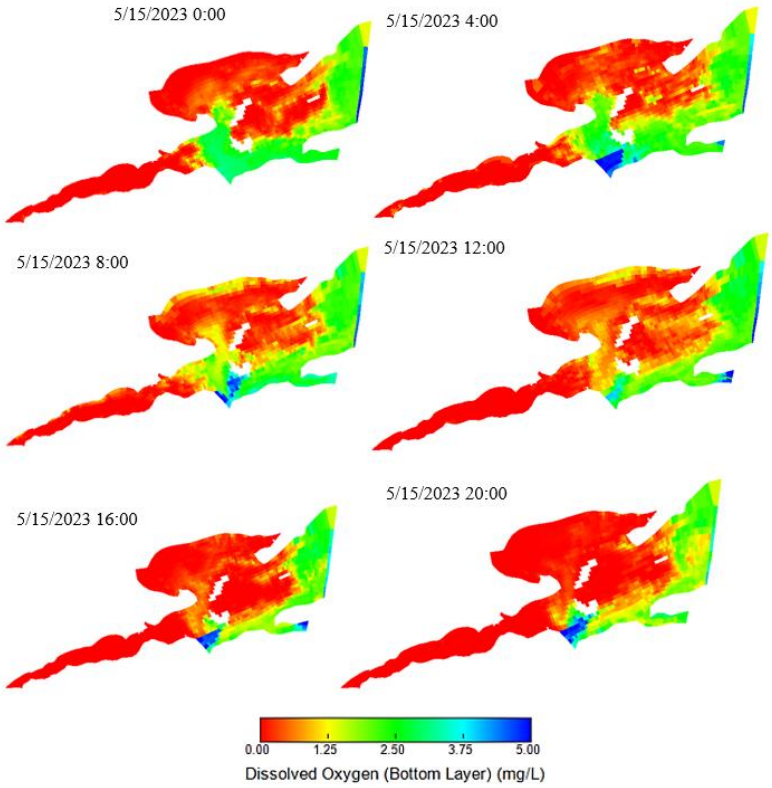

Figure 5-2 Hourly DO distribution in the CBTC system from existing (baseline) condition nested model simulation.

5.4 Aerator

5.4.1 Jet/Plume Boundary Condition

The calibrated EFDC+ model for the CBTC area was used as baseline model with changes in boundary conditions to incorporate the addition of aerators. The Jet/Plume boundary condition was used to perform predictive simulations under targeted placement of forced aeration systems in critical locations in CBTC area. It was assumed that aerators similar to ADS FTC fine bubble aerators (https://airdiffusion.systems/) would be placed at the sediment surface. These aerators have already been used to oxygenate many wastewater treatment facilities, eutrophic lakes and potable water and industrial wastewater tanks. The diameter of each aerator disc is

1.33 m (disc surface area 1.39 m^2 or 15.0 ft^2). The aerators were placed at specific model grid cells. To set up the boundary condition, the minimum flow (0.5 cms) allowed by EFDC+ for the Jet/Plume boundary condition was used for each aerator disc. The Jet/Plume boundary condition was set up based on the reasoning that the placement of aerators will drive the DO concentration in the model cell to near saturation. Total number of aerators needed to make a model cell saturated was determined by EFDC+ modeling. Based on the dimension of the model cell, twelve to fifteen aerator discs (with 1.33 m diameter) were required to drive the DO concentration near saturation. The model grid cells have mean dimensions of 36.707 m (range: 21.018 m – 141.012 m) and 37.074 m (range: 4.741 m – 105.587 m). For each cell where an aerator is located, fifteen aerator discs were placed (total aerator flow of 15×0.5 cms and total disc surface area of 20.8 m^2 or 224.3 ft^2). This set of fifteen aerator discs is mentioned as 'aerator set' in this chapter. The aerator locations were determined by examining flow patterns and velocity vectors. Cells with dynamic velocity patterns were selected to ensure mixing of the aerator DO. Flow from a disc has vertical velocity based only on buoyancy. After selecting initial locations, varied locations (or model grids) were tested to achieve the optimum locations and number of aerators. The grid sizes where aerator discs are placed range from 494 to 2842 m^2. Figure 5-3 shows three of the many configurations tested for aerator installation. A constant temperature of 23^{o}C, constant salinity of 25 ppt and constant DO of 9 mg/L (close to the saturated DO at 23^o C) were used for the jet boundary condition.

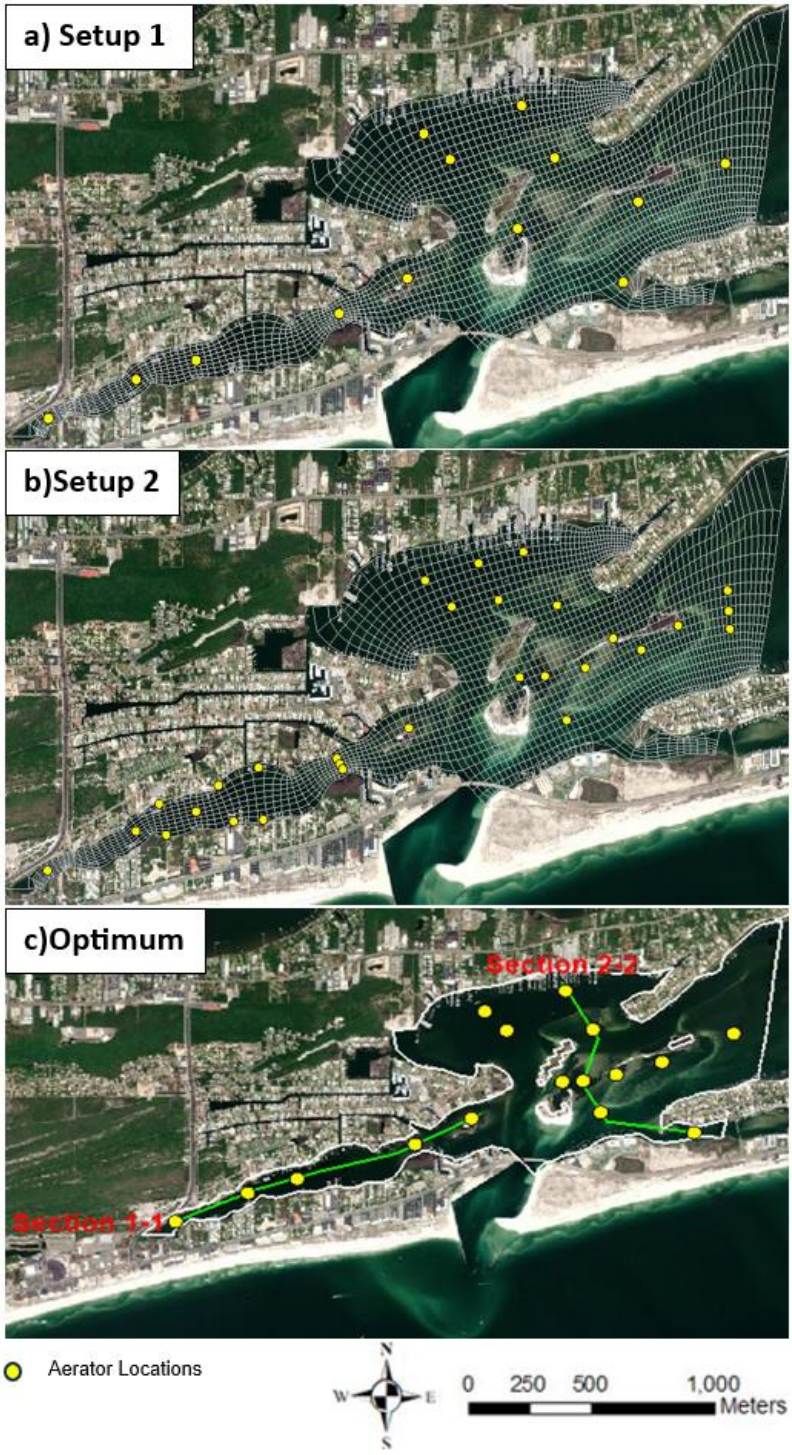

Figure 5-3 Three setups for aerator locations (yellow dots) in Cotton Bayou Terry Cove (CBTC) system to eliminate low DO problem.

Figure 5-4 shows the difference in DO at three cells after aerator installation. Configuration 1 has 13 locations with aerators. Configuration 2 and the optimum configuration 3 have 28 and 18 locations, respectively. Configuration 1 and the optimum configuration both have four grids with aerator sets placed in the Terry Cove area whereas configuration 2 has six grids with aerator sets. Figure 5-4(a) shows that though six aerator locations could result in higher DO, the four-grids aerator placement also increases DO to higher than 3 mg/L which exceeds the survival threshold for *Gulf Menhaden*. Figure 5-4(b) shows the DO time series at the Cotton Bayou (Cell 3) location forboth the existing and proposed condition. This figure shows that in Cotton Bayou, the temporal variation in bottom DO is minimal for the proposed condition. This area has minimal mixing or transport of water, so oxygenated water remains in the bayou. The shallow area between the islands is difficult to oxygenate, andthe application of two sets of aerators is not adequate for this area. If two grids with aerator discs are used, the area between Walker Island and Robinson Island would still have DO levels less than 3 mg/L. Therefore, an optimum arrangement of four sets of aerators was selected for the shallow near-island areas.

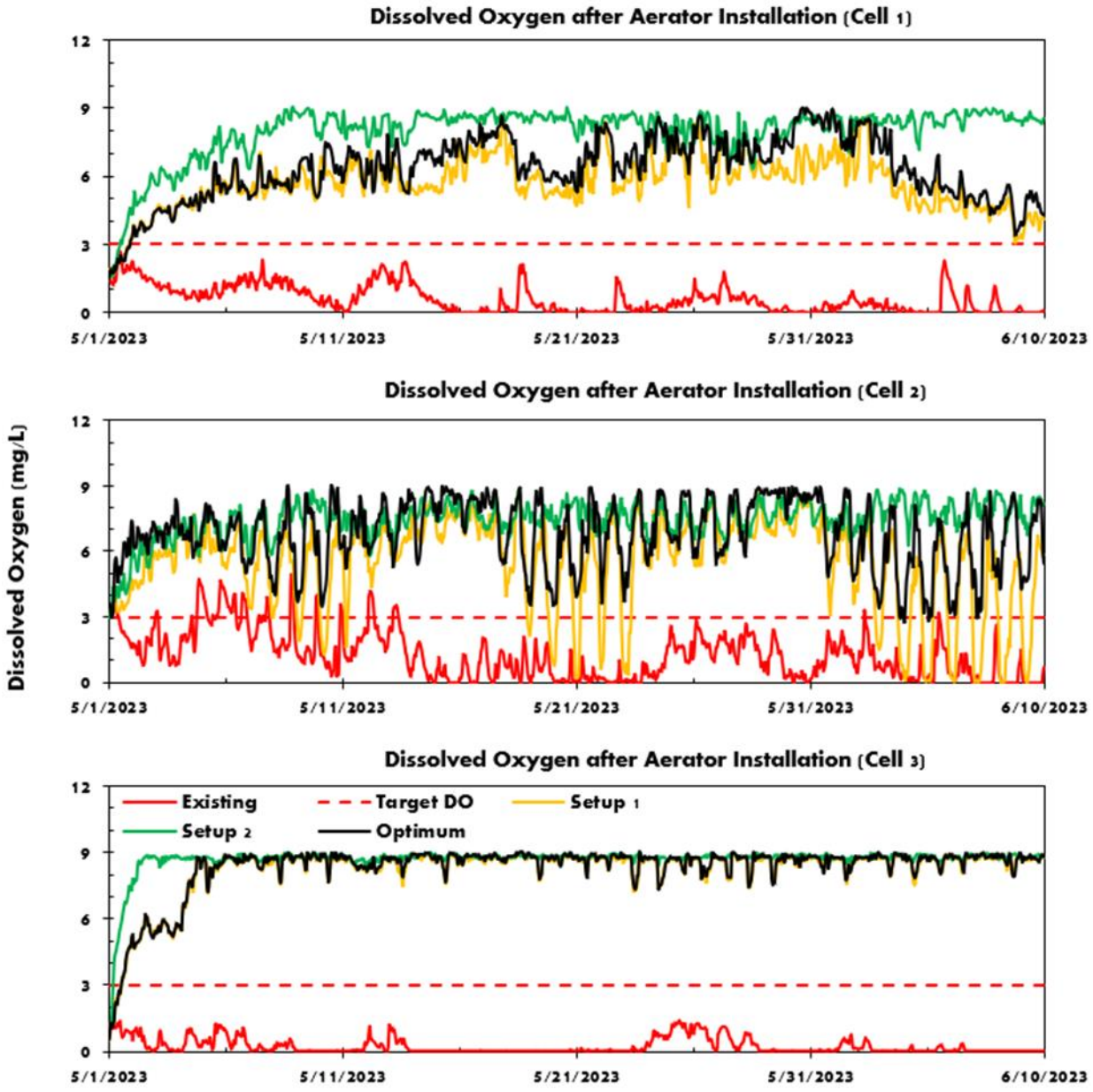

Figure 5-4 Dissolved oxygen concentration at selected cells (Figure 4-13) in response to different aerator setups compared with existing and target DO.

Figure 5-5 shows the longitudinal distribution of DO along a section cut through section 1-1 in Figure 5-3 (c). Figure 5-5(a) and 5-5(b) shows the DO distribution over depth on 05-10-2023 12:00 and 05-15-2023 16:00 for the existing (baseline) condition simulation.

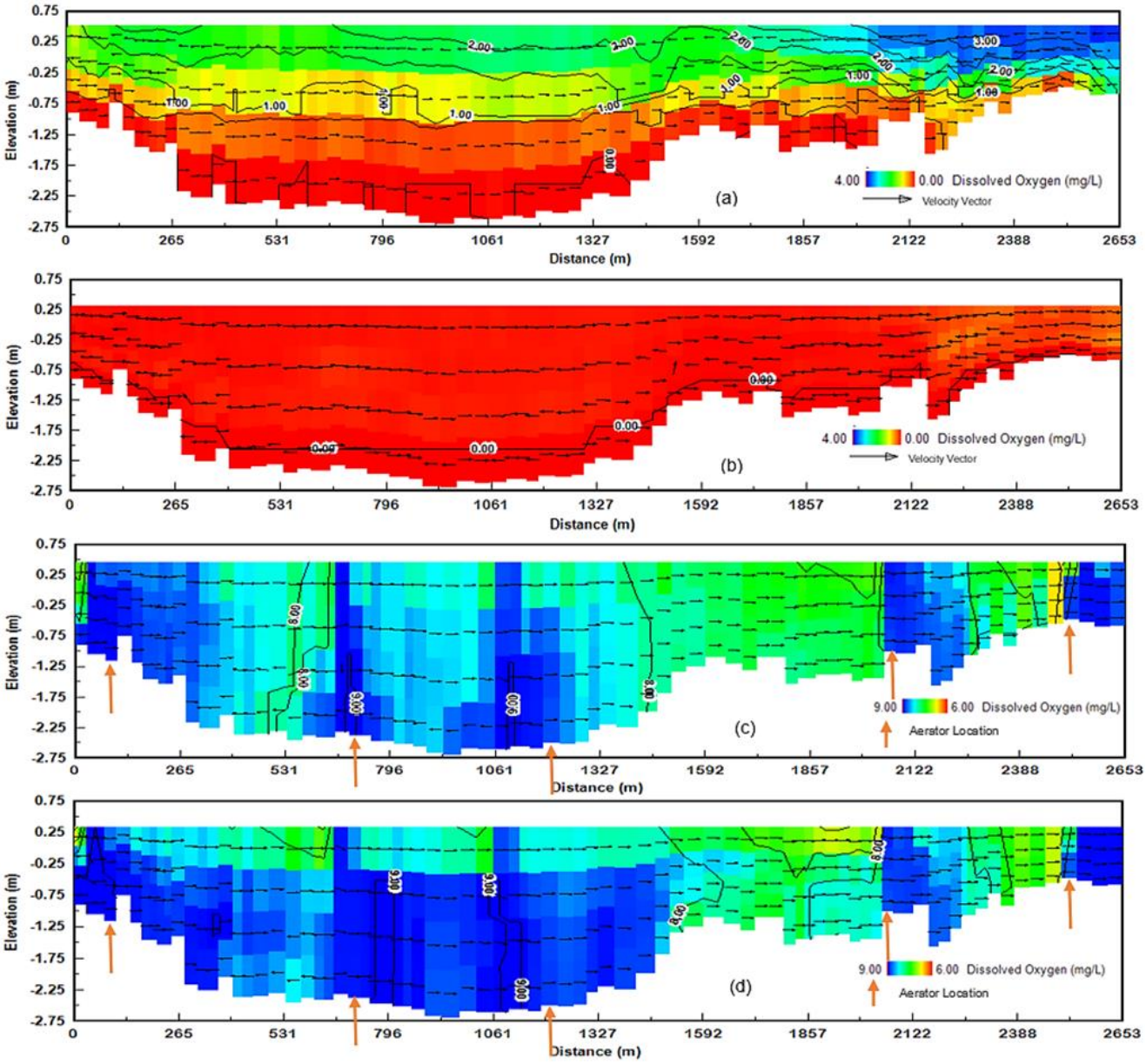

Figure 5-5 Longitudinal sections from the west part of Cotton Bayou to near Perdido Pass (section 1-1 in Figure 5-4(c)) showing EFDC simulated DO (mg/L) and velocity direction over depth at: a) 12:00 on 05/10/2023 b) 16:00 on 05/15/2023 c) 12:00 on 05/10/2023 with optimum setup of aerators, and d) 16:00 on 05/15/2023 with optimum setup of aerators.

Figure 5-5(a) shows strong DO stratification throughout the section. The west section has DO lower than 3mg/L whereas the surface DO is greater than 3 mg/L near GilChrist Island. The velocity vectors show that there is eastward flow from the mouth of Cotton Bayou to the shallow area at around 2100 m distance. . Flow is from west to east throughout the sections. The westward flow from the island area enters the section causing higher DO concentrations at the surface. Figure 5-5(b) shows complete anoxic conditions throughout the section on 5/15/2023 16:00. The velocity vectors show that at the top two layers the flow goes from the contracted section to GilChrist Island whereas the bottom two layers have opposite flow direction. The two flows coming from two different directions mix in the contracted area; which flow remains on top depends on the density of the water. Figure 5-5(c) and 5-5(d) show the longitudinal distribution of DO through section 1-1 after installation of aerators. The section goes through five aerator locations as presented in the figures. The figures show oxygenation of the bottom layers first; as air bubbles rise towards the surface, they become entrained based on the ambient water temperature. Figure 5-5(d) shows clear stratification up to 1592 distance. Since the aerators are placed at the sediment surface, the stratification has the opposite direction compared to the natural stratification of DO (Figure 5-5(a)).

Figure 5-6 shows the longitudinal distribution of DO along a section cut through section 2-2 in Figure 5-3(c). The section encompasses from north of Terry Cove through the shallow island regions towards the Old River channel. Figure 5-6(a) and 5-6(b) show spatial distribution of DO very clearly. The Terry Cove area has stronger stratification with lower DO concentrations. While moving from Island to deep (relatively) old River channel, DO increases sufficiently for *Gulf Menhaden* survival. The top three layers seem to be fully well-mixed whereas the bottom layer has slightly lower DO.

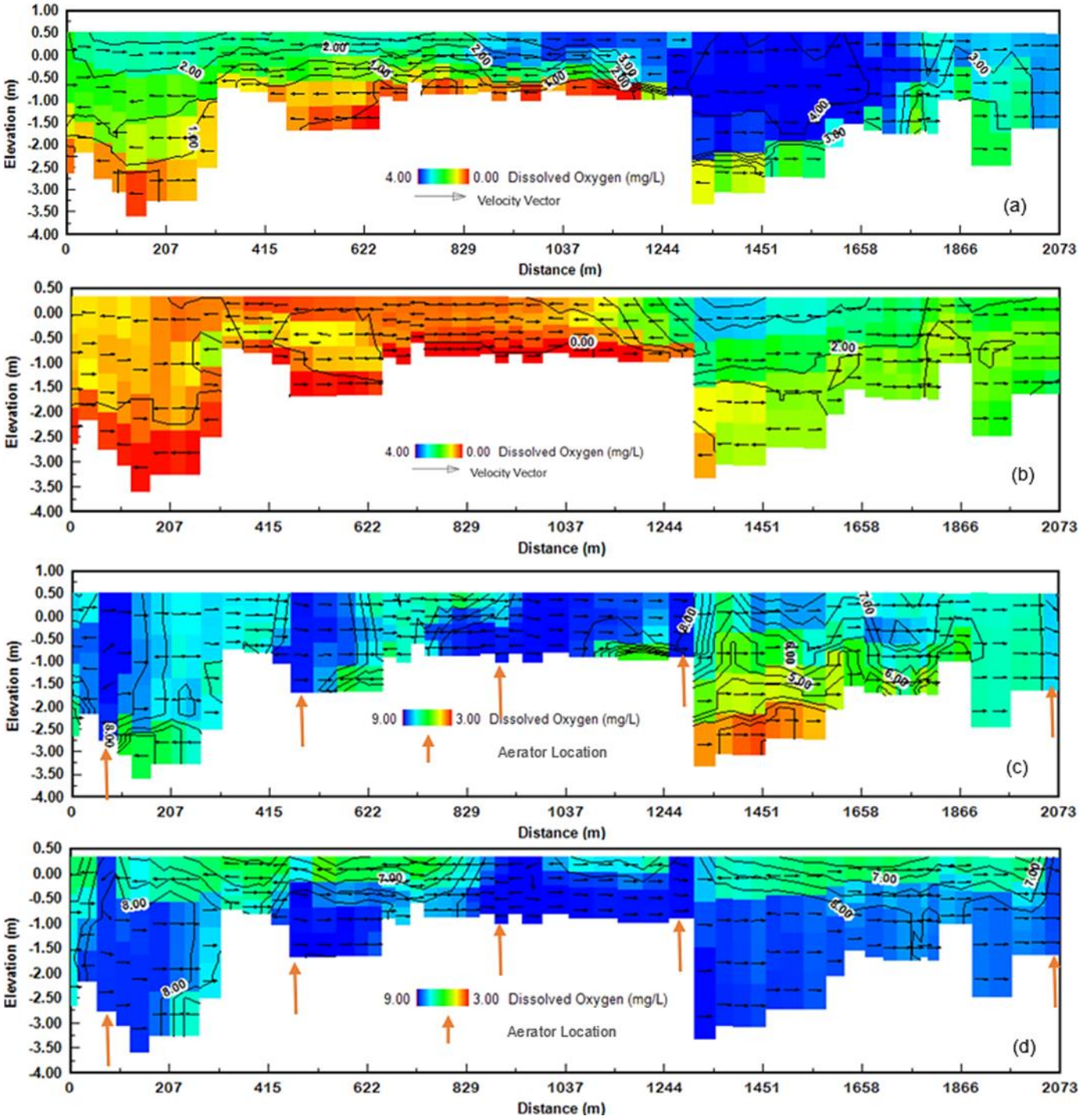

Figure 5-6 Longitudinal sections from the north part of Terry Cove to Old River (section 2-2 in Figure 5-4(c)) showing EFDC simulated DO (mg/L) and velocity direction over depth at: a)

12:00 on 05/10/2023 b) 16:00 on 05/15/2023 c) 12:00 on 05/10/2023 with optimum setup of aerators, and d) 16:00 on 05/15/2023 with optimum setup of aerators.

Figure 5-6(b) shows essentially well-mixed conditions, with anoxic conditions near the islands. In the shallow island region, velocity vectors also change direction. Figure 5-6(c) and 5-6(d) show longitudinal distribution of DO through section 1-1 after installation of aerators. The section goes through five aerator locations as presented in the figures. The figures show oxygenation of the bottom layers first; air bubbles rise towards the surface; they are entrained based on the ambient water temperature. Flow is from west to east throughout the sections. Figure 5-6(C) shows strong stratification south of the island areas; the surface DO becomes 7 mg/L whereas the bottom DO is close to 4 mg/L.

5.4.2 Open Boundary Conditions

The application of aerator can also be simulated using EFDC+ open boundary conditions. For this approach, it was assumed that the aerators have made the model cells saturated with DO. The cell where the aerator was placed, was used as an open boundary condition with constant temperature of 23^{o}C, constant salinity of 25 ppt and constant DO of 9 mg/L (close to the saturated DO at 23^{o}C). Higher DO was diffused from the open boundary to nearby cells based on simulated vertical and horizontal turbulent diffusion. Using the open boundary method, a few open boundary cells at mouth of Cotton Bayou, Perdido Pass and Old River were set as boundary cells for model stability. A total of 18 locations were selected for aerator placement (Figure 5-7(a)). At Cell1 and Cell2, the DO went below the target DO for few days but is unlikely to create stress on *Gulf Menhaden* since the DO again increased in 1-2 days. Moreover, the open boundary condition approach calculated lower DO than the jet/plume scenario since it did not consider any

additional flow caused by aerator bubbles. However, the Jet/Plume simulation method is closer to a realistic scenario as it calculates the flow inside the study area and transport of water quality constituents with the additional flow created by the aerators.

5.5 Pipe Connection from Gulf of Mexico

Another restoration method involves establishing a hydraulic connection between Cotton Bayou and Gulf of Mexico. The near-saturation DO of Gulf of Mexico can be transported to Cotton Bayou through a pipe. A pump can be used to transport the flow. The cell where the pipe would connect at Cotton Bayou was used as a flow boundary with constant flow of 3 m^3/s, constant temperature of 23ºC, constant salinity of 33 ppt and, constant DO of 8 mg/L. Figure 5-8(a) shows the location of the pipe connection. It was observed that this method did not increase DO concentration at Terry cove and near-island areas. DO concentration at Cotton Bayou increased but had DO less than the target DO for most of the time. Moreover, the flow 3 m^3/s corresponds to a 47,000 GPM pump capacity which is not feasible.

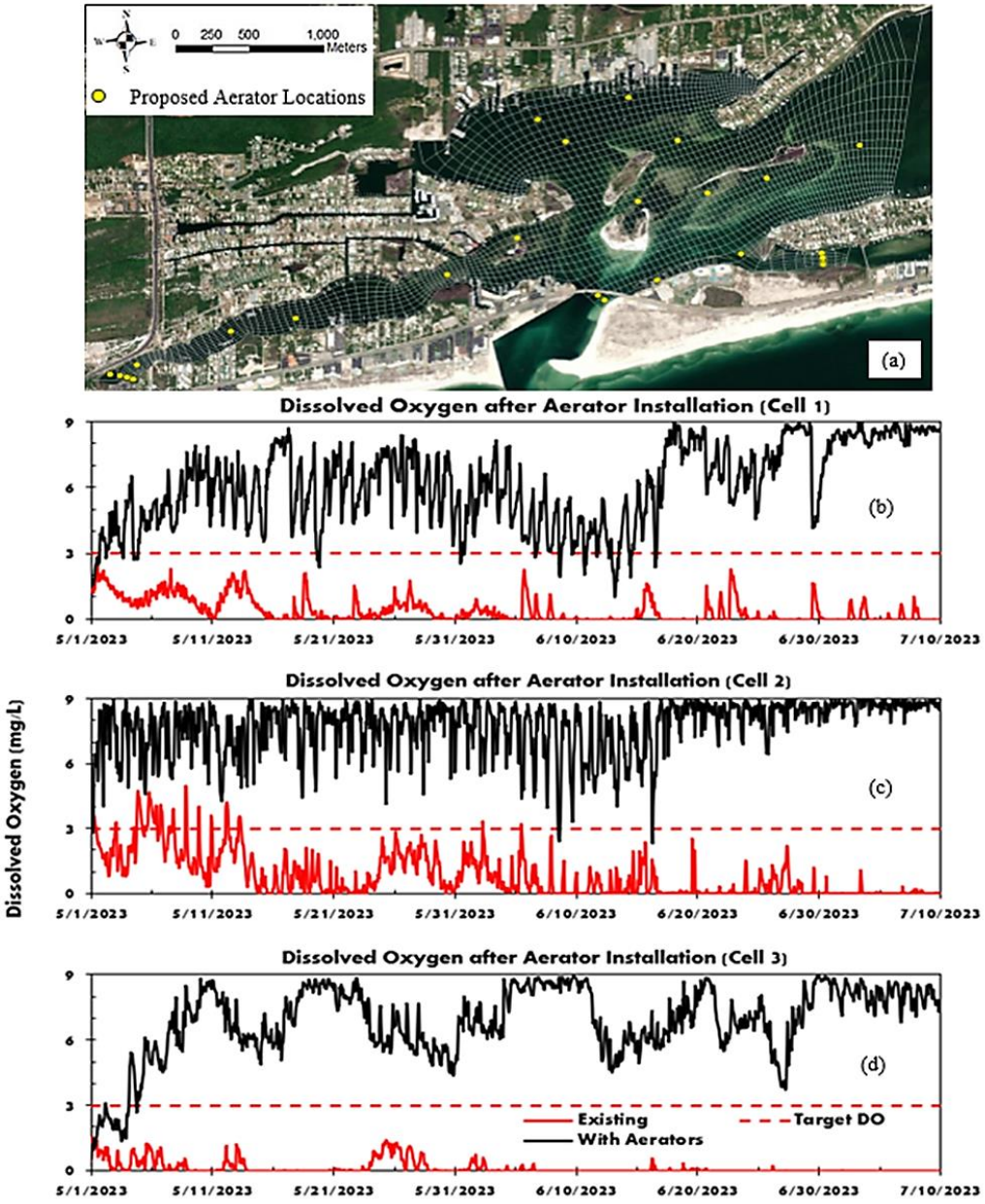

Figure 5-7 a) Location of aerator for optimum condition; (b), (c), and (d) DO concentration at selected cells (Figure 4-13) with optimum aerator setup using open boundary conditions compared with existing and target DO.

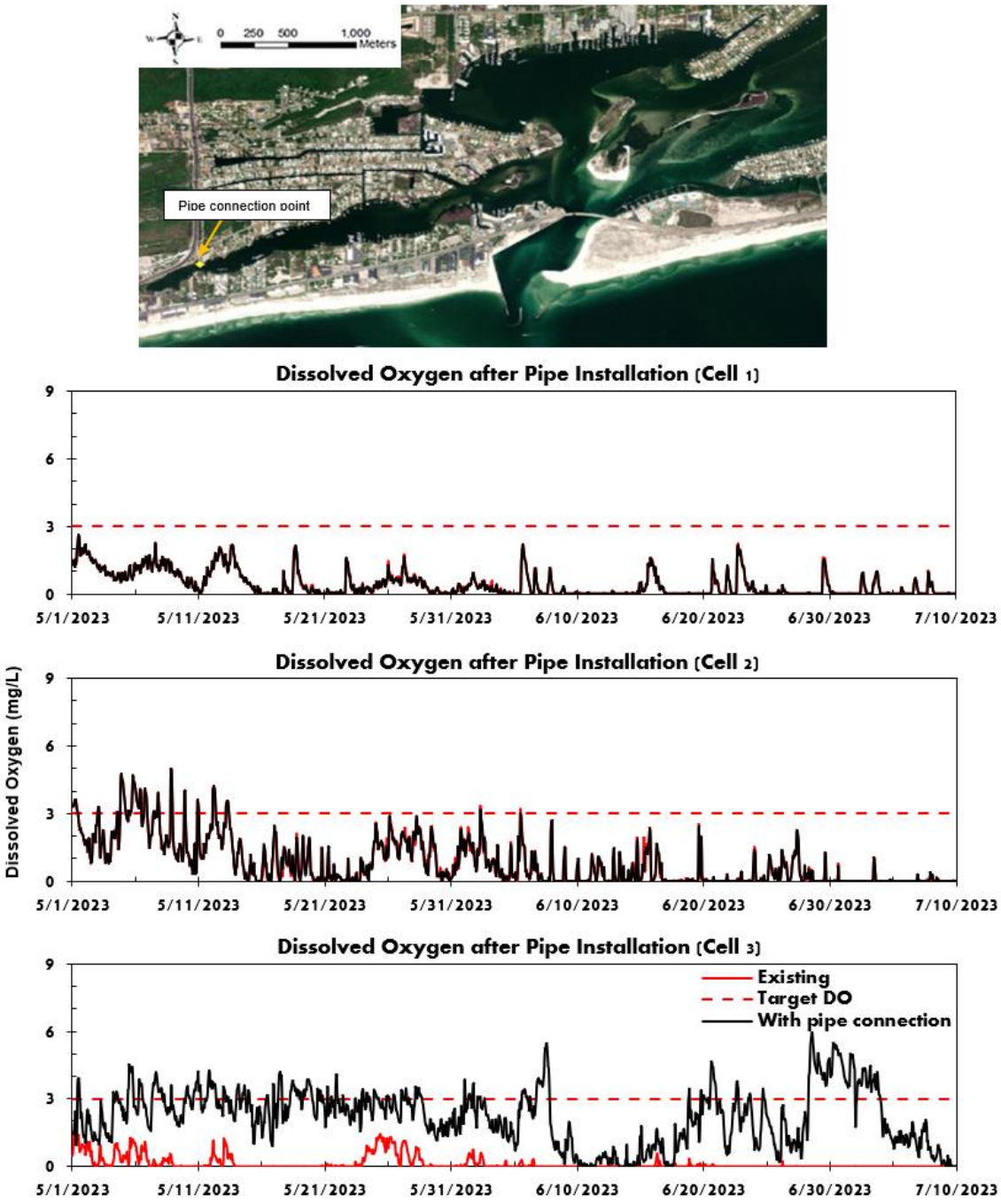

Figure 5-8 a) Location of the pipe connecting at Cotton Bayou from the Gulf of Mexico; (b), (c), and (d) DO concentration at selected cells (Figure 4-13) with pipe connection setup using flow boundary conditions compared with existing and target DO.

5.6 Dredging

Dredging is a potentially effective way to widen the channel and ensure flow exchange. The CBTC system has some shallow areas where sediment buildups happen. The sudden contracted channel at Cotton Bayou and the shallow areas between Walker Island and Robinson Island are among these areas. However, dredging is not possible near the islands as it may enhance erosion of these islands. The only channel where dredging is unlikely to negatively affect shoreline and island stability is in Figure 5-9(a). The bottom elevation of the adjacent area is 1.5 m. It is assumed that the channel is dredged to a target bottom elevation of 1.5 m. Figure 5-9 shows the difference in DO concentrations due to dredging alone. With the removal of sediment, the uptake of DO by nutrient-rich sediment decreases, which increases the DO concentrations at Cell 3. At Cell 2 and Cell 3, the DO concentrations increase as DO from Cotton Bayou circulates through the system. Dredging improves DO conditions by removing nutrient-rich sediment and ensuring enhanced water circulation through the dredged area.

Figure 5-10 shows the DO distribution and velocity direction at two transects (section 1-1 and section 2-2 in Figure 5-3(c)) on two different time. Figure 5-6(a) shows that the maximum DO on 5-10-2023 12:00 was 3 mg/L and the DO was stratified over the depth for existing condition. Figure 5-10(a) shows that dredging the narrow channel resulted in an increase in DO at the top layers, the maximum being 5 mg/L on 5-10-2023 12:00 but the bottom layer remained anoxic. Figure 5-10(b) shows that dredging the channel has resolved the anoxic DO problem on 5-15-2023 16:00 with maximum DO being 3 mg/L towards the east side. The DO distribution showed some stratification and the bottom layer remained anoxic. The DO distribution at the transect 2-2 for dredging scenario also showed some improvement in DO for both times. But the bottom DO near the islands remained below the target DO.

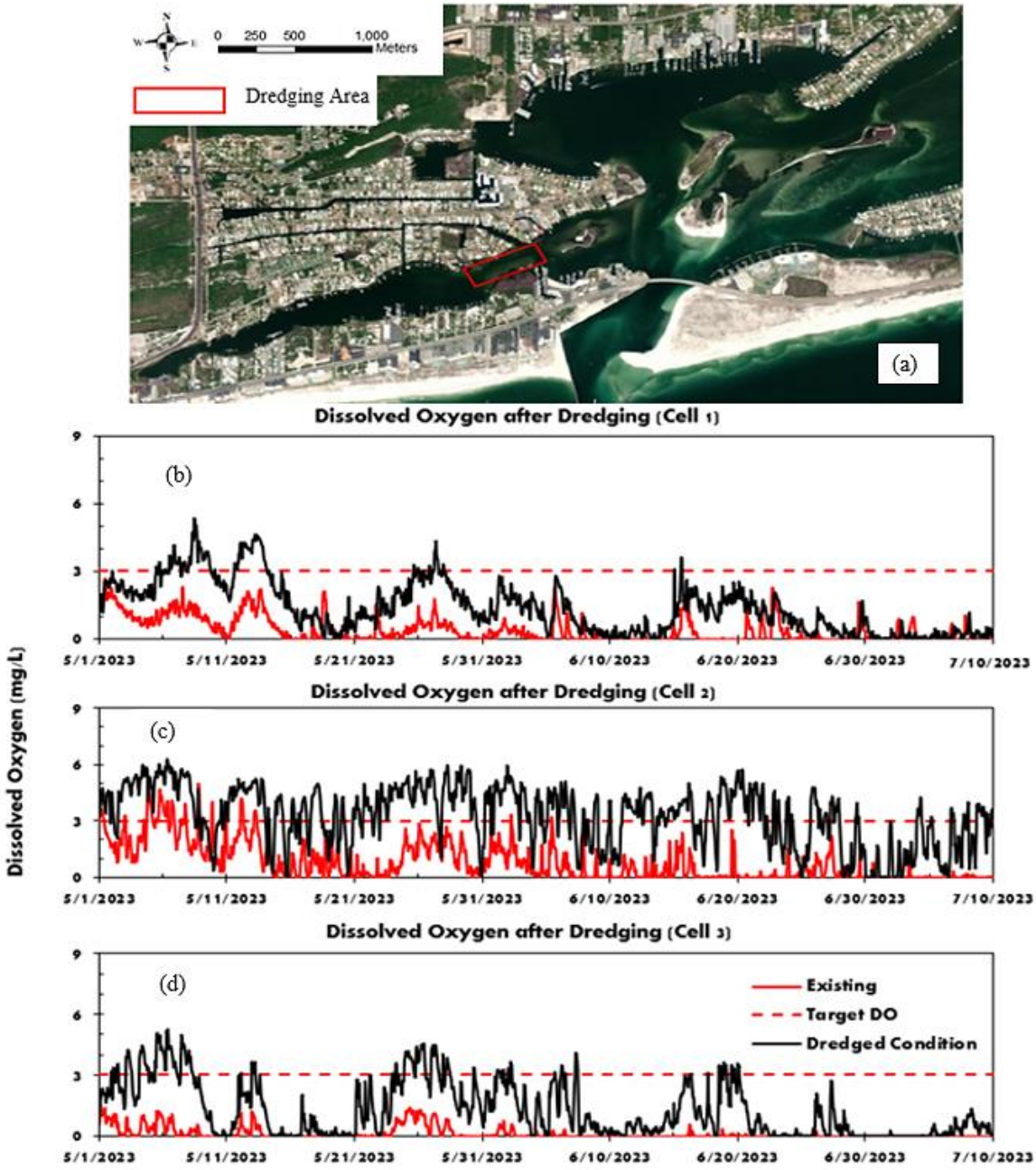

Figure 5-9 a) Locations of aerators for optimum condition; (b), (c), and (d) DO concentrations at selected cells (Figure 4-13) with optimum aerator setup using open boundary conditions compared with existing and target DO.

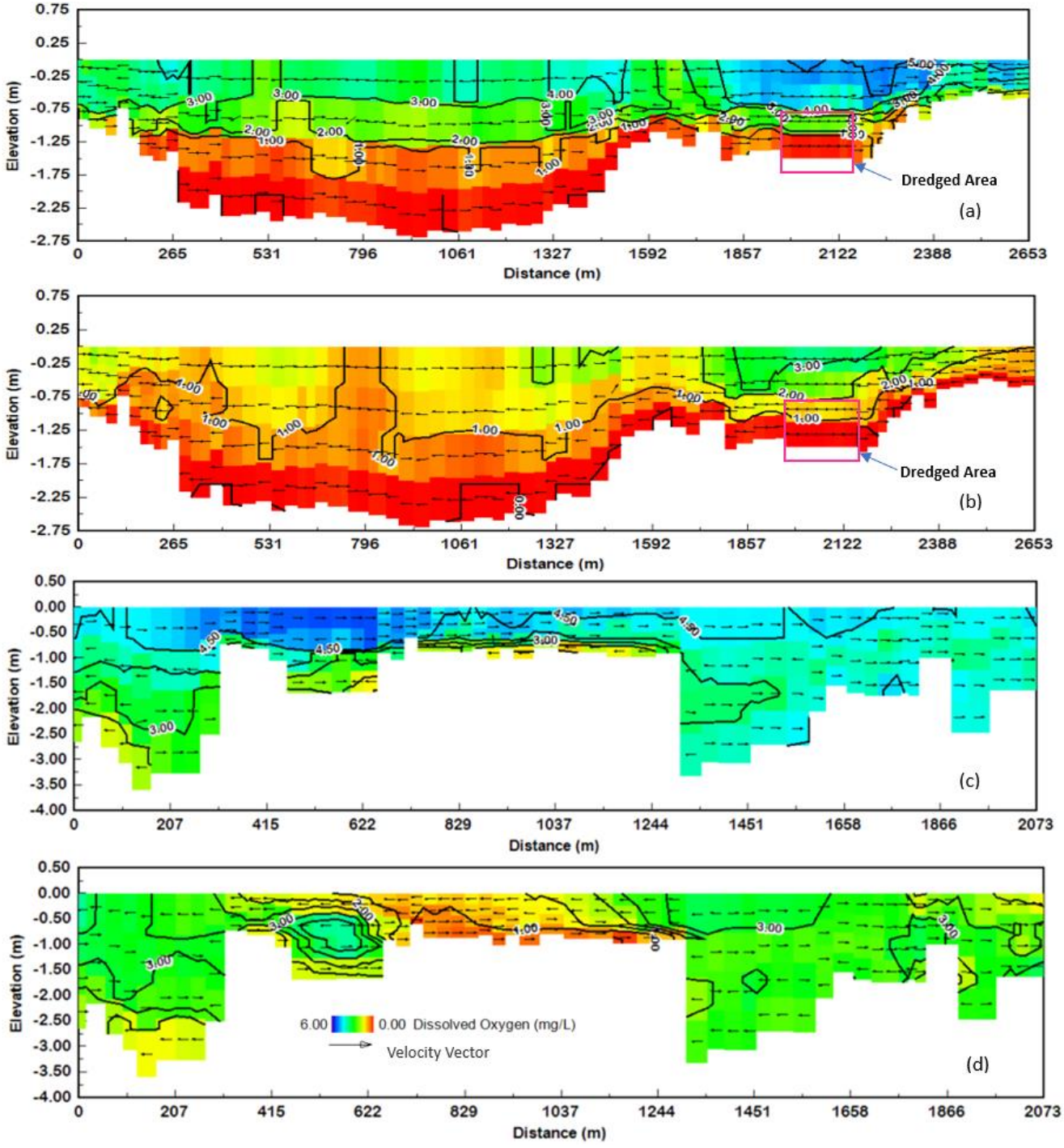

Figure 5-10 EFDC simulated DO (mg/L) and velocity direction over depth at longitudinal section at west part of Cotton Bayou to near Perdido Pass (section 1-1) on: a) 12:00 on 05/10/2023, b) 16:00 on 05/15/2023; at north part of Terry Cove to Old River (section 2-2) on:

c) 12:00 on 05/10/2023, and d) 16:00 on 05/15/2023 with proposed dredging scenario . Section 1-1 and section 2-2 are referenced in Figure 5-4(c).

5.7 Combination of Aerator and Dredging

The combination of aerator installation and dredging was also tested as a potential remedial alternative. In the dredged model, aerators were placed at potential locations. The same procedure is followed as Section 5.4.1. The jet/plume boundary condition is used. Due to dredging, the contracted channel can transport water more efficiently, increasing DO concentrations. As a result, less aerators are needed to oxygenate the area (Figure 5-11). With dredging, Cotton Bayou requires three aerators, Terry Cove requires four aerators, and Perdido Pass and Old River require one aerator each. The aerators at Perdido Pass (Aerator 9) and Old River (Aerator 6) are not crucial but ensure that DO remains above 3 mg/L at all times during the summer. If occasional low DO (not less than 1.5 mg/L, for 1-2 days for 5-6 instances) is not a concern, these two aerators can be omitted. Figure 5-12 shows the DO distribution and velocity direction at two transects (section 1-1 and section 2-2 in Figure 5-4(c)) at two different time. Transect 1-1 had three aerator locations (A1, A2, A3) and transect 2-2 also had three aerator locations (A4, A5, A6) placed close to the transect. At both transect locations at both times the DO ranged from 4 mg/L to 9 mg/L.

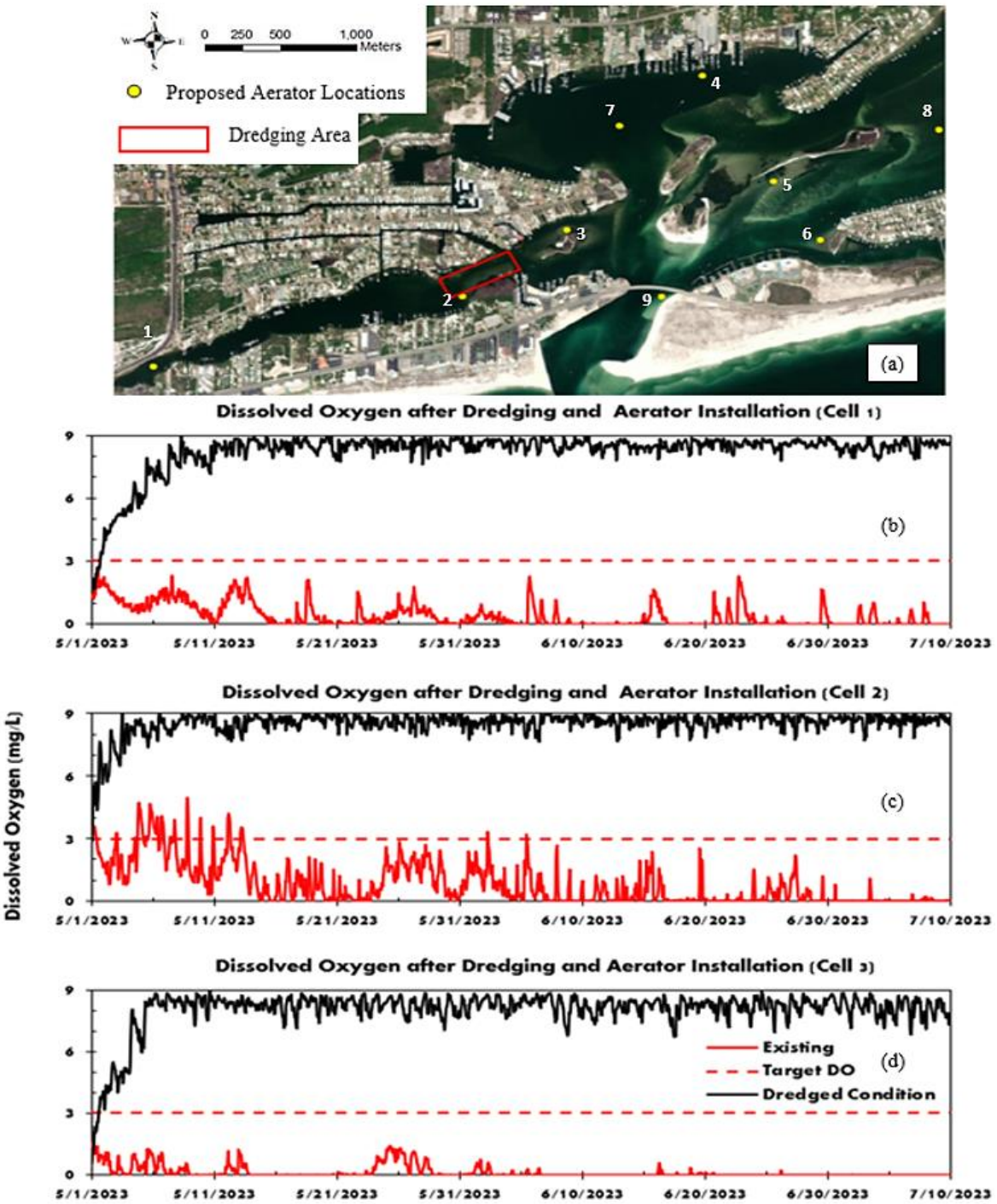

Figure 5-11 a) Location of aerator for optimum condition; b), c), d) DO concentration at selected cells (Figure 5-3) with optimum aerator setup using open boundary conditions compared with existing and target DO.

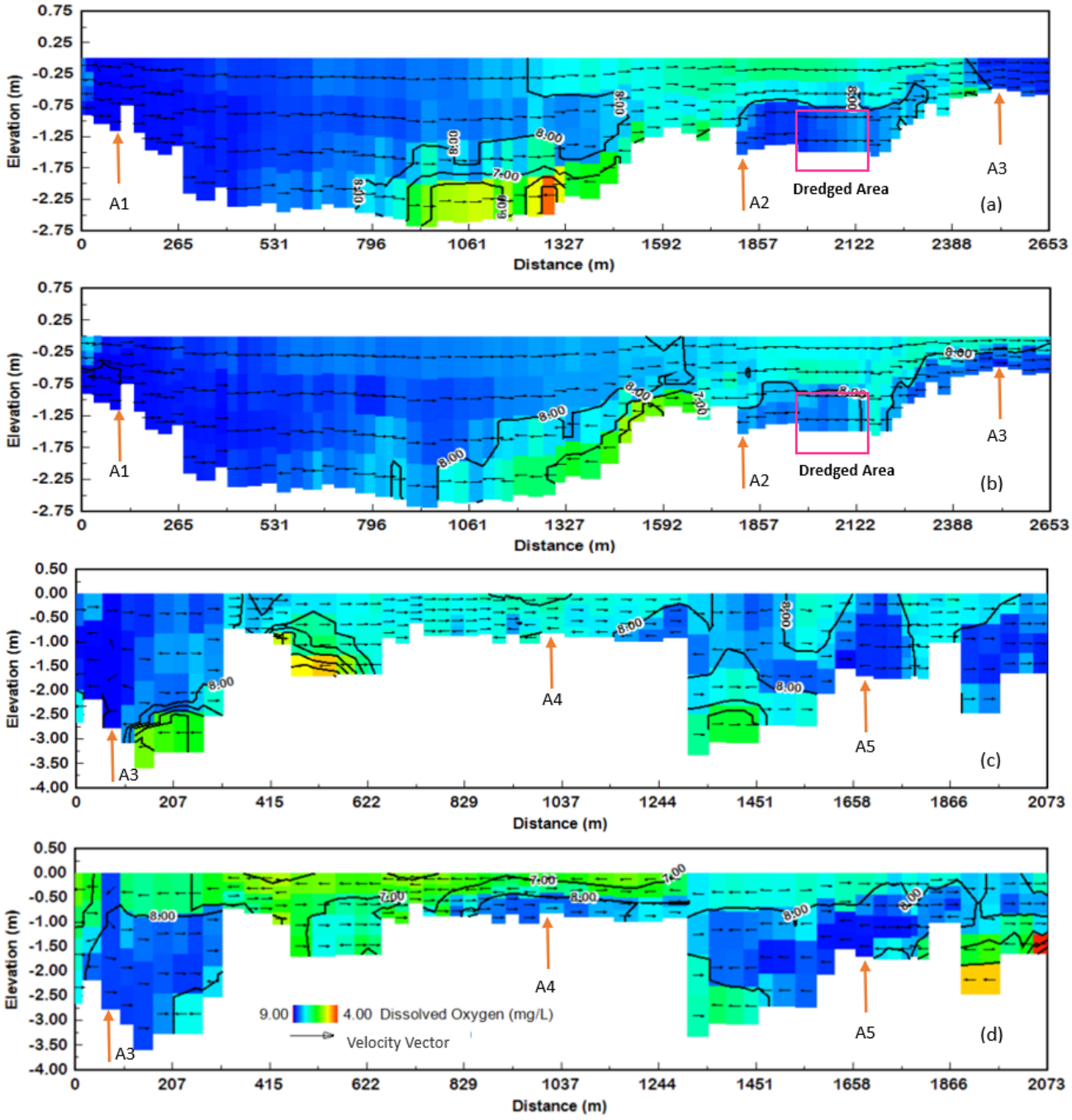

Figure 5-12 EFDC simulated DO (mg/L) and velocity direction over depth at longitudinal section at west part of Cotton Bayou to near Perdido Pass (section 1-1) on: a) 12:00 on 05/10/2023, b) 16:00 on 05/15/2023; at north part of Terry Cove to Old River (section 2-2) on:

c) 12:00 on 05/10/2023, and d) 16:00 on 05/15/2023 with proposed combination of dredging and aerators. Section 1-1 and section 2-2 are referenced in Figure 5-4(c).

5.8 Conclusion

This chapter demonstrates a novel approach for investigating and selecting remedial actions to improve water quality within estuaries. The EFDC+ model was used to test potential remedial options and select the most appropriate options for achieving remedial goals. In this case study, the primary remedial goal was to increase DO concentrations in chronically low DO areas to levels protective against fish kills, using Gulf Menhaden survival levels as the threshold DO to achieve. This case study demonstrates the effectiveness of using complex 3-dimensional hydrodynamic and water quality modeling to assist watershed managers and policy makers to make informed restoration decisions based on a technically-defensible assessment methodology.

- Four potential remedial approaches restoration methods were considered using an EFDC+ model for the CBTC system as a base model. Different functions/boundary conditions for the EFDC+ model were used to predict the effects of the remedial approaches on DO. Predicted DO were compared with observed DO and target DO. A target DO of 3 mg/L was set based on the habitat preference of *Gulf Menhaden.*

- Targeted placement of forced aeration systems was tested using two boundary condition options: Jet/Plume boundary condition and open boundary condition. Jet/Plume boundary condition was applied based on the specifications for an aerator commonly used in related applications (ADS FTC fine bubble aerators). Three configurations of aerator sets were compared in Figure 5-5. The aerator setup which met the target DO with a

minimum number of aerators was selected. A total of sixteen aerator sets were included in the optimum setup.

- Verification of the aerator model was performed by using open boundary conditions. For open boundary conditions, selected cells were set to maintain saturated DO conditions. Selected cells were in the same locations as the aerator sets. The model was modified to include additional boundary conditions for model stability. Simulated DO indicated that the optimum setup of aerator sets selected using the Jet/Plume boundary condition meets the target DO requirement. Additionally, the Jet/Plume boundary condition is a more realistic approach since it includes the additional flow exerted by air bubbles.

- Targeted dredging in strategically selected areas within the CBTC system improved water mixing and circulation. This approach was incorporated into the model by modifying the bottom elevation to mimic the effects of targeted dredging. Though dredging alone increased DO concentrations, it failed to meet the target DO requirement.

- Predictive modeling indicated that the most effective restoration method is a combination of dredging and aeration. When the minimally dredged channel in Cotton Bayou was incorporated into the Jet/Plume boundary condition aerator model, a total of nine aerator sets were required to achieve the target DO.

Chapter 6 Extreme Weather and Sea Level Rise Effect on Perdido Bay

6.1 Introduction

Coastal habitats are vulnerable to environmental change, including projected changes in tropical cyclones and sea level rise. Extreme weather events are expected to significantly increase by 2050 (Arkema et al., 2013), and tropical cyclones cause the most destruction of any natural disaster in the U.S. (Emanuel, 2005). Increased sea level can alter land cover, increase erosion, and expose more areas to flooding and inundation (Epanchin-Niell, 2017). It has been estimated through modeling that up to 17,000 km^2 of beach worldwide could be lost by 2100 (Hinkel et al., 2013). The estimate for global mean sea-level rise by the year 2100 is up to 0.91 m (Epanchin-Niell, 2017) which may increase the exposure of people and properties by 30–60% (Arkema et al., 2013). In the northern Gulf of Mexico, local sea-level rise projections can be up to 2.48 m by the year 2100 according to the National Oceanic and Atmospheric Administration's (NOAA) Sea Level Rise Viewer (Sweet et al., 2017). Perdido Bay is included in the Eastern Gulf region (Figure 6-1), which has a high risk of sea level rise, according to NOAA 2022 predictions (Sweet et al., 2022).

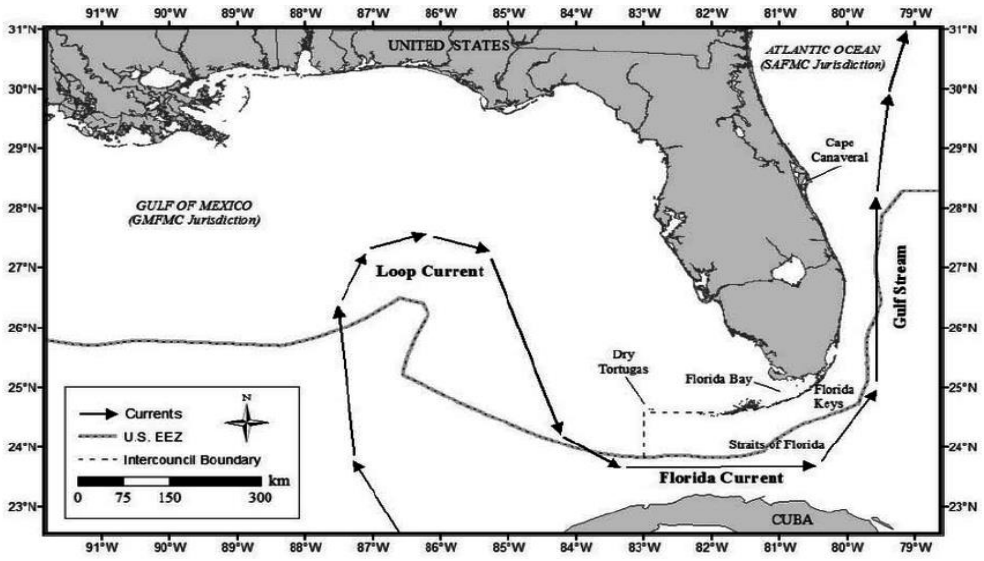

Figure 6-1 Location of Eastern Gulf

Climate change poses a risk to water quality in estuaries. Some climate change-related stressors include warmer summers and winters; increasing indices and durations of droughts; increasing frequency and intensity of tropical weather events, and rising sea levels. Increasing ocean heat content is a consequence of global warming, which becomes a major factor in mean sea level rise through thermal expansion of sea water. Potential future climate conditions has been assessed by the Intergovernmental Panel on Climate Change (IPCC). The IPCC Assessment Report 5 and Coupled Model Intercomparison Project (CMIP5) Datasets prepared in 2014 contains observed and predicted climate data from 2006 to 2300. Earth System Model (ESM) is often used as a synonym for coupled climate models. ESM models represent the dynamics of carbon and non-CO_2 greenhouse gas emissions.

To understand the potential impact of global warming and sea level rise on the CBTC system, the EFDC+ model developed in Chapters 4 and 5 was used to simulate baseline (no restoration) and improved (with preferred remedial actions) conditions in 2050, using CMIP5 data. The existing condition (calibrated model in Chapter 4) and the proposed condition

(proposed model with optimum remedial alternatives, Chapter 5) was simulated using future climate scenarios to examine the performance of the remedial alternatives under future climate conditions and sea level rise.

6.2 Methods

6.2.1 Sea Level Rise

It is critical to assess water levels in coastal areas in the context of sea level rise due to climate change. Future estimates for global mean sea level rise are relative to the current elevation of global mean sea level. Present mean sea level (MSL) for US coasts is determined from long-term NOAA tide gauge records and is referenced to the current National Tidal Datum Epoch (NTDE) provided by NOAA.

In recent decades, the dominant contributors to global sea level rise have been ocean warming and ice sheet loss (Mengel et al., 2016; Neill & Lee, 2020). Several previous studies, including the Intergovernmental Panel on Climate Change (IPCC), assumed thermal expansion of the oceans and retreating glaciers to be the dominant contributor. However, the National Research Council (NRC) reported that advances in satellite measurements indicated ice sheet loss as a greater contribution to global sea level rise than thermal expansion over the period of 1993 to 2008. There are six scenarios (low, intermediate-low, intermediate, intermediate-high, high and extreme) that reflect different degrees of ocean warming and ice sheet loss.(Sweet et al., 2022)

Parris et al. (2012) used equation 6.1 and equation 6.2 to estimate global sea level rise. NOAA currently utilizes the 1983–2001 National Tidal Datum Epoch. As the mid-point for the NTDE, 1992 is often selected as the start-point for sea level rise scenarios. Parris et al (2012)

reported four scenarios of sea level rise : lowest, intermediate-low, intermediate high and highest scenarios. The highest, intermediate-high, and intermediate-low scenarios represent possible future accelerations in global mean sea level rise and the future global mean sea level rise (using 1992 as the mid-point of NTDE) is represented by the following quadratic equation:

$$E(t) = 0.0017t + bt^2 \quad (6.1)$$

in which *t* represents years, starting in 1992, *b* is a constant, and *E(t)* is the estimated sea level rise, in meters, as a function of time *t* in year. To fit the curves to the scenarios, the constant *b* has a value of 1.56E-04 (the highest scenario), 8.71E-05 (the intermediate-high scenario), and 2.71E-05 (the intermediate-low scenario).

If estimating a projected rise in global mean sea level starts in a year more recent than 1992, the sea level rise is calculated using the following equation:

$$E(t_2) - E(t_1) = 0.0017(t_2 - t_1) + b(t_2^2 - t_1^2) \quad (6.2)$$

Where t_1 is the time between the beginning year of interest and 1992 and t_2 is the time between the ending year of interest and 1992 (Knuuti 2002, Flick et al. 2012).

The above-mentioned equations determined the global mean sea level rise. In the eastern Gulf of Mexico, according to Sweet et al. (2022) predictions for 2050, the low, intermediate-low, intermediate, intermediate-high, and high tide conditions have sea level rise of 0.30, 0.34, 0.38, 0.45 and 0.51 m, respectively relative to sea level in 2000. Assuming the intermediate-high or high scenario are the most probable for the northern Gulf of Mexico, a scenario of 0.51 m (high scenario) rise in sea level relative to the sea level in 2000 was used in this study.

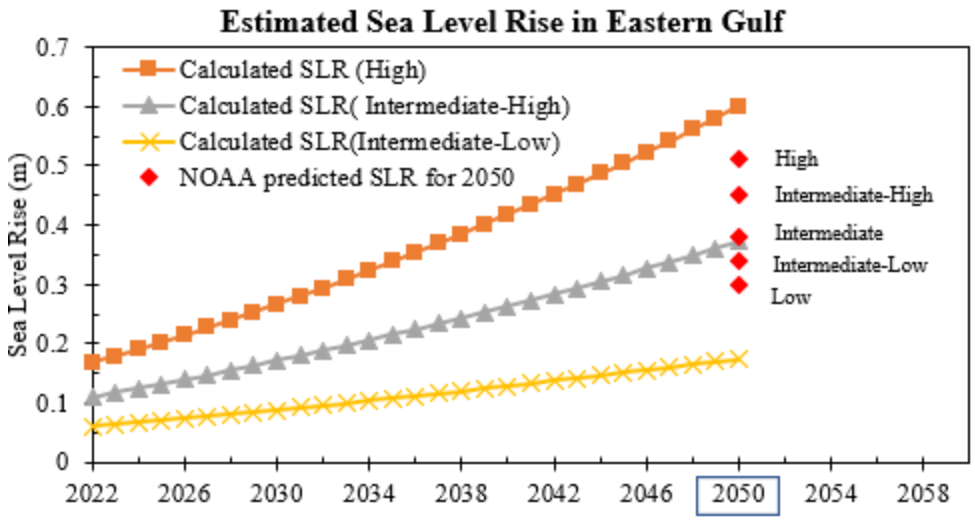

Figure 6-2 Estimated global sea level rise (Parris et al, 2012) and eastern Gulf of Mexico sea level rise (Sweet et al., 2022). Calculated SLR represent calculated global sea level rise using equations from Parris et al. (2012).

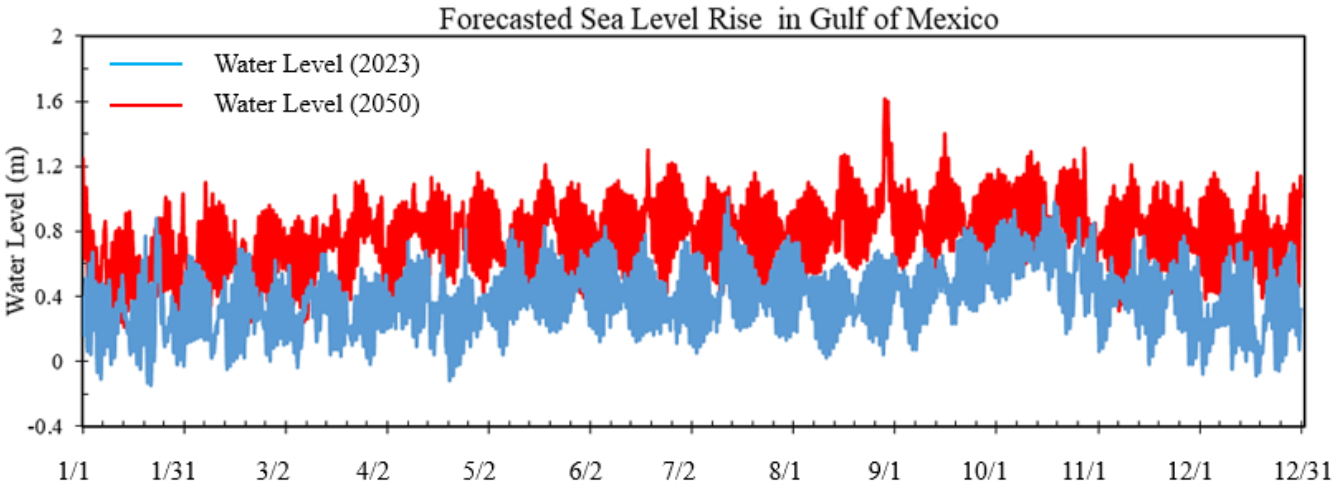

Figure 6-3 Water level at Dolphin Pass in 2023 and in 2050 (based on high scenario for the eastern Gulf of Mexico).

6.2.2 Future Weather Conditions

The establishment of long-term mitigation goals against climate change should be based on sound information from scientific projections on a centennial time scale. “MIROC-ESM”, is

based on the global climate model MIROC (Model for Interdisciplinary Research on Climate) which has been cooperatively developed by the University of Tokyo, NIES, and JAMSTEC ((Nozawa et al., 2007; K-1 model developers, 2004). Representative Concentration Pathway (RCP) is a greenhouse gas concentration trajectory adopted by IPCC. RCP 6.0 is a high greenhouse gas emission scenario. To examine hydrodynamics and water quality changes in CBTC due to future climate, the MIROC ESM RCP 6.0 dataset for 2050 was used. The MIROC ESM RCP 6.0 dataset was downloaded from the WDC Climate database (https://www.wdc-climate.de/ui/) and data were extracted for our study region in the year 2050. Daily projected weather data and wind data were arranged in EFDC+ input format and used in the calibrated EFDC+ existing (baseline) condition model and proposed condition model (optimized aerator number and locations with targeted dredging).

EFDC+ atmospheric forcing input variables include nine meteorological parameters: atmospheric pressure (millibars), air temperature (^{o}C), relative humidity (fraction), rainfall(m/day), evaporation (m/day), solar radiation (W/m^2), cloud cover (fraction), wind speed (m/s) and wind direction (degree). The existing condition model for 2023 uses meteorological data collected from the Mobile Regional Airport (40 miles northwest of the Wolf Bay) and the South Alabama Mesonet Jay Station (25 miles northeast of the Wolf Bay). The Mobile Regional Airport monitoring station records all required meteorological parameters except solar radiation, and the Mesonet Jay Station records all parameters except atmospheric pressure and cloud cover. Meteorological data requirements were met by combined data from these two stations in the EFDC+ model. Figure 6-4 shows the comparison between existing weather condition and future weather conditions which is based on MIROC ESM RCP 6.0. It was identified that the air temperature

rises 6ºC on average from 1/1/2050 to 7/31/2023. The relative humidity decreases in 2050 and the solar radiation shows less fluctuation over time.

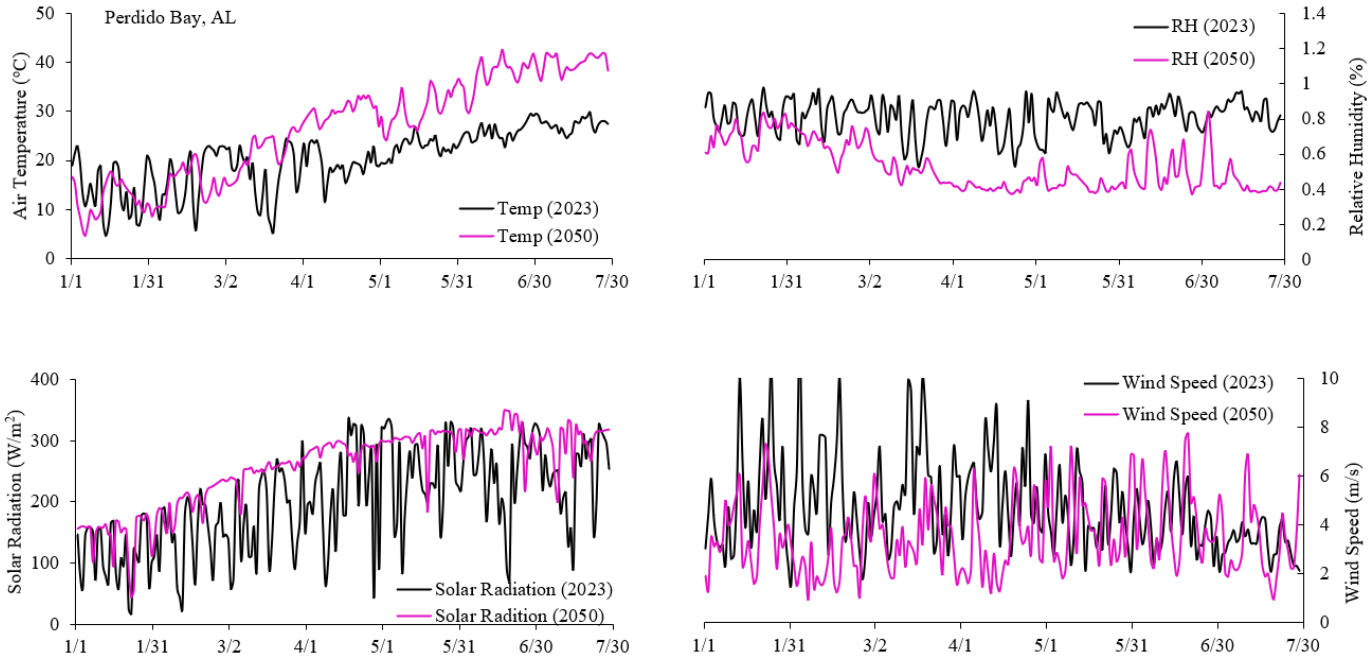

Figure 6-4 Comparison between existing and future (MIROC ESM RCP 6.0) weather conditions

6.3 Result

6.3.1 Future Climate Scenario Results

Figure 6-5 shows simulated DO concentrations with future climate along with the dredged/aerator scenario with future climate. DO concentrations for future climate are higher than those for existing (current) climate in early May; this is likely due to the sudden drop in air temperature. The DO concentrations on future climate show a different anoxic period than that for the existing (current) climate. The proposed dredged/aerator scenario results in different DO concentrations under future climate conditions; with decreased DO due to high air temperatures. For cell 1 and cell 2 (Figure 4-14), the DO simulation for future climate proposed condition

drops below 3 mg/L in June. Though Cell 3 DO for future climate proposed condition is less than the proposed condition DO, it is above the target DO of 3 mg/L.

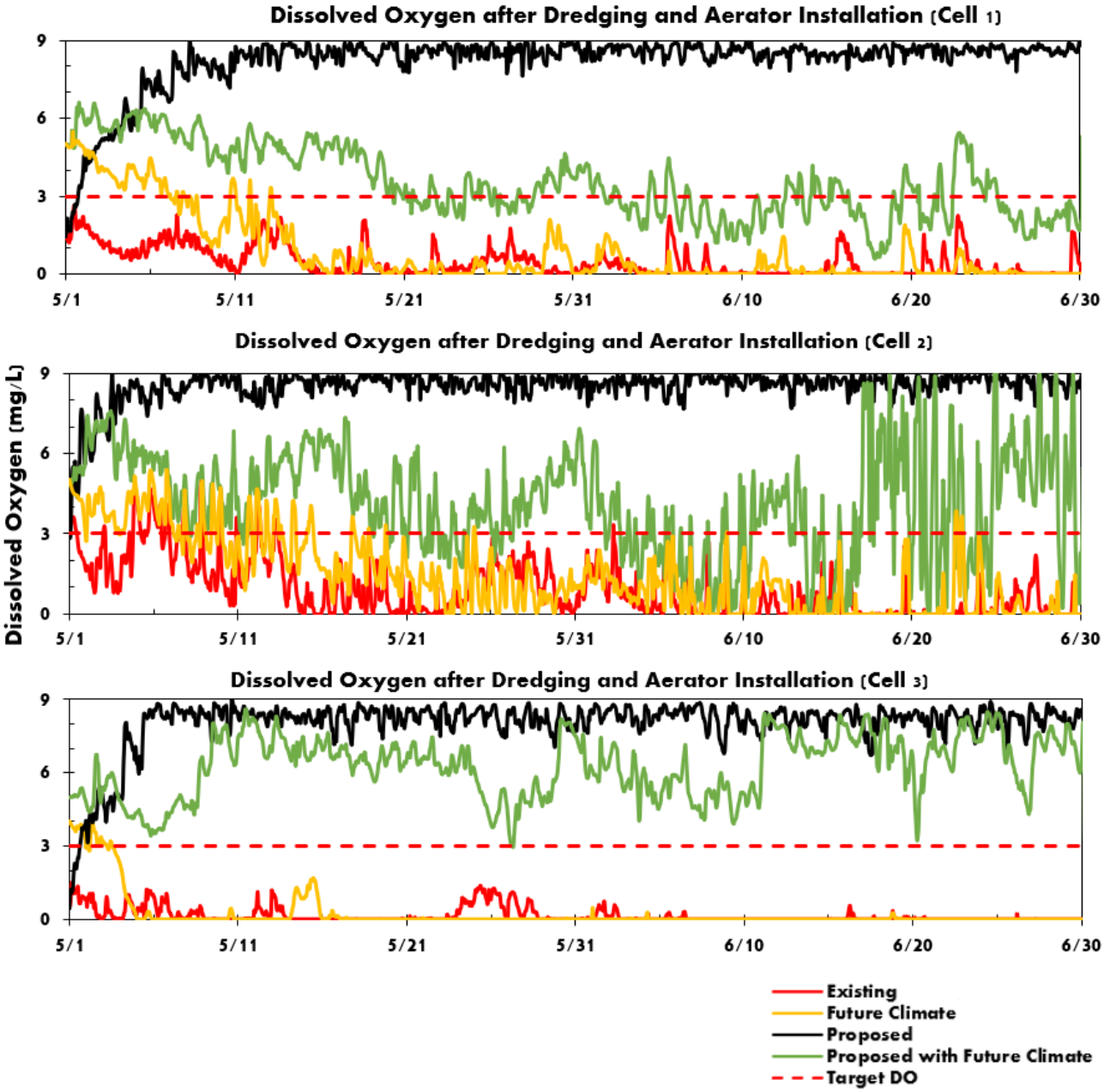

Figure 6-5 Effect of future climate on bottom DO concentrations.

6.3.2 Sea Level Rise Scenario Results

Figure 6-6 shows the change in DO if sea level rises. DO concentrations increase with sea level rise. DO concentrations with sea level rise are greater than the target DO, so no aerator or dredging is required. When dredging and aerator are incorporated in the sea level rise scenario, the effect on DO is negligible.

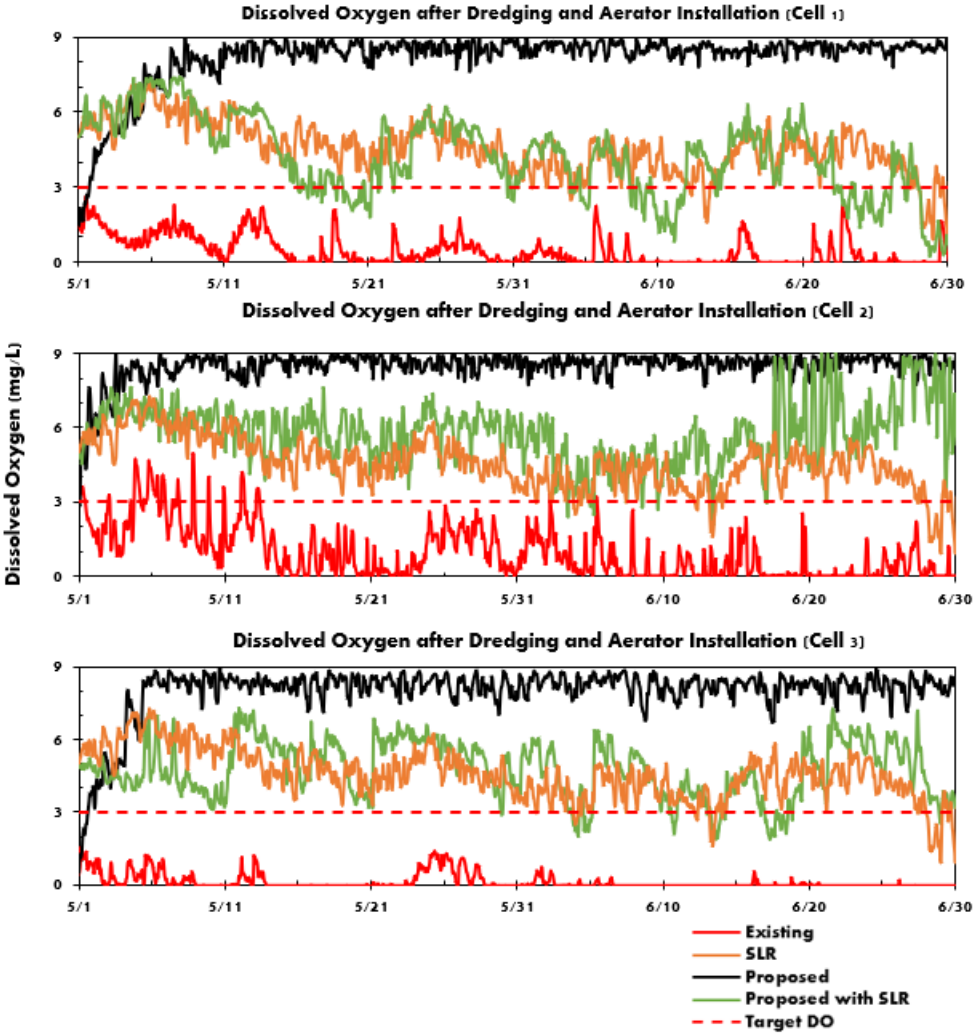

Figure 6-6 Effect of Sea level rise (SLR) on bottom DO concentrations.

6.4 Conclusion

A sea level rise of 0.51 m was implemented through the Gulf of Mexico water level boundary condition. MIROC ESM RCP6.0 was selected as the future climate model for its complete consideration of different environmental stressors. Future climate data were extracted at the center of the CBTC system for 2050.

- Sea level rise results in higher DO in the three observation cells (Figure 5-3) for most of the summer. It was also observed that in the event of sea level rise, incorporation of aerators and dredging have minimal impact on DO.
- The future climate scenario shows a much warmer climate in 2050. As a result, the DO concentrations drop below the target DO on some days in June even with the dredging-aerator scenario applied.

Chapter 7 Summary and Conclusions

7.1 Summary

The research work presented in Chapter 2 through Chapter 6 can be divided into two parts: lake water quality modeling and estuary water quality modeling. The lake water quality modeling includes Chapter 2 and Chapter 3. In Chapter 2, the lake water quality model MINLAKE2020 was first discussed along with its integration of nutrients and DO sub models. The updated model MINLAKE2020 was calibrated against measured water temperatures and DO profiles for six Minnesota lakes with varying characteristics in terms of depth (two shallow lakes, two medium-depth lakes, two deep lakes) and trophic status (two eutrophic, two mesotrophic, and two oligotrophic lakes). Later in Section 2.6, the inflow-outflow sub model was explained, and the simulation results were presented in Section 2.7. Although the 1-D MINLAKE2020 has provided acceptable results, the MINLAKE2020 model was also compared with the 3-D EFDC+ for several factors including spatial variance, simulation time, and long-period simulation. This study is particularly important for lake managers and water quality modelers since it gives an overall assessment of model performance based on lake features (region, size and other characteristics).

Chapter 4 through Chapter 6 describes estuary water quality modeling. The overall goal of these chapters is to demonstrate the effectiveness of 3-D hydrodynamic and water quality modeling as a means of testing the performance of proposed remedial strategies and selecting the most appropriate remedial approach. To demonstrate this approach, a case study was examined in the CBTC area of Perdido Bay on the northern Gulf coast. Chapter 4 focuses on the setup and calibration of a 3-D hydrodynamic and water quality model (EFDC+) for the CBTC system. For complete incorporation of the inflow and open boundaries, a coarse grid EFDC+ model for

Perdido Bay-Wolf Bay was developed first. Then, a more refined grid, nested model was developed which extracted boundary conditions from the coarse grid Perdido Bay model. The model was calibrated using observed data collected at three locations of CBTC system using continuous monitoring probes, recording at two-hour intervals. The objective for model calibration was to match the low DO occurrence in the seasonal summer period. The model was calibrated in two segments: spring (November to February) and summer (May to July). The coarse grid model was calibrated first. Water level, water temperature, salinity and DO were compared with observed data. To achieve optimal matching with the observed data, a more refined nested model was developed and incorporated into the coarse grid model.

Chapter 5 focuses on predicting water quality changes resulting from the testing and selection of remedial alternatives, using the calibrated model developed in Chapter 4. Through modeling and observed data, it was seen that the bottom layers in the three observation points have extremely low DO the seasonal summer. The prominent fish species in CBTC system often involved in fish kills, *Gulf Menhaden*, requires DO above 3 mg/L for survival. To provide the study area with a minimum DO of 3 mg/L, three restoration methods were examined: aeration, dredging, and a combination of both. Testing the restoration method using 3-D modeling is an innovative approach to identify the optimal restoration approach with minimal expenditure of time and funds. To test aeration, two methods were considered: jet/plume boundary conditions and open boundary conditions. Based on flow directions and DO distributions, three different setups for aerators were tested. Figure 5-5 shows the DO concentration after using the aerators at three setups. Comparing the DO concentrations, the optimum setup of aerators were selected. This setup has 5 aerator locations along the Cotton Bayou, four locations along the upper Terry Cove, 6 locations near the islands and surrounding east areas, and one location along the Old

River Channel. The intent was to test the same setup using an open boundary condition option in EFDC for verification. Since the boundary conditions work differently, three extra cells (the end of Cotton Bayou, Old River and Perdido Pass) were assigned the aerator DO for the model to run properly. Moreover, four aerators were assigned instead of six in the island region because that was the optimum amount for target DO. Dredging the Cotton Bayou channel was also tested. Though it helped in circulation and got rid of the sediment, the DO concentration was not more than 3 mg/L on most of the summer days in Cell 1 and Cell 2. At the end, a combination of dredging and aerators were utilized which gave us the best result. The optimum setup now has the cotton bayou channel dredged and a total of nine aerator locations.

Chapter 6 deals with the climate change effects on the CBTC water quality with and without the restoration technique. A sea level rise of 0.51 m was implemented through the Gulf of Mexico water level boundary condition. The sea level rise results in higher DO in the three observation cells (Figure 4-13) for most of the summer. It was also observed that in the event of sea level rise, the aerator and dredging condition does not have significant impact on DO, increasing the DO by a low margin on some days. MIROC ESM RCP 6.0 scenario data were used for future climate projections in 2050.

7.2 Conclusion

In Chapter 2, the updated model MINLAKE2020 was calibrated against measured water temperature and DO profiles for six Minnesota lakes with varying characteristics in terms of depth (two shallow lakes, two medium-depth lakes, two deep lakes) and trophic status (two eutrophic, two mesotrophic, and two oligotrophic lakes). The average standard error of water temperature and DO are 1.51^{o}C and 2.33 mg/L, respectively. One major advantage of this model over MINLAKE2012 is that this new model has decreased average standard error of DO

simulation by 24.2%. A long-term simulation of Lake Elmo (1989 to 2009) revealed that the anoxic condition at the lake bottom regulates sediment oxygen release, which in turn influences the surface phosphorus in Lake Elmo. The results from MINLAKE2022 was analyzed in detail and it was found that the density difference between the inflow water and lake water plays an important role in inflow mixing. The nutrient entering through the inflow greatly affect nutrient and Chl-*a* concentration in the lake.

The study showed that EFDC+ performed better in simulating DO in Lake Carlos and Lake Pearl for the summer period. The winter DO could not be compared because no observed data was available. However, the snowfall data (close to the lake location) was used as an estimation of ice in and ice out dates. It was observed that EFDC+ simulated shorter ice cover periods and smaller ice thicknesses due to not simulating snow thickness. Though EFDC+ provides great advantage by simulating spatial variance- a great feature for large lakes with complex bathymetry, multiple inlet/outlet; MINLAKE is preferable tool for simulating lakes for multiple years due to its less computation time.

Chapter 4 includes the model development and calibration of CBTC system. From the DO data, it was observed that the CBTC area has lethal DO (less than 3 mg/L) for *Gulf Menhaden* on most of the days in the Summer. The simulation results indicated that Cotton Bayou has lower DO in Summer compared to Terry Cove and Perdido Pass. Due to its location and bathymetry, Cotton Bayou has the highest stratification and longest anoxic period in Summer. Terry Cove also experienced stratification and anoxic condition. The near-island shallow areas between Terry cove and Perdido Pass are very shallow and remain more or less well mixed most of the Summer days. During calibration efforts, it was observed that SOD and COD play a very important role in DO calculation. Two major advantages of EFDC+ are the application of nested model and sediment

diagenesis model. The nested model of CBTC system performed better than the coarse model; this statement is based on the comparison with observed data. It was observed that the nested model simulates water level, water temperature and DO with good agreement with observed data. For Summer period, the RMSE for Terry Cove, Perdido Pass and Cotton Bayou DO (simulated using nested model) were 1.50, 1.21 and 1.09 mg/L, respectively. Figure 4-13 shows the difference in simulated DO for coarse and nested model. It is evident that the nested model performs better in simulating DO at all three locations. The smaller cell size helps the model to capture the hydrodynamic and water quality changes more easily. The overall RMSE for DO simulation reduced by 27% when the nested model was used. To capture the spatial variance, the sediment diagenesis model was used. The model area was divided into three areas with different COD rates. This option allows the user to calibrate DO more efficiently as shown in Figure 4-7.

Chapter 5 shows a unique approach to solve the low DO issue at CBTC area. The Jet/Plume boundary condition and the open boundary condition were used to include aerators in the CBTC system. Similar results in Figure 5-4 and 5-5 show that our approach to aerator simulation is giving reasonable results. The goal was to select an optimum scenario where we would use the least number of aerators to keep the DO above 3 mg/L so that *Gulf Menhaden* does not undergo any stress. The combination of dredging and aerator worked the best for this purpose. A channel was widened in the cotton Bayou and nine aerator locations were used along with this.

Sea level rise does not have any adverse effect on the DO concentration. In fact, sea level rise solves the low DO problem itself by increasing the DO concentration above the target DO. However, the future climate scenario shows a much warmer climate in 2050. As a result, the DO

concentration dropped below the target DO on some days in June though the dredging-aerator scenario was applied.

This novel study uses MINLAKE2020 and EFDC+ for water quality modeling and provides feedback to the managers and decision makers with important information. MINLAKE2020 is a very reliable model suitable for small waterbodies where not much spatial variance is expected. This model has a strong snow-ice submodel which makes it appropriate to simulate cold-region lakes. Short simulation time embedded future climate simulation capability and robust inflow submodel are other advantages of this model. Being a 1-D model, this model lacks capability to simulate spatial variance. Moreover, this model does not provide the user option to choose between different methods for temperature/DO calculation (which EFDC+ does).

EFDC+ model was used to select the most promising restoration method in CBTC system. The major advantages of this method are its nested model capabilities, sediment diagenesis methods, option to select from different methods (for turbulent diffusion, temperature, DO saturation) and jet/plume boundary conditions. One drawback of this model is the absence of snow submodel which makes it unsuitable for simulating cold region lakes/estuaries. Different types of lakes/estuaries has different characteristics and hence, might need different turbulent diffusion, DO saturation/ temperature governing equations which increases the probability of having a good calibration for any waterbody. The model has capability to use different types of boundary conditions, as a result, the model can be used to simulate aerators.

As a whole, this study manifest the importance of water quality modeling in decision making and managing waterbodies, ranging from lakes to estuaries. Building the right model for

lake water quality simulation, comparing 1D and 3D models for lake simulation studies, calibrating a 3D model for CBTC system, finding the best restoration method and simulating its feasibility through future climate and sea level rise – this study gives a novel idea to water quality modeling on a very application-based approach. These novel approaches and unique utilization of water quality models will help fellow researchers, water quality professionals and managers to use water quality modeling to make informed decisions for restoration and other purposes.

7.3 Limitations

Observed inflow-outflow data for Lake Elmo, Trout Lake and Riley Lake were not available, as a result, hypothetical inflows were simulated for these lakes. There were no observed water temperature and DO data for ice-cover period for Lake Carlos, Trout Lake and Pearl Lake. Moreover, no ice thickness or snow thickness data was available for these lakes. To make a good approximation, the snowfall depth data from the closest weather station was used. Though we had continuous observed data for three probe locations in CBTC, there were not enough observed data for the open boundary conditions, mostly for salinity and water quality parameters. The water quality time series for Gulf of Mexico were used for other boundary conditions by applying some modification (based on historical data available).

7.4 Future Study

EFDC+ model can be modified to include the snow submodel and test in different lakes to support the judgement made in Chapter 3. ADCNR is going to implement the most promising restoration method in CBTC area. A follow-up study can be performed to assess the effect of the restoration technique on the water quality.

References

Akiyama, J., & Stefan, H. G. (1987). Gravity currents in lakes, reservoirs and coastal regions: two-layer stratified flow analysis.

Al-Zubaidi, H. A., & Wells, S. (2018). Comparison of a 2D and 3D Hydrodynamic and Water Quality Model for Lake Systems. World Environmental and Water Resources Congress 2018

Andersen, T. K., Nielsen, A., Jeppesen, E., Bolding, K., Johansson, L. S., Sondergaard, M., & Trolle, D. (2022). Simulating shifting ecological states in a restored, shallow lake with multiple single-model ensembles: Lake Arreskov, Denmark. Environmental Modelling and Software, 156.

Anderson, D. M., Cembella, A. D., & Hallegraeff, G. M. (2012). Progress in understanding Harmful Algal Blooms: Paradigm shifts and new technologies for research, monitoring, and management. Annual Review of Marine Science, 4, 143-176.

Arkema, K. K., Guannel, G., Verutes, G., Wood, S. A., Guerry, A., & Ruckelshaus, M. (2013). Coastal habitats shield people nad property from sea-level rise and storms. Nature Climate Change, 3, 913-918.

Bales, J. D., Tomlison, S. A., & Tillis, G. (2006). Flow and Salt Transport in the Suwannee River Estaury, Florida, 1999-2000: Analysis of Data and Three-Dimensional Simulations. Retrieved from U.S. Geological Survey, Reston, Virginia:

Bartram, J., & Chorus, I. (1999). Toxic Cyanobacteria in Water: A guide to their public health consequences, monitoring and management.

Batick, B. M. (2011). Modeling Temperature and Dissolved Oxygen in the Cheatham Reservoir with CE-QUAL-W2. Vanderbilt University,

Bowen, J. L., Dow, D., Serveiss, V. B., Valiela, I., & Rao, L. (2002). Waquoit Bay Watershed Ecological Risk Assessment: The effect of land-derived nitrogen loads on estuarine eutrophication.

Bowen, J. L., & Valiela, I. (2004). Nitrogen loads to estuaries: using loading models to assess the effectiveness of management options to restore estuarine water quality. Estuaries, 27(3), 482-500.

Bricker, S., Longstaff, B., Dennison, W., Jones, A., Boicourt, K., Wicks, C., & Woerner, J. (2007). Effects of Nutrient Enrichment in the Nation's Estuaries: A Decade of Change - National Estuarine Eutrophication Update. Retrieved from Center for Coastal Monitoring and Assessment, National Centers for Coastal Ocean Science, N/NCCOS/CCMA SSMC4 Floor 9, 1305 East West Highway, Silver Spring, MD.

Burn, D. H., McBean, E., A. (1985). Optimizing modeling of water quality in an uncertain environment. *Water Resources Research*, 21, 934-940.

Carraro, E., N., G., Hamilton, D., Valsecchi, L., Manfredi, E. C., Viviano, G., Copetti, D. (2012). Coupling high-resolution measurements to a threedimensional lakemodel to assess the spatial and temporal dynamics of the cyanobacterium Planktothrix rubescens in a medium-sized lake. Hydrobiologia, 698, 77-95.

Cataño-Lopera, Y.A., Spelman, D., Yee, T., Prathapati, S.(2023), Best Practices for Computational Fluid Dynamic Applications in Water Infrastructure. Journal of Environmental Engineering. **149**(10): p. 03123003.

CH2MHILL. (2011). Remedial, Enforcement Oversight, and Non-Time Critical Removal Activities at Sites of Release or Threatened Release of Hazardous Substances in Region 5.

Chapra, S. C., & Martin, J. L. (2004). LAKE2K, a modeling framework for simulating lake water quality (Version 1.2): documentation and users manual. Retrieved from Civil and Environmental Engineering Dept., Tufts University, Medford, MA.

Chen, G., & Fang, X. (2015). Accuracy of hourly water temperatures in rivers calculated from air temperatures. Water, 7(3), 1068-1087.

Chen, G., Fang, X., & Devkota, J. (2015). Understanding flow dynamics and density currents in a river-reservoir system under upstream reservoir releases. Hydrological Sciences Journal. doi:10.1080/02626667.2015.1112902.

Christmas, J. Y., McBee, J. T., Waller, R. S., & Sutter III, F. C. (1982). Habitat suitability index models: Gulf Menhaden.

Cole, C. (2017). Fish kill brings quick concern, quicker response. Gulf Coast Media. Retrieved from https://gulfcoastmedia.com/stories/fish-kill-brings-quick-concern-quicker-response.

Cole, T. M., & Wells, S. A. (1995). CEQUALW2: A Two-Dimensional, Laterally Averaged, Hydrodynamic and Water Quality Model, Version 3.2. US Army Crops of Engineers, Vickburg, Miss, USA.

Cole, T. M., & Wells, S. A. (2004). CE-QUAL-W2: a two-dimensional, laterally averaged, hydrodynamic and water quality model, version 3.2, user's manual. Retrieved from Vicksburg, MS, 39180:

Cole, T. M., & Wells, S. A. (2010). CE-QUAL-W2: A Two-Dimensional, Laterally Averaged, Hydrodynamic and Water Quality Model, Version 3.6 User Manual.

Conley, D. J., Bonsdorff, E., Carstensen, J., Destouni, G., Gustafsson, B. G., Hansson, L. A., & Rabalais, N. N. (2009). Tackling hypoxia in the blatic sea: is engineering a solution? Enviroment Science Technology, 43(10), 3407-3411.

Craig, P. M., Chung, D. H., LAM, N. T., SON, P. H., & TINH, N. X. (2014, October 9-14, 2014). Sigma-Zed: a computationally efficient approach to reduce the pressure gradient error in the EFDC's vertical sigma grid. Paper presented at the 11th National Conference on Hydrodynamics.

DeGasperi, C. (2013). Prediction Climate Change Effects on Kokanee Habitat Suitability in Lake Sammamish, Washington, King County. Retrieved from

Devkota, J. (2014). Understanding Unsteady Flow and Modeling Water Quality Dynamics in the Coastal Systems under Various Hydrological and Climate Scenarios. (Ph.D.). Auburn University, Auburn, AL 36849.

Devkota, J., & Fang, X. (2015). Quantification of water and salt exchanges in a tidal estuary. Water, 7, 1769-1791. doi:10.3390/w7051769

Dillon, P. J., & Rigler, F. H. (1974). The phosphorus-chlorophyll relationship in lakes: phosphorus-chlorophyll relationship. Limnology Oceanography, 19, 767-773. doi:https://doi.org/10.4319/lo.1974.19.5.0767

Dodds, W. K., Bouska, W. W., Eitzmann, J. L., Pilger, T. J., Pitts, K. L., Riley, A. J., Thornbrugh, D. J. (2008). Eutrophication of U.S. freshwaters: analysis of potential economic damages. Enviromental Science and Technology, 43(1).

DSI. (2020). EFDC+ Theory Version 10.2. Retrieved from Available at https://www.eemodelingsystem.com/efdcplus-theory Accessed on 2020-12-1

Edwards, R., & Owens, M. (1965). The oxygen balance of streams. Ecology and the Industrial Society, 6, 149-172.

Elliott, A. H. (2011). Predicting the impact of changing nutrient load and temperature on the phytoplankton of England's largest lake, Windermere. Freshwater Biology, 57(2), 400-413.

Emanuel, K. (2005). Increasing destructiveness of tropical cyclones over the past 30 years. nature, 436, 686-688.

Engel, L., Heiskary, S., Valley, R., & Tollefson, D. (2012). Sentinel lake assessment report Carrie Lake (34-0032) Kandiyohi County, Minnesota. Retrieved from

Engel, L., Valley, R., Beck, D., & Anderson, J. (2010). Sentinel lake assessment report Lake Carlos (21-0057) Douglas County, Minnesota.

Epanchin-Niell, R. S. (2017). Economics of invasive species policy and management. Biological Invasions, 19, 3333-3354.

Fang, X., Ellis, C. R., & Stefan, H. G. (1996). Simulation and observation of ice formation (freeze-over) in a lake. Cold Regions Science and Technology, 24(2), 129-145.

Fang, X., & Stefan, H. G. (1994). Modeling of dissolved oxygen stratification dynamics in Minnesota lakes under different climate scenarios. Retrieved from Minneapolis, MN 55414:

Fang, X., & Stefan, H. G. (1996b). Long-term lake water temperature and ice cover simulations/measurements. Cold Regions Science and Technology, 24(3), 289-304.

Fang, X., & Stefan, H. G. (1997). Simulated climate change effects on dissolved oxygen characteristics in ice-covered lakes. Ecological Modelling, 103(2-3), 209-229.

Fang, X., & Stefan, H. G. (1998). Potential climate warming effects on ice covers of small lakes in the contiguous U.S. Cold Regions Science and Technology, 27(2), 119-140.

Fang, X., & Stefan, H. G. (2009). Simulations of climate effects on water temperature, dissolved oxygen, and ice and snow covers in lakes of the contiguous United States under past and future climate scenarios. Limnol Oceangr, 54(6), 2359-2370.

Fang, X., Stefan, H. G., Eaton, J. G., McCormick, J. H., & Alam, S. R. (2004). Simulation of thermal/dissolved oxygen habitat for fishes in lakes under different climate scenarios: Part 1. Cool-water fish in the contiguous US. Ecological Modelling, 172(1), 13-37.

Fitzpatrick, J.J. & DiToro, D.M. (1993). Chesapeake Bay Sediment Flux Model. 1993

Flick E. R, Knuuti, K., and Gill, S.K. (2012) Matching Mean Sea Level Rise Projections to Local Elevation Datums. J. Waterway, Port, Coastal, Ocean Eng. doi: 10.1061/(ASCE)WW.1943-5460.0000145.

Garcia, H.E. & Gordon, L.I. (1992). Oxygen solubility in seawater: Better fitting equations. Limnology and oceanography. 37(6): p. 1307-1312.

Gu, R., & Stefan, H. G. (1990). Year-round temperature simulation of cold climate lakes. Cold Regions Science and Technology, 18(2), 147-160.

Hampton, S. E., A.W.E., G., Powers, S. M., Ozersky, T., K.H., W., & R.D., B. (2017). Ecology under lake ice. Ecology Letters, 20, 98-111.

Hamrick, J. (1995). Calibration and verification of the VIMS EFDC model of the James River, Virginia. The College of William and Mary, Virginia Institute of Marine Science.

Henderson-Sellers, B. (1984). Engineering limnology: Pitman Advanced Pub. Program, Boston.

Herb, W. R., & Stefan, H. G. (2005). Model for wind-driven vertical mixing in a shallow lake with submersed macrophytes. Journal of Hydraulic Engineering ASCE, 131(6), 488-496. Retrieved from http://link.aip.org/link/?QHY/131/488/1

Hinkel, J., Nicholls, R. J., Tol, R. S. J., Hamilton, J. M., Boot, G., & Vafeidis, A. T. (2013). A golbal analysis of erosion of sandy beaches and sea-level rise: An application of DIVA. Global and Planetary Change, 11, 150-158.

Hondzo, M., & Stefan, H. G. (1993). Lake water temperature simulation model. Journal of Hydraulic Engineering, 119(11), 1251-1273.

Huang, J., Qi, L., Gao, J., & Kim, D.-K. (2017). Risk assessment of hazardous materials loading into four large lakes in China: A new hydrodynamic indicator based on EFDC. Ecological Indicators, 80, 23-30.

Hudnell, H. K. (2010). The state of U.S. freshwater harmful algal blooms assessments, policy and legislation. Toxicon, 55, 1024-1034.

Hudnell, H. K., & Dortch, Q. (2008). Cyanobacterial harmful algal blooms: Chapter 2: A synopsis of research needs identified at the interagency, international symposium on Cyanobacterial Harmful Algal Blooms (ISOC-HAB).

Imberger, J., & Patterson, J. C. (1989). Physical limnology. In J. W. Hutchinson & T. Wu (Eds.), Advances in applied mechanics (Vol. 27, pp. 303-475): Academic Presss Boston 27:303-475.

Imboden, D. M. (1974). Phosphorus model of lake eutrophication. Limnology and Oceanography, 19(2), 297-304. doi:https://doi.org/10.4319/lo.1974.19.2.0297.

In-Situ Inc. (2023). Aqua Troll 600 Operator's Manual. Retrieved from https://in-situ.com/pub/media/support/documents/Aqua-TROLL-600-Manual.pdf.

Ishikawa, M., Gonzales, W., Golyjeswski, O., Sales, G., Rigotti, A., Bleninger, T., Lorke, A. (2021). Effects of dimensionality on the performance of hydrodynmaic models. Geoscientific Model Development.

Jamily, J. A. (2018). Developing an hourly water quality model to simulate diurnal water temperature and dissovled oxygen variations in shallow lakes. (MS MS). Auburn University, Auburn, Alabama, USA.

Janssen, A. B. G., Teurlincx, S., Beusen, A. H. W., Huijbregts, M. A. J., Rost, J., Schipper, A. M., Janse, J. H. (2019). PCLake+: A process-based ecological model to assess the trophic state of stratified and non-stratified freshwater lakes worldwide. Ecological Modelling, 396, 23-32. doi:https://doi.org/10.1016/j.ecolmodel.2019.01.006

Jeppesen, E., Sondergaard, M., Jensen, J. P., Havens, K. E., Anneville, O., Carvalho, L., Winder, M. (2005). Lake responses to reduced nutrient loading: an analysis of contemporary long-term data from 35 case studies. Freshwater Biology, 50, 1747-1771.

Jiang, L., & Fang, X. (2016). Simulations and validation of cisco lethal conditions in Minnesota lakes under past and future climate scenarios using constant survival limits. Water, 8(7), 279.

Jiang, L., Fang, X., & Chen, G. (2017). Refuge lake reclassification in 620 Minnesota cisco lakes under future climate scenarios. Water, 9, 675.

Jiang, L., Fang, X., Stefan, H. G., Jacobson, P. C., & Pereira, D. L. (2012). Identifying cisco refuge lakes in Minnesota under future climate scenarios using variable benchmark periods. Ecological Modeling, 232(2012), 14-27.

K-1 model developers: K-1 Coupled GCM (MIROC) Description,K-1 Technical Report No. 1,Center for Climate System Research (Univ. of Tokyo), National Institute for Environmental Studies, and Frontier Research Center for Global Change, available at: http://www.ccsr.u-tokyo.ac.jp/kyosei/hasumi/MIROC/tech-repo.pdf, 2004.

Kantha, L.H., & Clayson, C.A. (1994). An improved mixed layer model for geophysical applications. Journal of Geophysical Research: Oceans, 1994. 99(C12): p. 25235-25266.

Kim, J., Lee, T., & Seo, D. (2017). Algal bloom prediction of the lower Han River, Korea using the EFDC hydrodynamic and water quality model. Ecological Modelling, 366, 27-36.

Kim, S.-J., Flato, G. M., Boer, G. J., & McFarlane., N. A. (2002). A coupled climate model simulation of the last glacial maximum, Part 1: transient multi-decadal response. Climate Dynamics, 19, 515-537.

Knuuti, K. (2002) Planning for Sea-Level Rise: U.S. Army Corps of Engineers Policy. Solutions to Coastal Disasters ‘02, ASCE 2002

Lassuy, D. (1983). Gulf menhaden, species profiles: life histories and environmental requirements (Gulf of Mexico). US Department of the Interior, Fish and Wildlife Service.

Le Moal, M., Gascuel-Odoux, C., Menesguen, A., Souchon, Y., Etrillard, C., Levain, A., Pinay, G. (2018). Eutrophication: A new wine in an old bottle? Science of the Total Environment, 1-11.

Li, X. (2019). Hydrodynamic and water quality simulations in the Perdido and Wolf Bay system. (MS). Auburn University, Auburn, AL. Retrieved from http://etd.auburn.edu/handle/10415/6726

Liu, Y., Villalba, G., Ayres, R. U., & Schroder, H. (2008). Global phosphorus flows and environmental impacts from a consumption perspective. Journal of Industrial Ecology, 12.

Livingston, R. J. (2001). Eutrophication processes in coastal systems : origin and succession of plankton blooms and effects on secondary production in gulf coast estuaries. Boca Raton: CRC Press, Taylor & Francis Group.

Livingston, R. J. (2001). Eutrophication processes in coastal systems: origin and succession of plankton blooms and effects on secondary production in Gulf Coast estuaries: CRC.

Livingston, R. J. (2003). Trophic organization in coastal systems: CRC.

Luo, X., & Li, X. (2018). Using the EFDC model to evaluate the risks of eutrophication in an urban constructed pond from different water supply strategies. Ecological Modeling, 372, 1-11.

Man, X., Lei, C., Carey, C. C., & Little, J. C. (2021). Relative Performance of 1-D Versus 3-D Hydrodynmaic, Water Quality Models for Predicting Water Temperature and Oxygen in a Shallow, Eutrophic, Managed Researvoir. Water, 13.

Markfort, C. D., Perez, A. L. S., Thill, J. W., Jaster, D. A., Porté-Agel, F., & Stefan, H. G. (2010). Wind sheltering of a lake by a tree canopy or bluff topography. Water Resour. Res., 46(3), W03530. doi:10.1029/2009wr007759

Marsden, M. W. (1989). Lake restoration by reducing external phosphorus loading; the influence of sediment phosphorus release. Freshwater Biology, 21, 139-162.

Mendoza-Gonzalez, G., Martinez, M. L., Lithgow, D., Perez-Maqueo, O., Simonin, P. (2012). Land use change and its effects on the value of ecosystem services along the coast of the Gulf of Mexico. Ecological Economics, 82, 23-32.

Mengel, M., Levermann, A., Frieler, K., Robinson, A., Marzeion, B., & Winkelmann, R. (2016). Future sea level rise constrained by observations and long-term commitment. The Proceedings of the National Academy of Sciences (PNAS), 113(10), 2597-2602.

Mesman, J. P., Ayala, A. I., Adrian, R., Eyto, E. D., Frassl, M. A., Goyette, S., Ibelings, B. W. (2020). Performance of one-dimensional hydrodynamic lake models during short-term extreme weather events. Environmental Modelling and Software, 133.

MNDNR. Minnesota Department of Natural resources-Sentinel Lake Monitoring. Retrieved from https://www.dnr.state.mn.us/fisheries/slice/sentinel-lakes-monitoring.html

Moomaw, W. R., & Birch, M. B. Cascading costs: An economic nitrogen cycle. Science in China Series C Life Sciences, 48(Special), 678-696.

Moss, B. (2011). Cogs in the endless machine: Lakes, climate change and nutrient cycles: A review. Science of the Total Environment, 434, 130-142.

NAS and NAE. (1973). Water quality criteria 1972 - A report of the committee on water quality criteria. Retrieved from Washington DC:

Nash, J. E., & Sutcliffe, J. V. (1970). River flow forecasting through conceptual models part I-A discussion of principles. Journal of Hydrology, 10(3), 282-290.

Neill, I. J., & Lee, J. J. (2020). NASA-led study reveals the caues of sea level rise since 1990.

Nozawa, T., Nagashima, T., Ogura, T., Yokohata, T., Okada, N., & Shiogama, H. (2007). Climate change simulations with a coupled ocean-atmosphere GCM called the Model for Interdisciplinary Research on Climate: MIROC, CGER Supercomputer Monograph Report Vol. 12, Center for Global Environmental Research, National Institute for Environmental Studies, Tsukuba, Japan.

Philips, G., Kelly, A., Pitt, J. A., Sanderson, R., & Taylor, E. (2005). The recovery of a very shallow eutrophic lake, 20 years after the control of effluent derived phosphorus. Freshwater Biology, 50, 1628-1638.

Pretty, J. N., Mason, C. F., Nedwell, D. B., Hine, R. E., Leaf, S., & Dils, R. (2003). Environmental Costs of Freshwater Eutrophication in England and Wales. Environmental Science and Technology Library, 37.

Rahaghi, A. I., Lemmin, U., Cimatoribus, A. A., & Barry, D. A. (2019). The importance of systemic spatial variability in the surfcae heat flux of a large lake: a multiannual analysis for Lake Geneva. Water Resource Research, 55, 10248-10267.

Riley, M. J., & Stefan, H. G. (1988). Minlake: A dynamic lake water quality simulation model. Ecological Modelling, 43(3-4), 155-182.

Romero, J. R., Antenucci, J. P., & Imberger, J. (2004). One- and three-dimensional biogeochemical simulations of two differing reservoirs. Ecological Modelling, 174(1-2), 143-160. Retrieved from http://www.sciencedirect.com/science/article/pii/S0304380004000043

Seewer, J. (2020). Ohio wants to put Lake Erie on a new, strict pollution diet. APnews.

Shen, J., & Haas, L. (2004). Calculating age and residence time in the tidal York River suing three-dimensional model experiments. Estuarine, Coastal and Shelf Science, 61(3), 449-461.

Shimoda, Y., & Arhonditsis, G. B. (2016). Phytoplankton functional type modelling: running before we can walk? A critical evaluation of the current state of knowledge. Ecological Modeling, 320, 29-43.

Smith, E. A., Kiesling, R. L., Galloway, J. M., & Ziegeweid, J. R. (2014) Water quality and algal community dynamics of three deepwater lakes in Minnesota utilizing CE-QUAL-W2 models. In: U.S. Geological Survey Scientific Investigations Report 2014–5066, 73 p., http://dx.doi.org/10.3133/sir20145066.

Sondergaard, M., Jeppesen, E., Jensen, J. P., & Amsinck, S. L. (2005). Water framework directive: ecological classification of Danish lakes. Journal of Applied Ecology, 42, 616-629.

Sondergaard, M., Jeppesen, E., Lauridsen, T. L., Skov, C., Nes, E. H. V., Roijackers, R., Portielje, R. (2007). Lake restoration: successes, failures and long-term effects. Journal of Applied Ecology, 44, 1095-1105.

Song, W., Xu, Q., Fu, X., Wang, C., Pang, Y., & Song, D. (2019). EFDC simulation of fishway in the Diversion Dahaerteng River to Danghe Reservoir, China. Ecological Indicators, 102, 704-715.

Stefan, H. G., & Fang, X. (1994). Dissolved oxygen model for regional lake analysis. Ecological Modelling, 71, 37-68.

Stefan, H. G., Hondzo, M., Fang, X., Eaton, J. G., & McCormick, J. H. (1996). Simulated long-term temperature and dissolved oxygen characteristics of lakes in the north-central United States and associated fish habitat limits. Limnology and Oceanography, 41(5), 1124-1135.

Stefanidis, K., Varlas, G., Papaioannou, G., Papadopouolos, A., & Dimitriou, E. (2022). Trends of lake temperature, mixing depth and ice cover thickness of European lakes during the last four decades. Science of the Total Environment, 830(154709).

Stepanenko, V. M., Goyette, S., Martynov, A., Perroud, M., & Fang, X. (2010). First steps of a lake model intercomparison project: LakeMIP. Boreal Environment Research, 15, 191-202.

Stepanenko, V. M., Martynov, A., Joehnk, K. D., Subin, Z. M., Perroud, M., Fang, X., Goyette, S. (2013). A one-dimensional model intercomparison study of thermal regime of a shallow, turbid midlatitude lake. Geoscientific Model Development 6, 1337-1352.

Sun, B., Chen, W., Li, N., Wang, W., Fu, C., Liu, Y., & Gao, X. (2022). Quantifying the effects of submerged aquatic vegetation on internal loading in lake: A modeling study of the largest shallow lake in North China. Science of the Total Environment, 853.

Sweet, W. V., B.D. Hamlington, R.E. Kopp, C.P. Weaver, P.L. Barnard, D. Bekaert, G. Garner, A. S. G., J.P. Krasting, E. Larour, D. Marcy, J.J. Marra, J. Obeysekera, M. Osler, M. Pendleton, D. Roman, L. Schmied, W. Veatch, K.D. White, and C. Zuzak. (2022). Global and regional sea level rise scenarios for the United States: updated mean projections and extreme water level probabilities along U.S. coastlines. Retrieved from Silver Spring, MD:

Sweet, W. V., Kopp, R. E., Weaver, C. P., Obeysekera, J., & Horton, R. M. (2017). Global and Regional Sea Level Rise Scenarios for the United States. NOAA Technical Report NOS CO-OPS 083. Retrieved from Silver Spring, MD:

Taguchi, V. J., Olsen, T. A., Janke, B. D., Gulliver, J. S., Finlay, J. C., & Stefan, H. G. (2020). Internal loadong in stormwater ponds as a phosphorus source to downstream waters. Limnology and Oceanography Letters, 5, 322-330.

Takolander, A., Cabeza, M., & Leskinen, E. (2017). Climate change can cause complex responses in Baltic Sea macroalgae: A systematic review. (123), 16-29.

Tasnim, B., Jamily, J. A., Fang, X., Zhou, Y., & Hayworth, J. S. (2021). Simulating diurnal variatios of water temperature and dissolved oxygen in shallow Minnesota lakes. Water, 13(1980).

Thiery, W., Stepanenko, V. M., Fang, X., Jöhnk, K. D., Li, Z., Martynov, A., Martynov A., Perroud M., Subin Z.M., Darchambeau F., Mironov D., Van Lipzig N.P.M. (2014).

LakeMIP Kivu: Evaluating the representation of a large, deep tropical lake by a set of one-dimensional lake models. Tellus A, 2014(66), 21390,

Thomann, R. V., & Mueller, J. A. (1987). Principles of Surface Water Quality Modeling and Control: Harper Collins Publishers.

Townsend, A. R., Howarth, R. W., Bazzaz, F. A., Booth, M. S., Cleveland, C. C., Collinge, S. K., Wolfe, A. H. (2003). Human health effects of a changing global nitrogen cycle. Frontiers in Ecology and the Environment, 1(5).

Turner, R. E. (2003). Linking landscape and water quality in the Mississippi river basin for 200 years. Bioscience, 53.

VenderKooy, S. J., & Smith, J. W. (2015). The Menhaden Fishery of the Gulf of Mexico, United States: A Regional management Plan, 2015 Revision. Retrieved from

Vollenweider, R. A., & J., K. (1982). Eutrophication of waters. Monitoring, assessment and control. OECD Cooperative Programme on Monitoring of Inland Waters.

Welch, E. B., & Cooke, G. D. (2009). Internal phosphorus loading in shallow lakes: Importance and control. Lake and Reservoir Management, 21(2), 209-217.

Wells, S. A. (2020). Thermal Stratification Effects in Lakes and Reservoirs. Inland Waters.

West, D., & H. G. Stefan. (1998). Simulation of lake water quality using a one-dimensional model with watershed input. Model Description and application to Lake Riley and Lake Elmo, project report No.430. Retrieved from

Wolfe, A. H., & Patz, J. A. (2002). Reactive nitrogen and human health: acute and longterm implications. AMBIO: A Journal of the Human Environment, 31(2).

Wu, G., & Xu, Z. (2011). Prediction of algal blooming using EFDC model: Case study in the Daoxiang Lake. Ecological Modelling, 222(6), 1245-1252.

Xia, M., Craig, P. M., Wallen, C. M., Stoddard, A., Mandrup-Poulsen, J., Peng, M., Liu, Z. (2011). Numerical simulation of salinity and dissolved oxygen at Perdido Bay and adjacent coastal ocean. Journal of Coastal Research, 27(1), 73-86.

Yao, H., Samal, N. R., Joehnk, K. D., Fang, X., Bruce, L. C., Pieson, D. C., James, A. (2014). Comparison of lake ice dynamics model performance: Harp Lake, Ontario, Canada. Hydrological Processes.

Zhang, X., Recknagel, F., Chen, Q., Cao, H., & Li, R. (2015). Spatially-explicit modelling and forecasting of cyanobacteria growth in Lake Taihu by evolutionary computation. Ecological Modeling, 306, 216-225.

Zheng, L., Wang, H., Liu, C., Zhang, S., Ding, A., Xie, E., Wang, S. (2021). Prediction of harmful lagal blooms in large water bodies using the combined EFDC and LSTM models. Journal of Environmental Management, 295.

APPENDIX A

Sample of observed inflow-Outflow data collected from USGS (Smith et al., 2014)

					Le Homme Dieu	Le Homme Dieu	Le Homme Dieu	Darling	Darling	Darling	Long Prairie	Long Prairie	Long Prairie
					5244810	5244810	5244810	5244780	5244780	5244780	5244820	5244820	5244820
YEAR	MONTH	DAY	YYYY-MM-DD HH:MM	Time	Discharge (cfs)	Elevation (ft)	Temp (°C)	Discharge (cfs)	Elevation (ft)	Temp (°C)	Discharge (cfs)	Elevation (ft)	Temp (°C)
2010	3	14	2010-03-14 00:00	0:00	23	1356.37	0.8						
2010	3	14	2010-03-14 00:15	0:15	23	1356.37	0.8						
2010	3	14	2010-03-14 00:30	0:30	23	1356.38	0.7						
2010	3	14	2010-03-14 00:45	0:45	23	1356.37	0.7						
2010	3	14	2010-03-14 01:00	1:00	23	1356.38	0.7						
2010	3	14	2010-03-14 01:15	1:15	23	1356.37	0.7						
2010	3	14	2010-03-14 01:30	1:30	23	1356.38	0.7						
2010	3	14	2010-03-14 01:45	1:45	23	1356.38	0.7						
2010	3	14	2010-03-14 02:00	2:00									
2010	3	14	2010-03-14 02:15	2:15									
2010	3	14	2010-03-14 02:30	2:30									
2010	3	14	2010-03-14 02:45	2:45									
2010	3	14	2010-03-14 03:00	3:00	23	1356.37	0.7						
2010	3	14	2010-03-14 03:15	3:15	23	1356.38	0.7						
2010	3	14	2010-03-14 03:30	3:30	23	1356.38	0.7						
2010	3	14	2010-03-14 03:45	3:45	23	1356.38	0.7						
2010	3	14	2010-03-14 04:00	4:00	23	1356.38	0.7						
2010	3	14	2010-03-14 04:15	4:15	23	1356.38	0.7						
2010	3	14	2010-03-14 04:30	4:30	23	1356.38	0.7						
2010	3	14	2010-03-14 04:45	4:45	23	1356.39	0.7						
2010	3	14	2010-03-14 05:00	5:00	23	1356.38	0.7	28	1356.49	1.1			
2010	3	14	2010-03-14 05:15	5:15	23	1356.38	0.7	28	1356.49	1.1			
2010	3	14	2010-03-14 05:30	5:30	23	1356.38	0.7	28	1356.49	1.1			
2010	3	14	2010-03-14 05:45	5:45	23	1356.38	0.7	28	1356.49	1.1			
2010	3	14	2010-03-14 06:00	6:00	23	1356.38	0.7	28	1356.49	1.1			
2010	3	14	2010-03-14 06:15	6:15	23	1356.38	0.7	28	1356.49	1.1			
2010	3	14	2010-03-14 06:30	6:30	23	1356.38	0.7	28	1356.49	1.1			
2010	3	14	2010-03-14 06:45	6:45	23	1356.38	0.7	28	1356.49	1.1			
2010	3	14	2010-03-14 07:00	7:00	23	1356.38	0.7	28	1356.49	1.0			
2010	3	14	2010-03-14 07:15	7:15	23	1356.38	0.7	28	1356.49	1.0			
2010	3	14	2010-03-14 07:30	7:30	23	1356.38	0.7	28	1356.49	1.0			
2010	3	14	2010-03-14 07:45	7:45	23	1356.38	0.7	28	1356.49	1.1			
2010	3	14	2010-03-14 08:00	8:00	23	1356.38	0.7	28	1356.49	1.0			
2010	3	14	2010-03-14 08:15	8:15	23	1356.39	0.7	28	1356.49	1.1			

APPENDIX B

Sample of observed water quality data collected by Aqua Troll 600 probes at Cotton Bayou-Terry Cove (Location 3 data is presented here)

In-Situ **This file can be opened directly in Microsoft Excel** *(or you can Export a CSV)*

Location Properties
Location Name = Location 3
Location ID = b5912ab0-7f85-442f-ab2c-a6481ad3bf6e

Report Properties
Start Time = 2022-11-07 13:50:42
Duration = 259.20:00:32
Readings = 3119
Time Offset = -05:00:00

Instrument Properties
Device Model = Aqua TROLL 600 Vented
Device SN = 949763
Device Firmware = 2.29

Log Properties
Log Name = Location 3
Log Type = Linear
Log File Number = 1
Log ID = 27ff871c-9751-40f5-a1c5-33b910cca617
Interval = 02:00:00

Date Time	Chlorophyll-a Fluorescence (RFU) (945790)	RDO Concentration (mg/L) (946526)	RDO Saturation (%Sat) (946526)	Oxygen Partial Pressure (Torr) (946526)	BGA-PE Fluorescence (RFU) (933003)
2022-11-07 13:50:42	0.01059402	7.214205	91.44366	141.3154	0
2022-11-07 15:50:42	0.7554823	6.734423	92.75787	144.3304	0.01932205
2022-11-07 17:50:42	0.7336902	6.611543	92.75037	144.2985	0.01812092
2022-11-07 19:50:42	0.2395875	6.770123	94.99735	147.959	0.01439038
2022-11-07 21:50:42	0.09757682	6.762247	94.85017	147.7831	0.01630272
2022-11-07 23:50:42	0.1128751	6.70625	94.04355	146.581	0.01417346
2022-11-08 01:50:42	0.3184149	6.309557	88.25548	137.5847	0.01838492
2022-11-08 03:50:42	0.2610726	6.238832	87.13715	135.8241	0.01705673
2022-11-08 05:50:42	0.3619642	6.156585	85.72269	133.6964	0.01755901
2022-11-08 07:50:42	0.4977148	6.021441	83.41618	130.2829	0.01794091
2022-11-08 09:50:42	0.5056149	5.940293	82.14776	128.4277	0.01697043
2022-11-08 11:50:42	0.4329934	5.986462	83.64282	130.6378	0.0108939
2022-11-08 13:50:42	0.4501418	6.087646	85.66177	133.5057	0.01258777
2022-11-08 15:50:42	0.5758466	6.585487	93.07104	144.8265	0.008457927
2022-11-08 17:50:42	0.5641719	6.762573	95.61555	148.7509	0.01108555
2022-11-08 19:50:42	0.1847711	6.833575	96.63202	150.4622	0.009394284
2022-11-08 21:50:42	0.04128317	6.79491	95.58987	148.9553	0.01194079
2022-11-08 23:50:42	0.03736258	6.636103	93.63247	145.9154	0.007624175
2022-11-09 01:50:42	0.04555367	6.59536	92.72578	144.5459	0.01270132
2022-11-09 03:50:42	0.3854123	6.16059	86.63873	135.0897	0.009466488
2022-11-09 05:50:42	0.1936362	6.111282	84.63856	132.1745	0.009419834
2022-11-09 07:50:42	0.5934185	6.031563	82.66284	129.3457	0.0115956
2022-11-09 09:50:42	0.705584	5.893231	80.4129	125.9389	0.01530758
2022-11-09 11:50:42	0.7100319	6.136657	83.94279	131.3906	0.01227291
2022-11-09 13:50:42	0.2893432	6.786117	92.87153	145.0516	0.01224366
2022-11-09 15:50:42	0.2621796	7.095897	96.99406	151.3062	0.01214962
2022-11-09 17:50:42	0.1533854	7.085498	96.85841	151.062	0.01057125
2022-11-09 19:50:42	0.3097853	7.062887	96.70867	150.8358	0.01225561
2022-11-09 21:50:42	0.1978493	6.985074	94.86115	148.058	0.01260918
2022-11-09 23:50:42	0.2276881	6.881836	92.70884	144.6456	0.01224277
2022-11-10 01:50:42	0.08737375	6.848372	91.82489	143.1218	0.01346467
2022-11-10 03:50:42	0.1404631	6.735312	90.22739	140.4384	0.01093114

APPENDIX C

Sample results of laboratory analysis of grab samples collected from Cotton Bayou-Terry Cove area

Water Analyte	L2			
	Result	DL	RL	Qual
Dissolved organic carbon (mg/L)	2.2	0.5	1	
Total phosphate (mg/L)	0.1	0.1	0.3	U
Ammonia nitrogen (mg/L)	0.05	0.05	0.25	U
Nitrate-nitrite (mg/L)	0.01	0.01	0.05	U
Dissolved available silica (mg/L)	0.48	0.054	0.11	
Chlorophyll-A (ug/L)	1.3	0.1	0.2	

Sediment Analyte	L2			
	Result	DL	RL	Qual
% Solids	74.28			
Total phosphate (mg/kg)	2.3	1.62	6.75	I
Ammonia nitrogen (mg/kg as N)	10	10	50	U
Nitrate-nitrite (mg/kg)	0.135	0.135	0.675	U

Sampled 2/21/2023

Water Analyte	L2			
	Result	DL	RL	Qual
Chemical Oxygen Demand (mg/L)	122000	5000	25000	U
Total phosphate (mg/L)	0.1	0.1	0.3	U

Sampled 7/25/2023

U: compound was analyzed for but not detected

I: Reported value is between the MDL and PQL

J: Spike recovery high(205%) with control limits of 90-110%. The sample may have been spiked twice. All other QCs passed.